Modeling flow-induced crystallization of polymers

Steenbakkers, R.J.A

Award date:
2005

Modeling Flow-Induced Crystallization of Polymers

Rudi Steenbakkers
MT05.43

Thesis committee:

Prof.dr.ir. H.E.H. Meijer, chair
Dr.ir. G.W.M. Peters, coach
Dr.ir. M.A. Hulsen
Ir. J.W. Housmans
Dr.ir. J.G.P. Goossens (Dept. of Chem. Eng.)
M.Sc. L. Balzano (Dept. of Chem. Eng.)

July 15th 2005

Contents

Samenvatting

De (mechanische) eigenschappen van een kunststof product zijn niet alleen afhankelijk van de moleculaire structuur van de polymere grondstof, maar ook van de thermische en mechanische belasting waaraan deze tijdens de fabricage onderworpen wordt. De morfologie die men aantreft in een uit semikristallijn polymeer vervaardigd product hangt nauw samen met de thermische en mechanische geschiedenis van het polymeer. Stromingsgeïnduceerde kristallisatie is daarbij een belangrijk fenomeen, dat echter in veel opzichten nog niet of slechts ten dele begrepen wordt. Voor de vervaardiging van producten die aan hoge specificaties moeten voldoen en voor de optimalisering van fabricageprocessen is het van belang dat dit fenomeen gemodelleerd kan worden.

Dit afstudeerwerk bestaat uit twee delen: in het eerste wordt de opzet van een algemeen model voor stromingsgeïnduceerde kristallisatie beschreven. Dit model is opgebouwd uit een aantal onderdelen, die gebaseerd zijn op eerder theoretisch werk dat, waar nodig, aangepast en uitgebreid werd. In het tweede deel wordt een aantal aspecten van het model geverifieerd aan de hand van beschikbare experimentele gegevens m.b.t. de isotherme kristallisatie van een lineair isotactisch polypropeen, dat aan een kortstondige afschuifstroming onderworpen werd.

De overeenkomst tussen de voorspellingen van het model en de resultaten van de experimenten is uitstekend. Dit werk kan daarom gezien worden als een eerste stap op weg naar het kwantitatief modelleren van de kristallisatie van polymeren met complexere moleculaire structuren onder industrieel relevante thermische en mechanische belasting.

Abstract

The (mechanical) properties of a plastic product are not only determined by the molecular structure of the polymeric material, but also by the thermal and mechanical loading to which this material is subjected during the manufacturing stage. The morphology observed within a semicrystalline polymer product is closely related to the thermal and mechanical history of the polymer. Here, flow-induced crystallization is a phenomenon that plays an important role. However, in many respects, it is not or only partly understood yet. For the manufacturing of products with high design specifications, as well as for the optimization of manufacturing processes, it is important to be able to model this phenomenon.

This master's thesis consists of two parts: in the first part, a comprehensive model of flow-induced crystallization is presented. This model comprises different elements, which are based on earlier theoretical developments that, where necessary, were modified and extended. In the second part, some aspects of the model are verified by available experimental data on the isothermal crystallization of a linear isotactic polypropylene, which was subjected to short-term shear flow.

The correspondence between the model predictions and the experimental results is excellent. Therefore, this work can be viewed as a first step towards the quantitative modeling of crystallization of polymers with more complex molecular structures under industrially relevant thermal and mechanical loading conditions.

Chapter 1

Introduction

In this work, a comprehensive framework for modeling flow-induced crystallization (FIC) of polymers is presented. The main effects of flow observed at the macroscopic level, which are to be described by the modeling, are twofold. First of all, already under moderate flow conditions, the nucleation density is significantly increased. Janeschitz-Kriegl [58] demonstrated that the number of spherulites obtained after a well-defined flow history depends on the applied mechanical work in a nonlinear fashion. This implies that flow-induced crystallization is a self-enhancing process. Secondly, if the flow (or flow history) is strong enough, oriented crystallites are formed. It has been observed [4, 52] that a strong increase of the number of spherulites and the appearance of oriented crystallites occur simultaneously. A typical example where these two effects are observed is shown in figure 1.1.

The kinetics of crystallization have traditionally been described in terms of nucleation, i.e. the appearance of primordial crystalline entities in the amorphous phase, and growth of these so-called nuclei into crystallites. According to the classical nucleation theory for polymers, developed by Lauritzen and Hoffman [51, 68], a nucleus becomes stable, meaning that folded-chain lamellae can spontaneously grow from its surface, when it reaches a critical size. It has been common practice, for modeling purposes, to derive an expression for the rate at which nuclei cross this size barrier, i.e. the nucleation rate. Much less attention has been devoted to the nuclei that do not become stable. An important part of the modeling presented here consists of a description of the creation, growth, and disappearance of these unstable nuclei, which we call precursors.

The reason for introducing precursors is the experimental observation that, in a melt crystallized at constant temperature, in quiescent conditions as well as after short-term flow, all spherulites have nearly the same diameter. The concept of precursors allows us to capture this effect, while still

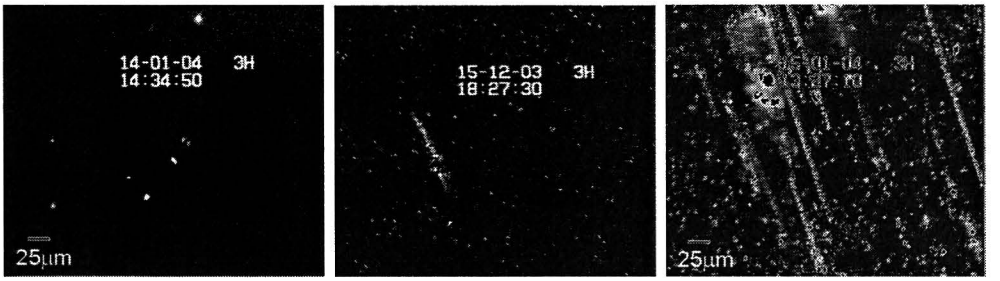

Figure 1.1: Optical micrographs of a linear isotactic polypropylene melt crystallizing at 135°C after different flow histories. The images were taken 120 seconds after cessation of short-term shear flow, which was applied at a constant rate of $60s^{-1}$ for a duration of one second (left), three seconds (middle), and six seconds (right) [52].

predicting a strong influence of flow on the nucleation process. It is assumed that nucleation is severely impeded by the flow, which prevents chain segments from aligning in folded-chain lamellae. Therefore, during flow only precursors are created. These immediately become nuclei when the flow is stopped. This fast transformation is justified by the observation that, in quiescent crystallization, all nuclei are present from the start. Relating the rate of creation of precursors to a measure of the deformation of molecules in the melt, obtained from a constitutive model for the stress, we show that point nucleation induced by short-term deformation can be described quantitatively.

For strong flows, threadlike precursors develop, which may grow into oriented crystallites. A description of the growth of pointlike precursors into threadlike precursors, and the resulting transition from an isotropic to an anisotropic morphology, has been established. However, at the moment, there are too many free parameters. Experiments will have to be designed to determine these parameters, before trying to simulate flow-induced crystallization experiments where a highly anisotropic morphology develops.

The semicrystalline morphology that develops influences the rheology of the crystallizing polymer. We propose to model the crystallizing polymer as a suspension, following the work of Tanner [111, 112]. An essential feature of our approach is that the rheological properties of the amorphous phase, viewed as the matrix in the suspension model, are affected by the presence of precursors. Moreover, the rheological properties of the semicrystalline phase, i.e. of the crystallites that play the role of particles in the suspension model, change due to perfection of the crystalline structure. Hence, we view a crystallizing polymer as a suspension with evolving properties of the matrix and the particles.

The ultimate objective of all this is to simulate the crystallization process during continuous flow. In contrast to the short-term flow experiments, the processes of creation, disappearance, and nucleation of precursors on one hand, and the disturbance of the flow by the presence of crystallites on the other hand, will then interfere. An important subject of future work will be to resolve the coupling between crystallization kinetics and rheology. A first step is taken here.

Chapter 2

Development of a FIC model

Modeling flow-induced crystallization requires understanding of two processes: the response of the material to thermomechanical loading and the transformation of the amorphous phase into the crystalline phase. Since these processes influence each other, as is evident from the vast amount of literature on flow-induced crystallization experiments, it is necessary to incorporate information on the crystalline morphology in the constitutive model for the stress state and information on the thermomechanical history of the material in the description of phase transformation kinetics. A framework is presented that incorporates concepts from rheology and crystallization kinetics in a comprehensive model of flow-induced crystallization.

2.1 Rheology of polymer melts

2.1.1 Kinematics and stresses

The Cauchy stress tensor of the fully amorphous melt is written in the form

$$\boldsymbol{\sigma} = -p\boldsymbol{I} + \boldsymbol{\tau}_v + \sum_{i=1}^{M} \boldsymbol{\tau}_{e,i}\,, \tag{2.1}$$

where the extra stress tensor is decomposed into a viscous mode $\boldsymbol{\tau}_v = 2\eta\boldsymbol{D}$ and M viscoelastic modes $\boldsymbol{\tau}_{e,i}$. The viscous stress is defined by an appropriate choice for the viscosity η, which may for instance depend on the deformation rate and temperature. The viscoelastic stress modes are related to the deformation, i.e. orientation and stretch, of macromolecules in the melt. The deformation of a single macromolecular chain is elastic: upon removal of the stress, its original contour length is regained and its orientation tends back to the isotropic, coil-like state. However, deformation at the molecular level is

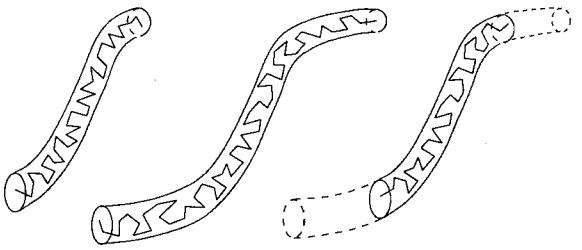

Figure 2.1: Nonaffine deformation of a macromolecular chain. A similar picture can be found in Larson [66].

nonaffine with respect to the macroscopic deformation. Energy is dissipated as a result of slippage of the chain with respect to the continuum; see figure 2.1. Peters and Baaijens [87] used the concept of a slip tensor to describe this effect. Their approach is briefly outlined here.

The molecular structure of the melt is represented by a set of connector vectors $\vec{R}_i$. The equation of motion of a connector vector is written as

$$\dot{\vec{R}}_i = (\boldsymbol{L} - \boldsymbol{A}_i) \cdot \vec{R}_i = \boldsymbol{L}_{e,i} \cdot \vec{R}_i \,, \tag{2.2}$$

where $\boldsymbol{A}_i$ is the slip tensor and $\boldsymbol{L}_{e,i}$ is the elastic part of the velocity gradient tensor $\boldsymbol{L}$. A dot designates the material time derivative, $\dot{x} = \partial x/\partial t + \vec{v} \cdot \vec{\nabla} x$. The connector vectors are written as $\vec{R}_i = \Lambda_i \vec{n}_i$, with $\vec{n}_i$ a unit vector and Λ_i the appropriate stretch factor. The average of the dyadic product $\vec{R}_i \vec{R}_i$ over all orientations is known as the conformation tensor. Under the assumption that the stretch is independent of orientation, hence $\langle \Lambda_i \rangle = \Lambda_i$, the conformation tensor is given by

$$\langle \vec{R}_i \vec{R}_i \rangle = \langle \Lambda_i \vec{n}_i \Lambda_i \vec{n}_i \rangle \; = \Lambda_i^2 \langle \vec{n}_i \vec{n}_i \rangle = \Lambda_i^2 \boldsymbol{S}_i \,, \tag{2.3}$$

where $\boldsymbol{S}_i = \langle \vec{n}_i \vec{n}_i \rangle$ is the orientation tensor. The evolution equation for the conformation tensor is derived from the equation of motion (2.2) as

$$\frac{D}{Dt} \langle \vec{R}_i \vec{R}_i \rangle = \boldsymbol{L}_{e,i} \cdot \langle \vec{R}_i \vec{R}_i \rangle + \langle \vec{R}_i \vec{R}_i \rangle \cdot \boldsymbol{L}_{e,i}^T \,, \tag{2.4}$$

in which D/Dt is another notation for the material time derivative. The deformation tensor is decomposed into an elastic part and a plastic part ($\boldsymbol{F} = \boldsymbol{F}_{e,i} \cdot \boldsymbol{F}_{p,i}$). The velocity gradient tensor $\boldsymbol{L} = \dot{\boldsymbol{F}} \cdot \boldsymbol{F}^{-1}$ can then be written as the sum of an elastic part

$$\boldsymbol{L}_{e,i} = \boldsymbol{L} - \boldsymbol{A}_i = \dot{\boldsymbol{F}}_{e,i} \cdot \boldsymbol{F}_{e,i}^{-1} \tag{2.5}$$

and a plastic part

$$\boldsymbol{L}_{p,i} = \boldsymbol{A}_i = \boldsymbol{F}_{e,i} \cdot \dot{\boldsymbol{F}}_{p,i} \cdot \boldsymbol{F}^{-1} . \tag{2.6}$$

Furthermore, the elastic Finger tensor is defined as

$$\boldsymbol{B}_{e,i} = \boldsymbol{F}_{e,i} \cdot \boldsymbol{F}_{e,i}^{T} . \tag{2.7}$$

Since it is easily shown that the time derivative of $\boldsymbol{B}_{e,i}$ obeys

$$\dot{\boldsymbol{B}}_{e,i} = \boldsymbol{L}_{e,i} \cdot \boldsymbol{B}_{e,i} + \boldsymbol{B}_{e,i} \cdot \boldsymbol{L}_{e,i}^{T} , \tag{2.8}$$

which is equivalent to equation 2.4 with $\langle \vec{R}_i \vec{R}_i \rangle$ replaced by $\boldsymbol{B}_{e,i}$, it follows from the initial conditions $\langle \vec{R}_i \vec{R}_i \rangle = \frac{1}{3}\boldsymbol{I}$ and $\boldsymbol{B}_{e,i} = \boldsymbol{I}$, corresponding to the undeformed configuration, that

$$\boldsymbol{B}_{e,i} = 3\langle \vec{R}_i \vec{R}_i \rangle = 3\Lambda_i^2 \boldsymbol{S}_i . \tag{2.9}$$

Hence, the elastic Finger tensor is directly related to the stretch and orientation of molecules in the melt. For this reason, Zuidema *et al.* [131, 132] used the second invariant of the deviatoric part of $\boldsymbol{B}_e$ as the driving force for flow-induced nucleation and crystal growth.

The viscoelastic stress, experienced momentarily by the temporary network of entangled chains, is denoted by $\boldsymbol{\sigma}_{e,i}$ and is related to the elastic Finger tensor according to

$$\boldsymbol{\sigma}_{e,i} = G_i \boldsymbol{B}_{e,i} = 3G_i \Lambda_i^2 \boldsymbol{S}_i . \tag{2.10}$$

Defining the viscoelastic modes of the extra stress tensor as $\boldsymbol{\tau}_{e,i} = \boldsymbol{\sigma}_{e,i} - G_i \boldsymbol{I}$, which in combination with equation 2.10 is analogous to the well-known neo-Hookean constitutive model $\boldsymbol{\tau} = G(\boldsymbol{B} - \boldsymbol{I})$, the overall contribution of these viscoelastic modes is written as

$$\boldsymbol{\tau}_e = \sum_{i=1}^{M} G_i \left(\boldsymbol{B}_{e,i} - \boldsymbol{I} \right) = \sum_{i=1}^{M} G_i \left(3\Lambda_i^2 \boldsymbol{S}_i - \boldsymbol{I} \right) . \tag{2.11}$$

2.1.2 Non-linear viscoelastic constitutive models

With the viscoelastic part of the extra stress in equation 2.1 given by equation 2.11, the constitutive modeling is completed by a formulation of the evolution of the elastic Finger tensor $\boldsymbol{B}_{e,i}$ or, equivalently, of the orientation tensor $\boldsymbol{S}_i$

[1] Also known as the Truesdell rate.
[2] Also known as the Cotter–Rivlin rate.
[3] Also known as the Jaumann rate.

Table 2.1: Definition of some objective derivatives.

Upper convected derivative[1]	$\overset{\triangledown}{\boldsymbol{X}} = \dot{\boldsymbol{X}} - \boldsymbol{L}\cdot\boldsymbol{X} - \boldsymbol{X}\cdot\boldsymbol{L}^T$
Lower convected derivative[2]	$\overset{\triangle}{\boldsymbol{X}} = \dot{\boldsymbol{X}} + \boldsymbol{L}^T\cdot\boldsymbol{X} + \boldsymbol{X}\cdot\boldsymbol{L}$
Corotational derivative[3]	$\overset{\circ}{\boldsymbol{X}} = \dot{\boldsymbol{X}} - \boldsymbol{\Omega}\cdot\boldsymbol{X} - \boldsymbol{X}\cdot\boldsymbol{\Omega}^T$
Gordon–Schowalter derivative	$\overset{\square}{\boldsymbol{X}} = \overset{\triangledown}{\boldsymbol{X}} + \zeta\left(\boldsymbol{D}\cdot\boldsymbol{X} + \boldsymbol{X}\cdot\boldsymbol{D}\right)$

and the stretch parameter Λ_i. This means that a slip tensor $\boldsymbol{A}_i$ has to be specified. Taking the upper convected derivative of equation 2.10 (see table 2.1) and substituting equations 2.5 and 2.8, the evolution of the viscoelastic stress $\boldsymbol{\sigma}_{e,i}$ is obtained as

$$\overset{\triangledown}{\boldsymbol{\sigma}}_{e,i} + \boldsymbol{A}_i\cdot\boldsymbol{\sigma}_{e,i} + \boldsymbol{\sigma}_{e,i}\cdot\boldsymbol{A}_i^T = \boldsymbol{O}\,. \tag{2.12}$$

For $\boldsymbol{\tau}_{e,i}$ we get, making use of $\overset{\triangledown}{\boldsymbol{I}} = -2\boldsymbol{D}$,

$$\overset{\triangledown}{\boldsymbol{\tau}}_{e,i} + \boldsymbol{A}_i\cdot\boldsymbol{\tau}_{e,i} + \boldsymbol{\tau}_{e,i}\cdot\boldsymbol{A}_i^T + G_i\left(\boldsymbol{A}_i + \boldsymbol{A}_i^T\right) = 2G_i\boldsymbol{D}\,. \tag{2.13}$$

Several nonlinear viscoelastic constitutive models can be reproduced by an appropriate choice for the slip tensor $\boldsymbol{A}_i$ (see appendix A from Peters and Baaijens [87] and table 3.1 from Swartjes [110]). Table 2.2 summarizes the governing equations for the most frequently used models, omitting the subscript i for the sake of brevity.

It is essential, when trying to understand the molecular origins of flow-induced crystallization, that the effects of orientation and stretch can be studied separately. This will be one of the subjects of chapter 3. Such a separation is accomplished by decomposing the elastic Finger tensor into the orientation tensor $\boldsymbol{S}_i$ and the scalar stretch parameter Λ_i according to equation 2.9, where

$$\Lambda_i = \sqrt{\frac{\mathrm{tr}\left(\boldsymbol{B}_{e,i}\right)}{3}} = \sqrt{\frac{\mathrm{tr}\left(\boldsymbol{\sigma}_{e,i}\right)}{3G_i}} \tag{2.14}$$

since by definition $\mathrm{tr}(\boldsymbol{S}_i) = 1$. Thus, equation 2.8 can be converted into two separate evolution equations for $\boldsymbol{S}_i$ and Λ_i. A class of constitutive models known as the Pom-Pom models are particularly interesting because there the distinction between molecular orientation and stretch processes was explicitly made, on the basis of a physical picture of the molecular architecture, in the equations describing the orientation and stretch relaxation processes.

Table 2.2: Formulation of some differential constitutive models, using the concept of a slip tensor.

Viscoelastic stress	$\overset{\nabla}{\boldsymbol{\sigma}}_e + \boldsymbol{A}\cdot\boldsymbol{\sigma}_e + \boldsymbol{\sigma}_e\cdot\boldsymbol{A}^T = \boldsymbol{O}$					
Slip tensor	$\boldsymbol{A} = \alpha_0\boldsymbol{D} + \alpha_1\boldsymbol{\sigma}_e + \alpha_2\boldsymbol{\sigma}_e^{-1} + \alpha_3\boldsymbol{I}$					
Model	α_0	α_1	α_2	α_3	λ	References
Johnson–Segalman[1]	ζ	0	$-\frac{G}{2\lambda}$	$\frac{1}{2\lambda}$	constant	[75,87]
Leonov[2]	0	$\frac{1}{4G\lambda}$	$-\frac{G}{4\lambda}$	$-\frac{\mathrm{tr}(\boldsymbol{\sigma}_e)-G^2\mathrm{tr}(\boldsymbol{\sigma}_e^{-1})}{12G\lambda}$	constant	[75,87]
Giesekus	0	$\frac{\alpha}{2G\lambda}$	$-\frac{(1-\alpha)G}{2\lambda}$	$\frac{1-2\alpha}{2\lambda}$	constant	[75,87]
Phan-Thien–Tanner[1,2]	ζ	0	$-\frac{G}{2\lambda}$	$\frac{1}{2\lambda}$	$\begin{cases}\lambda_0\exp\left[-\frac{\beta}{G}\mathrm{tr}\,(\boldsymbol{\tau}_e)\right]\\ \lambda_0\left[1+\frac{\beta}{G}\mathrm{tr}\,(\boldsymbol{\tau}_e)\right]\end{cases}$	[75,87]
Extended Pom-Pom[3]	0	$\frac{\alpha}{2G\lambda_{0b}}$	$-\frac{(1-\alpha)G}{2\lambda_{0b}}$	$\frac{1}{2\lambda}$	$\left[\frac{1-\alpha-3\alpha\Lambda^4\boldsymbol{S}:\boldsymbol{S}}{\lambda_{0b}\Lambda^2}+\frac{2}{\lambda_s}\left(1-\frac{1}{\Lambda^2}\right)\right]^{-1}$	[125,126]
Extended Pom-Pom (double-equation form)	$\overset{\nabla}{\boldsymbol{S}} + 2\left(\boldsymbol{D}:\boldsymbol{S}\right)\boldsymbol{S} + \frac{1}{\lambda_{0b}\Lambda^2}\left[3\alpha\Lambda^4\boldsymbol{S}\cdot\boldsymbol{S} + \left(1-\alpha-3\alpha\Lambda^4\boldsymbol{S}:\boldsymbol{S}\right)\boldsymbol{S} - \frac{1-\alpha}{3}\boldsymbol{I}\right] = \boldsymbol{O}$ $\dot{\Lambda} = \Lambda\left(\boldsymbol{D}:\boldsymbol{S}\right) - \frac{1}{\lambda_s}\left(\Lambda-\frac{1}{\Lambda}\right)$					[125,126]

[1] In these models $\lambda\overset{\square}{\boldsymbol{\sigma}}_e + \boldsymbol{\sigma}_e = G_{GS}\boldsymbol{I}$, using the Gordon–Schowalter derivative (see table 2.1) and the modulus $G_{GS} = (1-\zeta)^{-1}G$. The definitions $\boldsymbol{\sigma}_e = G_{GS}\boldsymbol{B}_e$ and $\boldsymbol{\tau}_e = \boldsymbol{\sigma}_e - G_{GS}\boldsymbol{I}$ assure that $\lambda\overset{\square}{\boldsymbol{\tau}}_e + \boldsymbol{\tau}_e = 2G\lambda\boldsymbol{D}$ [66]. The Gordon–Schowalter derivative reduces to the other derivatives listed in table 2.1 for specific values of the slip parameter ζ. We get the upper convected Maxwell model for $\zeta = 0$, the lower convected Maxwell model for $\zeta = 2$, and the corotational Maxwell model for $\zeta = 1$.

[2] Table 4.4.2 of Macosko [75] contains some errors. For the Leonov model, $\boldsymbol{I}$ must be replaced by $G\boldsymbol{I}$ throughout the definition of $\boldsymbol{f}_d$. For the Phan-Thien–Tanner model, $\boldsymbol{f}_d$ should read $\lambda^{-1}(\exp[\beta G^{-1}\mathrm{tr}(\boldsymbol{\tau})] - 1)\boldsymbol{\tau}$. Furthermore, $\boldsymbol{f}_c$ should be multiplied by $\boldsymbol{\tau}$ for the White–Metner model and replaced by $2f[\boldsymbol{\tau} + G\boldsymbol{I}]$ for Larson's model, with f from equation A5, A6, or A7 of Peters and Baaijens [87].

[3] The stretch relaxation time λ_s in the XPP model depends on Λ (see equation 2.15). The expression given by Swartjes [110] for the generalized relaxation time λ_g, here denoted by λ, contains an error. The left-hand side of his equation 3.15 should read λ_g^{-1}.

The original Pom-Pom model of McLeish and Larson [77] was based on the Doi–Edwards tube model for linear polymer melts [27]. The pom-pom molecule has a simplified branched architecture, which serves as a model for long-chain branched polymers. It is visualised as a backbone, whose motion is confined to a tube determined by constraints imposed by the surrounding chains, with an equal number of branches at each of its two ends. Every mode $\boldsymbol{\tau}_{e,i}$ of the viscoelastic stress corresponds to a pom-pom molecule with a number of branches per end given by the parameter q_i. In this picture, $\boldsymbol{S}_i$ and Λ_i represent the orientation and stretch of a part of the backbone tube. The definition of the viscoelastic stress $\boldsymbol{\sigma}_{e,i}$ that McLeish and Larson used, in the differential form as well as in the integral form of the Pom-Pom model, differs from equation 2.10 by a constant. However, Rubio and Wagner [96] showed that equation 2.10 gives the correct expression for constitutive models based on a differential approximation of the Doi–Edwards model.

The extended Pom-Pom model (XPP) of Verbeeten *et al.* [125, 126] was based on the differential form of the original Pom-Pom model. The viscoelastic stress is calculated by equation 2.11 in combination with the evolution equations for the orientation tensor and the stretch parameter given in table 2.2. Alternatively, the XPP model can be written in a single-equation form, which is also shown in the table. One important improvement with respect to the original Pom-Pom model was the introduction of an exponential decay of the stretch relaxation time with increasing stretch of the contour length of the backbone tube,

$$\lambda_{s,i}(t) = \lambda_{0s,i}\exp\left[-\nu_i\left(\Lambda_i(t) - 1\right)\right], \tag{2.15}$$

where $\nu_i = 2/q_i$. The orientation relaxation time $\lambda_{0b,i}$ is constant. Experimental data for two LDPE melts, obtained in a range of flow types, were fitted accurately by Verbeeten *et al.* [125, 126] without having to change the fitting parameters for different flows. Surprisingly, they found that the XPP model also performed reasonably well for HDPE, which has a linear molecular structure. The formulation of the stretch relaxation law was modified later (see chapter 5 of [125]) to improve the convergence of contraction flow simulations, which had turned out to be problematic. This new version of the XPP model is also the one presented in table 2.2. The references [110] and [126] use the older version.

2.2 Modeling crystallizing polymers as suspensions

The mechanical behavior of an undercooled polymer melt gradually changes as more and more molecules are incorporated in newly formed nuclei or in the already present crystalline phase(s). The morphology that develops as nuclei grow into crystallites with distinct shapes agrees with the basic concept of a particle suspension: isolated particles (the crystallites) are scattered throughout a continuous matrix (the amorphous phase). Theories of suspension mechanics have therefore been used in the context of flow-induced crystallization [11, 12, 111, 112].

In this section, we introduce the concept of a crystallizing polymer as a suspension, where the amorphous matrix is characterized by the moduli $G_{0,i}$ and relaxation times $\lambda_{0,i}$, whereas the semicrystalline particle phase is characterized by the moduli $G_{1,i}$ and relaxation times $\lambda_{1,i}$. Both spectra may change during the crystallization process; the first by the development of noncrystalline structures within the amorphous phase and the latter by perfection of the semicrystalline structure. These phenomena are briefly discussed in section 2.2.5. Perfection will be left out of consideration in the simulations presented in chapter 3, where we mainly look at the early stage of crystallization, which is characterized by nucleation and growth. A more detailed discussion of modeling structure development within the amorphous phase is postponed to section 2.4.3. The reason for this is that a theoretical picture of the kinetics of flow-induced nucleation, which will be introduced in section 2.4.2, is needed.

Before proceeding to the rheology of viscoelastic suspensions, which is still a largely unexplored area, a number of results obtained for the more extensively studied case of a suspension of elastic particles in an elastic matrix will be discussed here.

2.2.1 Classical elastic suspension theory

The effective modulus of a suspension of elastic particles in an elastic matrix, also called a composite, is generally expressed in the form

$$G(\phi) = f_G\left(\phi, G_0, \nu_0, \underset{\sim}{\beta}, G_1, \nu_1, \ldots\right) G_0\,, \tag{2.16}$$

where ϕ represents the volume fraction of the particles or, in the present context, the crystallites and ν denotes the Poisson ratio. The subscripts 0 and 1 refer to the suspension at $\phi = 0$ and at $\phi = 1$. The ratio $f_G = G/G_0$ is commonly referred to as the relative modulus, while G is called the effective

modulus. In general, f_G not only depends on the volume fraction and the mechanical properties of the individual phases, but also on the geometry of the particles, expressed by a set of shape factors $\underset{\sim}{\beta} = [\beta_1\ \beta_2\ \ldots\ ]$.

Kerner [62] derived an expression for the relative shear modulus of a suspension of elastic spheres in an elastic matrix, where the particles could belong to an arbitrary number of different phases with different material properties. When only one particle phase is present, it reads

$$f_G = \frac{7 - 5\nu_0 + (8 - 10\nu_0)\frac{G_1}{G_0} + (7 - 5\nu_0)\left(\frac{G_1}{G_0} - 1\right)\phi}{7 - 5\nu_0 + (8 - 10\nu_0)\frac{G_1}{G_0} - (8 - 10\nu_0)\left(\frac{G_1}{G_0} - 1\right)\phi}. \tag{2.17}$$

Uemura and Takayanagi [120] obtained the same result. However, their expression for the effective Poisson ratio differs from Kerner's. On the basis of a composite spheres model, where the suspension is viewed as an assembly of spherical unit cells, each consisting of a particle surrounded by a concentric shell of the matrix material, Hashin [37] derived upper and lower bounds on the relative bulk modulus and found that these converged to the exact solution

$$f_K(\phi) = 1 + \frac{3(1 - \nu_0)\left(\frac{K_1}{K_0} - 1\right)\phi}{3(1 - \nu_0) + (1 + \nu_0)\left(\frac{K_1}{K_0} - 1\right)(1 - \phi)}. \tag{2.18}$$

The effective Poisson ratio follows from the effective moduli according to

$$\nu = \frac{3K - 2G}{6K + 2G}. \tag{2.19}$$

Hashin only obtained upper and lower bounds on the relative shear modulus of an elastic suspension of spheres. More general bounds, applicable to any macroscopically isotropic elastic suspension, were later derived by Hashin and Shtrikman [38] and Walpole [128]. Christensen and Lo [19] pointed out that the relative shear modulus given by equation 2.17 is not exact, but coincides with the lower bound derived in these works.

In the limiting case of a dilute suspension of spheres, equations 2.17 and 2.18 reduce to the results of Eshelby [32],

$$\lim_{\phi \to 0} f_G(\phi) = 1 + \frac{15(1 - \nu_0)\left(\frac{G_1}{G_0} - 1\right)\phi}{7 - 5\nu_0 + (8 - 10\nu_0)\frac{G_1}{G_0}} \tag{2.20}$$

and

$$\lim_{\phi \to 0} f_K(\phi) = 1 + \frac{3(1 - \nu_0)\left(\frac{K_1}{K_0} - 1\right)\phi}{3(1 - \nu_0) + (1 + \nu_0)\left(\frac{K_1}{K_0} - 1\right)}. \tag{2.21}$$

Evaluating equations 2.17, 2.18, 2.20, and 2.21, some interesting features are observed:

1. The shear moduli of the individual phases only appear in the relative shear modulus f_G via their ratio G_1/G_0. Similarly, for the relative bulk modulus f_K, the ratio K_1/K_0 is important.

2. The relative shear modulus f_G is independent of the moduli of the individual phases if $G_1 << G_0$ (voids) or $G_1 >> G_0$ (rigid particles). If, in the latter case, $\phi \rightarrow 0$ and $\nu_0 = 0.5$ then equation 2.20 becomes equal to Einstein's dilute suspension model for rigid spheres in an incompressible matrix: $f_G = 1 + 2.5\phi$.

3. As $\phi \rightarrow 1$, f_G and f_K become linearly proportional to G_1/G_0 and K_1/K_0, respectively. The correct results $f_G = G_1/G_0$ and $f_K = K_1/K_0$ are obtained at $\phi = 1$.

4. The effective shear and bulk moduli are independent of the Poisson ratio of the particles. On the other hand, the Poisson ratio of the matrix remains present in the expression for f_G (though not in the one for f_K) as $\phi \rightarrow 1$, and only cancels out exactly at $\phi = 1$, which is not realistic.

Kerner forced the Poisson ratio of the matrix to vanish by replacing the matrix properties by the effective properties of the suspension in going to $\phi = 1$, which in the case of a single particle phase simply yields $f_G = G_1/G_0$. Uemura and Takayanagi, on the other hand, proposed to use equation 2.17 with the indices 0 and 1 interchanged and ϕ replaced by $1 - \phi$. The packed spheres are then assumed to form a continuous matrix, while the actual matrix material in the interstitial spaces is treated as the particle phase. A second relative modulus, describing the high-concentration behavior of the suspension, is therefore introduced according to

$$h_G = \frac{G}{G_1} = \frac{7 - 5\nu_1 + (8 - 10\nu_1)\frac{G_0}{G_1} + (7 - 5\nu_1)\left(\frac{G_0}{G_1} - 1\right)(1 - \phi)}{7 - 5\nu_1 + (8 - 10\nu_1)\frac{G_0}{G_1} - (8 - 10\nu_1)\left(\frac{G_0}{G_1} - 1\right)(1 - \phi)}. \quad (2.22)$$

Analogous to equation 2.20, in the limit $\phi \rightarrow 1$ it follows that

$$\lim_{\phi \rightarrow 1} h_G(\phi) = 1 + \frac{15(1 - \nu_1)\left(\frac{G_0}{G_1} - 1\right)(1 - \phi)}{7 - 5\nu_1 + (8 - 10\nu_1)\frac{G_0}{G_1}}. \quad (2.23)$$

The same procedure is carried out for the relative bulk modulus, thus defining a solution $h_K = K/K_1$ for high volume fractions.

Uemura and Takayanagi [120] compared the predictions of equations 2.17 and 2.22 to experimental data for blends of polyethylene and poly(1-butene). The materials were assumed incompressible ($\nu_0 = \nu_1 = 0.5$). The expressions for the relative shear modulus were reformulated in terms of the dynamic viscosity: f_{η^*} from equation 2.17 for the low-concentration behavior and h_{η^*} from equation 2.22 for the high-concentration behavior, with the elastic shear moduli in these expressions replaced by dynamic viscosities. Replacing elastic shear moduli by static viscosities is justified if pressure gradients and inertia effects can be neglected. The correspondence principle, which will be discussed in section 2.2.3, was then applied to replace these static viscosities by dynamic viscosities. Since the components were both liquid, and therefore could both form the dispersed phase depending on the volume fraction, equation 2.22 was the exact high-concentration solution to the problem studied. Excellent agreement with the data, corresponding to two different temperatures, was obtained for $0 \leq \phi \leq 0.4$ using f_{η^*} and for $0.8 \leq \phi \leq 1$ using h_{η^*}. In the range of intermediate volume fractions, the experiments showed a zero-shear viscosity in between the limiting solutions. The same qualitative behavior is observed in crystallizing polymer melts, where the storage modulus is often measured in order to characterize the evolution of crystallinity. At some point, the storage modulus starts to increase, then it rises steeply, and eventually it levels off.

In liquid-liquid suspensions, this transition from low-concentration to high-concentration behavior is related to phase inversion, which means that droplets coalesce and gradually form a new matrix, while the former matrix is reduced to isolated droplets. In suspensions of solid particles, the transition is determined by a percolation threshold rather than phase inversion, since the particles do not coalesce upon impingement. Consequently, using equation 2.22 at high volume fractions, two things are neglected. First, whereas the model was derived for spherical particles, the newly defined particles, formed by what is in fact the matrix material, are not spherical. The resulting error is probably insignificant if these particles are small. Secondly, bodies with no edges, such as spheres, cannot possibly enclose a region in three-dimensional space. Therefore, the newly defined particles are interconnected. But in a crystallizing melt, where impinged crystallites continue to grow in the free directions, isolated amorphous regions can be created. Thus, it is conceivable that the sudden strong hardening of the material is due to a process with characteristics of a phase inversion as well as a percolation threshold. Finally, a disadvantage of simply switching the phases in equation 2.17 to obtain equation 2.22 is that this method does not provide a solution for highly concentrated suspensions with multiple particle phases, e.g. different crystalline phases in the present context, unless one of these has such

a high volume fraction in comparison with the others that it is reasonable to assume that this phase alone constitutes the homogeneous matrix. A reasonable first approximation might be to assume that all crystalline phases have the same mechanical properties and simply treat them as a single dispersed phase in the suspension model.

The results of Uemura and Takayanagi [120] were obtained from dynamic viscosity measurements in the limit of zero frequency. This probably explains the rather large range of volume fractions in which their experimental data were predicted by equation 2.17. However, in general, this model is only accurate for $\phi << 1$.

Two main strategies to determine f_G at higher volume fractions exist. On one hand, dilute suspension theories ($f_G \sim \phi$) have been extended to higher volume fractions by incorporating higher-order effects like interactions between particles (typically $f_G \sim \phi^2$). For example, Shaqfeh and Fredrickson [102] calculated the effective viscosity of a suspension of randomly oriented, rigid fibers in a viscous liquid by taking the scattering of elastic waves from multiple fibers into account. For the case of spherical particles suspended in a Newtonian liquid, Phan-Thien *et al.* [89, 91] approached the effect of hydrodynamic interactions as a lubrication problem involving pairs of particles. Models of this kind are usually valid in the semidilute regime, which extends up to $\phi \approx 0.45$ if a 10% error is allowed and the model is $\mathcal{O}(\phi^2)$ accurate, but not in the highly concentrated regime. For elastic composites, Torquato [117] derived exact series expansions for the effective shear and bulk moduli in terms of an infinite set of probability functions $S_n^{(p)}$, that give the probability of finding n points in the same phase p. Truncating the series after the third-order terms, the predicted relative moduli agreed very well with numerical simulations of two- and three-dimensional composites, except for the case of rigid particles in an incompressible matrix, where the predictions deviated from the simulations for $\phi > 0.6$ [118].

On the other hand, several researchers have developed approximate micromechanical models based on a so-called effective medium method, where a model system with a simplified morphology is generally taken as the starting point for determining the effective properties of the suspension. Because of this simplification, effective medium methods are easily implemented in comparison to models based on a more realistic picture of the actual microstructure. Moreover, no parameters other than the mechanical properties of the constituent phases, and shape factors for nonspherical particles, are needed. Two of these effective medium methods have been taken from the literature and will be discussed next. The first is the differential effective medium approximation, which has the advantage that it is simple in concept and im-

plementation. The second is known as the generalized self-consistent method. While its mathematical formulation is more complex, it has also proved more successful in predicting elastic properties of suspensions, of spheres as well as fibers, up to $\phi = 1$. A test of the performance of these models with respect to polymer crystallization experiments is postponed to chapter 3.

2.2.2 Effective medium methods

Differential effective medium approximation (DEMA)

The DEMA [20,82,83,90] is based on a simple scheme. It is imagined that an infinitesimal amount of particles is added to the pure matrix. The effective mechanical properties are calculated with a dilute suspension model. The effective medium thus obtained is considered the homogeneous matrix and again an infinitesimal amount of new particles is added. The previous steps are repeated until the correct total volume fraction is reached. At any stage, the sizes of the new particles should be considerably greater than those of the previously added ones for the assumption of a homogeneous matrix to be valid [90].

The relative moduli of a dilute suspension of elastic spheres in an elastic matrix were derived by Eshelby [32]. The results were given in equations 2.20 and 2.21. For non-spherical particles, one or more shape factors β_i enter the dilute suspension model. Here, however, we restrict our attention to suspensions of spheres to illustrate the concept of the DEMA. Departing from equations 2.20 and 2.21, the differential scheme for calculating the effective shear and bulk moduli is summarized in the coupled differential equations

$$\frac{\mathrm{d}G}{\mathrm{d}\phi} = \frac{15\,(1-\nu)\,(G_1 - G)}{(1-\phi)\left(7 - 5\nu + (8-10\nu)\,\frac{G_1}{G}\right)} \tag{2.24}$$

and

$$\frac{\mathrm{d}K}{\mathrm{d}\phi} = \frac{(K_1 - K)}{(1-\phi)\left(1 + \frac{K_1 - K}{K + \frac{4}{3}G}\right)}, \tag{2.25}$$

with the effective Poisson ratio given by equation 2.19. A peculiar case is when $\nu_0 = \nu_1 = 1/5$, equations 2.24 and 2.25 are decoupled and $\nu = 1/5$ for all values of ϕ [20,90].

Generalized self-consistent method (GSCM)

The basic idea common to all self-consistent methods is that a unit cell, containing the relevant characteristics of the microstructure of a suspension,

is thought to be embedded in a homogeneous medium with the effective properties to be determined. Several self-consistent methods have been proposed, for example for spherical and ellipsoidal particles by Berryman [9,10], for spherical particles and fibers by Hashin *et al.* [37,39], and for fibers by Hill [47–50].

The model discussed here was developed by Christensen and Lo [19] and is known as the generalized self-consistent method. For suspensions of spheres, the unit cell consists of a spherical particle, surrounded by a concentric shell of the matrix material. This unit cell is embedded in an infinitely extending effective medium. The effective mechanical properties of the suspension are found when the response of the model system to a prescribed stress or strain becomes equal to the response of a homogeneous system, i.e. when the properties of the unit cell and the effective medium become equal. It was found that the effective shear modulus of a suspension of elastic spheres in an elastic matrix follows from the equation

$$A f_G(\phi)^2 + B f_G(\phi) + C = 0\,, \tag{2.26}$$

The parameters A, B, and C depend on the Poisson ratios of both phases, the ratio of their respective shear moduli, and the volume fraction of particles; the expressions involved are contained in appendix A since they are quite lengthy. One of the two possible solutions to equation 2.26 can always be discarded as physically unrealistic. The other gives the relative shear modulus sought. The relative bulk modulus was found to be the same as in the composite spheres model of Hashin [37] (equation 2.18).

The GSCM can also be applied to fiber suspensions, as Christensen and Lo [19] demonstrated. The mechanical behavior of anisotropic elastic materials is described by a generalized form of Hooke's law where the single modulus is replaced by a fourth order stiffness tensor, which contains the moduli corresponding to different directions:

$$\boldsymbol{\tau} = {}^4\boldsymbol{C} : \boldsymbol{\epsilon}\,, \tag{2.27}$$

where ${}^4\boldsymbol{C}$ is the fourth-order stiffness tensor and $\boldsymbol{\epsilon}$ is a strain tensor.

Hashin and Rosen [39] and Hill [47,48] developed a theory for elastic suspensions of aligned fibers. They assumed transverse isotropy, which means that the effective moduli do not vary with respect to a rotation about the fiber axis. The mechanical behavior of the suspension can then be expressed in five independent effective moduli. The mentioned authors derived solutions for four of these moduli, but only obtained upper and lower bounds on the effective shear modulus in the transverse direction. Christensen and Lo used

the GSCM to determine this property. They defined an essentially two-dimensional unit cell consisting of a cylindrical particle, surrounded by a concentric shell of the matrix material, embedded in the infinitely extending effective medium. The relative transverse shear modulus was found to be the solution of an expression similar in form to equation 2.26, but with different parameters A, B, and C. These are also given in appendix A, along with the expressions for the remaining four relative moduli.

Christensen and Lo demonstrated that the elastic (transverse) shear modulus predicted by equation 2.26 lies between the appropriate upper and lower bounds derived by Hashin [37, 40, 44], Hashin and Shtrikman [38], and Walpole [128]. In a paper by Christensen [20], theoretical results for suspensions of rigid spheres were shown to correlate well with experimental data compiled by Thomas [114], where the highest volume fraction was approximately 0.7. In contrast, the predictions of the DEMA showed a large deviation from the data at volume fractions above 0.5. Segurado and Llorca [100] performed numerical simulations of elastic sphere-reinforced composites, where $0 \leq \phi \leq 0.5$, and compared their results to the predictions of the GSCM and Torquato's third-order approximation (TOA) [118]. Both models performed equally well when the particles were not rigid, except that the relative bulk modulus was predicted slightly more accurately by the TOA. For rigid spheres, the TOA provided better results.

In complex flows of crystallizing polymers, shishes and row crystallites are generally not oriented in a common direction but rotate according to the deformation gradients along their individual paths. This does not mean that the GSCM, which assumes that fibers are oriented along a common axis, becomes useless. In order to calculate the stress field resulting from a complex thermomechanical history, a finite element method is usually applied. The GSCM can then be used to calculate the effective moduli within each individual volume element, where the orientation of the fibers is assumed homogeneous and is obtained from the viscoelastic constitutive model. Analogous to equation 2.27, we can replace the viscoelastic modes of the total stress, as expressed in equation 2.11, by

$$\boldsymbol{\tau}_{e,i} = {}^4\boldsymbol{C}_i : (\boldsymbol{B}_{e,i} - \boldsymbol{I}) \; . \tag{2.28}$$

Another possible formulation, which looks similar but may yield very different results, is given by

$$\boldsymbol{\tau}_{e,i} = {}^4\boldsymbol{C}_i : \boldsymbol{B}_{e,i} - G_i \boldsymbol{I} \; . \tag{2.29}$$

It will be assumed that the longitudinal axes of the fibers coincide with the direction corresponding to the highest eigenvalue of the local elastic Finger tensor. In flow-induced crystallization experiments, spherulites and oriented

crystallites are usually present at the same time, i.e. locally there is a mixture of the two that varies with time and position. In that case we propose to determine the effective properties of that part of the material which consists of the amorphous phase and the spherulites first, applying the 3D GSCM, and to use the resulting effective medium as the matrix in the 2D GSCM to account for the additional filler effect due to the oriented crystallites.

2.2.3 Extension to linear viscoelasticity

Models for nondilute viscoelastic suspensions subjected to arbitrary flows are not available, due to the complex nature of the problem, but rigorous bounds on the effective dynamic moduli were derived in a series of papers by Gibiansky *et al.* [34,35] and Milton and Berryman [78]. In the range of linear viscoelasticity the correspondence principle, developed by Hashin [41–43] and Christensen [18], can be used. In their derivation, these authors departed from the constitutive model of a linear viscoelastic material, which is given by the Boltzmann integral

$$\boldsymbol{\tau}(t) = \int_{-\infty}^{t} 2G(t-t')\,\dot{\boldsymbol{\epsilon}}(t')\,dt', \tag{2.30}$$

where $\boldsymbol{\epsilon}$ is the strain tensor. Taking the Laplace transform of equation 2.30 yields, according to the convolution theorem,

$$\tilde{\boldsymbol{\tau}}(s) = 2s\tilde{G}(s)\,\tilde{\boldsymbol{\epsilon}}(s) \tag{2.31}$$

with s the Laplace variable. Equation 2.31 has the form of Hooke's law. The solution to any linear viscoelastic problem can thus be found by transforming the constitutive equation to the Laplace domain, where $s\tilde{G}(s)$ plays the role of the elastic shear modulus, replacing the boundary conditions by their appropriate transforms, solving the resulting elastic problem, and finally transforming back to the time domain. Now suppose that the material is subjected to a steady harmonic oscillation

$$\boldsymbol{\epsilon}^*(\omega) = \boldsymbol{\epsilon}_0 \mathrm{e}^{j\omega t}. \tag{2.32}$$

The stress response is then given by

$$\boldsymbol{\tau}^*(j\omega) = G^*(j\omega)\,\boldsymbol{\epsilon}^*(j\omega), \tag{2.33}$$

where G^* is the dynamic modulus. Equation 2.33 has the same functional dependence on $j\omega$ as equation 2.31 has on s. Since there is no objection to taking $s = j\omega$ in equation 2.31, the correspondence principle applies,

which can be formulated as follows: *For a linear viscoelastic suspension of fixed volume fraction, the effective dynamic modulus is obtained by replacing elastic moduli by dynamic moduli in the model of an elastic suspension with the same structural geometry.* According to Tanner [112], who proposed a suspension model for crystallizing polymers, the correspondence principle will still be a good approximation if ϕ changes slowly compared to the molecular relaxation processes.

Equation 2.16 is now replaced by

$$G^*(\omega,\phi) = f_G^*\left(\phi, G_0^*(\omega), \nu_0, \underset{\sim}{\beta}, G_1^*(\omega), \nu_1, \ldots\right) G_0^*(\omega) \; . \tag{2.34}$$

The Poisson ratios are assumed real numbers, which is a common assumption. Agbossou *et al.* [3] explored the possibilities of mechanical modeling of suspensions allowing the Poisson ratio of the matrix, and hence the effective Poisson ratio, to be complex. This method will be left out of consideration here, but it can easily be included. It is important to note that the relative modulus f_G^* is now a complex quantity. With the abbreviations $f_G' = \mathrm{Re}\{f_G^*\}$ and $f_G'' = \mathrm{Im}\{f_G^*\}$, the effective modulus is written as

$$G^* = f_G' G_0' - f_G'' G_0'' + j\left(f_G'' G_0' + f_G' G_0''\right) \; . \tag{2.35}$$

Dickie *et al.* [24–26] used the correspondence principle according to equation 2.34 in combination with the elastic suspension model derived by Kerner [62] and Uemura and Takayanagi [120], which is expressed in equation 2.17. If $\nu_0 = \nu_1 = 0.5$, the result is equivalent to the more recent incompressible linear viscoelastic suspension model of Palierne [85] in the special case of vanishing interfacial tension [36]. Dickie *et al.* introduced composite particles (made up of both phases) to simulate partial phase inversion and a maximum packing fraction to correct for interactions between particles. The experimentally determined dynamic moduli of different suspensions of spherical polymeric particles in polymeric matrices, as a function of temperature and composition, could be fitted qualitatively by this approach.

Tanner [112] stated that the correspondence principle implies that all moduli of the relaxation spectrum are increased in proportion to a real number $f_G(\phi)$, while the relaxation times do not change with ϕ. Looking at equation 2.17 again, and substituting dynamic moduli for static elastic moduli, it is seen that this is only true in suspensions of rigid particles ($|G_1^*| >> |G_0^*|$) or voids ($|G_1^*| << |G_0^*|$). The ratio G_1^*/G_0^* then drops out of the right-hand side of the equation and f_G^* becomes real. Consequently

$$G^* = f_G(\phi)\, G_0^* = f_G(\phi)\, G_0' + j f_G(\phi)\, G_0'' \, , \tag{2.36}$$

where $f_G = f'_G = f^*_G$, and hence

$$G'(\omega) = \sum_i^M f_G(\phi)\, G_{0,i} \frac{\lambda_{0,i}^2 \omega^2}{1 + \lambda_{0,i}^2 \omega^2} \tag{2.37}$$

and

$$G''(\omega) = \sum_i^M f_G(\phi)\, G_{0,i} \frac{\lambda_{0,i} \omega}{1 + \lambda_{0,i}^2 \omega^2}\,. \tag{2.38}$$

Thus, the moduli G_i in equation 2.11 may be written as $G_i = f_G(\phi) G_{0,i}$. The validity of equation 2.17 is restricted to low volume fractions. But the same conclusions can be drawn for models of semidilute and highly concentrated suspensions, which share with dilute suspension models the fact that not the absolute values of the phase moduli, but their ratio is important. For a suspension of voids, this ratio (G_1^*/G_0^* in the linear viscoelastic case considered here) will vanish. For a suspension of rigid particles, it becomes infinitely large. In any realistic suspension model, the ratio of the phase moduli then must drop out of the expression for the relative modulus, since f_G^* should only become infinite in the limit $\phi \to 1$. The models considered in this thesis all meet this requirement.

It is interesting in this respect to look at the work of See *et al.* [99], who investigated suspensions of polyethylene spheres in silicon oil and in a polymer solution. In both cases, i.e. for a viscous matrix and for a viscoelastic matrix, they found that the relative viscosities, storage moduli, and loss moduli could be described by a single real function $f(\phi) = \eta/\eta_0 = G'/G'_0 = G''/G''_0$ that was predicted by a constitutive model based on pairwise interactions between particles (see also Phan-Thien *et al.* [89, 91]). The range of investigated volume fractions extended from $\phi = 0$ up to $\phi = 0.4$. In the light of the above discussion, the result of See *et al.* is explained by the high moduli of the solid particles compared to the matrix fluids used in their experiments.

In numerical simulations of flow-induced crystallization processes where the crystallites cannot be assumed rigid, so that equations 2.37 and 2.38 do not hold, it will be necessary (in the time interval where ϕ increases significantly) to calculate the effective dynamic modulus for different frequencies by means of a viscoelastic suspension model and to obtain a new relaxation spectrum from these dynamic data. In this way the moduli G_i and relaxation times λ_i, needed in the constitutive model, can be found.

2.2.4 Preliminary nonlinear viscoelastic modeling

Formally, the correspondence principle is only valid in the range of linear viscoelasticity. In nonlinear viscoelastic constitutive models for polymer melts,

the moduli and relaxation times of the linear relaxation spectrum are generally retained, while a number of additional parameters are introduced to capture the nonlinear phenomena. It will be assumed that the correspondence principle still applies to the linear viscoelastic part of the mechanical behavior. Tanner [112] proposed a similar generalization by assuming that, also in a nonlinear viscoelastic constitutive model, the moduli $G_{0,i}$ of the amorphous phase can be replaced by $f_G(\phi)G_{0,i}$, while leaving the basic structure of the model intact. It was shown in the previous section that this assumption is invalid, even in the linear viscoelastic regime, if the crystallites cannot be assumed rigid. Although the modulus of the final semicrystalline phase exceeds the modulus of the amorphous phase by several decades, the assumption of rigidity is probably not realistic in earlier stages of the crystallization process, when the semicrystalline phase is still highly imperfect. However, in this section, Tanner's simplifying approach will be followed in order to illustrate the basic concept of a nonlinear viscoelastic suspension model. For deformable crystallites, the spectrum (moduli *and* relaxation times) should be updated as space filling, which plays the role of the volume fraction in the suspension model, evolves.

Of the differential constitutive models summarized in table 2.2, only the Leonov model is completely determined by the linear viscoelastic relaxation spectrum. The other models all contain one or more additional parameters, related to the nonlinear viscoelastic part of the mechanical behavior. The possible dependence of these parameters on space filling, degree of crystallinity, and microstructure of a crystallizing polymer has not been explored yet. In section 2.4.3, the branching parameter q of the XPP model will be related to the structure that develops in the amorphous phase during flow-induced crystallization.

Mall-Gleissle *et al.* [76] investigated suspensions of glass spheres in silicon oil subjected to simple shear flow. They observed that the first normal stress difference $N_1 = \tau_{11} - \tau_{22}$ depended on the shear stress as $N_1 \sim \tau_{12}^n$ with $1.63 \leq n \leq 1.68$. Upon increasing the volume fraction of particles, while keeping the shear stress constant, N_1 decreased. Hwang *et al.* [54] simulated suspensions of rigid particles in an Oldroyd-B fluid and found a similar scaling with $n = 2$. Furthermore, the normal stress difference and the shear viscosity were observed to increase with the volume fraction of particles as well as the shear rate. A phenomenological modeling approach, proposed by Peters [86], is followed here in an attempt to capture the essentials of the mentioned experimental and numerical results. For illustrative purposes, we start with an upper convected Maxwell model for the viscoelastic stress in the suspension,

$$\lambda \overset{\nabla}{\boldsymbol{\tau}}_e + \boldsymbol{\tau}_e = 2G f_1(\phi)\, f_2(\phi, \dot{\gamma})\, \boldsymbol{D}\,. \tag{2.39}$$

The effective modulus is related to the volume fraction of particles as $f_1 G$, where f_1 follows from the linear viscoelastic suspension model as discussed in the previous section. Moreover, it is assumed that the distortion of the velocity field by the presence of particles can be captured by a second scalar f_2, depending on the volume fraction ϕ and the shear rate $\dot{\gamma} = \sqrt{2\boldsymbol{D} : \boldsymbol{D}}$. Thus, an effective rate of deformation tensor $f_2 \boldsymbol{D}$ is introduced. The following results are obtained for the effective viscosity in simple shear flow,

$$\eta = \frac{\tau_{12}}{\dot{\gamma}} = G f_1 f_2 \lambda \,, \tag{2.40}$$

and the effective first normal stress coefficient,

$$\Psi_1 = \frac{N_1}{\dot{\gamma}^2} = 2 G f_1 f_2^2 \lambda^2 \,. \tag{2.41}$$

The relative viscosity and the relative first normal stress coefficient are thus given by

$$\eta_r = \frac{\eta}{\eta_0} = f_1 f_2 \tag{2.42}$$

and

$$\Psi_{1r} = \frac{\Psi_1}{\Psi_{1,0}} = f_1 f_2^2 \,, \tag{2.43}$$

respectively. The notation used by Hwang *et al.* is followed here in the definitions of the relative properties. In accordance with their results, the ratio

$$\frac{\Psi_{1r}}{\eta_r^2} = \frac{1}{f_1} \tag{2.44}$$

is independent of the shear rate. Hence, the trend observed experimentally may be captured by the rather simple phenomenological model expressed in equation 2.39. Because an upper convected Maxwell model was used, the second normal stress difference $N_2 = \tau_{22} - \tau_{33}$ equals zero. This is not in accordance with the data of Mall-Gleissle *et al.* [76], where a negative N_2 was found, whose absolute value showed the same qualitative dependence on τ_{12} as N_1.

The method outlined above can be extended to more advanced nonlinear viscoelastic constitutive models, such as those listed in table 2.2. If $\boldsymbol{\sigma}_e \cdot \boldsymbol{\sigma}_e$ terms appear in the constitutive equation for the stress, i.e. if $\alpha_1 \neq 0$, no explicit expressions for the shear viscosity and relative normal stress differences can be derived. Exceptions are the Johnson–Segalman (JS) and Phan-Thien–Tanner (PTT) models, which yield the shear viscosity

$$\eta = \frac{G f_1 f_2 \lambda}{1 + \zeta (2 - \zeta) f_2^2 \lambda^2 \dot{\gamma}^2} \tag{2.45}$$

and the normal stress coefficients

$$\Psi_1 = \frac{2Gf_1f_2^2\lambda^2}{1+\zeta\,(2-\zeta)\,f_2^2\lambda^2\dot{\gamma}^2} \tag{2.46}$$

and

$$\Psi_2 = \frac{N_2}{\dot{\gamma}^2} = \frac{-\zeta Gf_1f_2^2\lambda^2}{1+\zeta\,(2-\zeta)\,f_2^2\lambda^2\dot{\gamma}^2}\,. \tag{2.47}$$

The ratio of the relative first normal stress coefficient and the squared relative viscosity is then obtained as

$$\frac{\Psi_{1r}}{\eta_r^2} = \frac{1+\zeta\,(2-\zeta)\,f_2^2\lambda^2\dot{\gamma}^2}{f_1\left[1+\zeta\,(2-\zeta)\,\lambda^2\dot{\gamma}^2\right]}\,. \tag{2.48}$$

The difference between the JS and PTT models is that, in the PTT model, λ is a function of $\mathrm{tr}(\boldsymbol{\tau}_e)$. Comparing equation 2.48 to equation 2.44 it is seen that, if the slip parameter $\zeta \neq 0$, the ratio Ψ_{1r}/η_r^2 depends on the shear rate and the relaxation time, which are combined in the dimensionless Weissenberg number

$$We = \dot{\gamma}\lambda\,, \tag{2.49}$$

as well as on the volume fraction.

It will be interesting to test the performance of the proposed method in simulating flow-induced crystallization processes. But that is beyond the scope of the present work, where we will look at crystallization during short-term deformation experiments (chapter 3) because then the processes of nucleation and space filling do not overlap in time, which allows us to study them separately.

2.2.5 Concluding remarks

A framework for a constitutive model for the stress in a crystallizing polymer, based on suspension mechanics, has been established. The evolution of the effective linear viscoelastic properties of the material as a function of the volume fraction of crystallites is determined by the relative dynamic modulus $G^*/G_0^* = f_G^*(\phi,\ldots)$. Because this is generally a complex quantity, both the effective moduli *and* the effective relaxation times will change. In chapter 3, one of the suspension models discussed above, i.e. a specific expression for f_G^*, will be chosen after comparison of the dynamic mechanical response predicted by these models to the one measured during quiescent and flow-induced crystallization experiments.

Suspension theories provide an attractive means to account for the evolution of mechanical properties of a crystallizing polymer. It is important,

however, to note that a suspension theory may not be applicable, or will have to be modified, under certain conditions. This is due to the specific microstructures encountered in different stages of the polymer crystallization process. Some limitations to the proposed modeling, and possible modifications to remove these limitations, are discussed next.

Brownian motion

The influence of Brownian motion on the concentration dependence of material parameters may be significant in early stages of crystallization, when crystallites are still small. The material should then be treated as a colloid. In the quiescent state, typical colloidal particle sizes range from 10^{-9}m (i.e. one order greater than atomic size, in which case the material is considered a solution) to 10^{-7}m, whereas suspensions are made up of particles with a characteristic dimension of the order of one micron or higher. The importance of Brownian motion of a particle relative to the macroscopic flow is expressed in the dimensionless Péclet number [88, 121],

$$Pé = \frac{R^2\dot{\gamma}}{D}, \tag{2.50}$$

with $\dot{\gamma} = \sqrt{2\boldsymbol{D} : \boldsymbol{D}}$ the characteristic shear rate and D the diffusivity of the particle in a specific direction. The effect of Brownian motion is significant when $Pé$ is small, which is to be expected in slow flows of small particles. Spheres are characterized by a single diffusivity D_0 because of their three-dimensional rotational symmetry. The Stokes-Einstein relation gives D_0 as a function of temperature T, matrix viscosity η, and particle radius R according to

$$D_0 = \frac{k_B T}{6\pi\eta R}, \tag{2.51}$$

where k_B is Boltzmann's constant. In suspensions of orientable particles, or clusters of particles, multiple diffusivities have to be defined according to the different rotational and translational degrees of freedom. Rotational and translational diffusivities of axisymmetric particles of diverse shapes were derived by Brenner [15]. Many other experimental and theoretical works on the rheology of colloids have been published. Van der Werff and De Kruif [121] determined the dependence of shear viscosity on particle size, volume fraction, and shear rate. The introduction to their paper provides a useful review of publications up to 1989. In a comprehensive literature review from 1999 on the rheology of fiber suspensions, Petrie [88] also discussed theories of Brownian suspensions (i.e. colloids).

Structure development within the amorphous phase

From molecular dynamics simulations, Muthukumar [79, 80] concluded that the nucleation process is significantly influenced by the ability of polymer molecules to participate in multiple nuclei. This will be true either if the nucleation density is high, the average internuclear distance being at most of the order of the contour length of the longest molecules, or if the nuclei appear in clusters rather than being scattered evenly throughout the material. To our knowledge, no evidence of such clustering during quiescent crystallization exists. If nuclei are created in a spatially random manner, then, during a large part of the crystallization process, they will be too far apart to assign a significant probability to the event that one molecule is incorporated in two nuclei. In flow-induced crystallization, on the other hand, connectivity of the spherulites that form a row crystallite can be inferred from their tendency to stay together in spite of strong velocity gradients. But in the case of flow-induced point nucleation, analogous to nucleation in a quiescent melt, Muthukumar's statement may be questioned.

More generally, one could argue that in some range of degree of crystallinity the material will resemble a physical network rather than a suspension, because the crystallites are interlinked through the amorphous phase; at high nucleation densities by single chains but otherwise by sequences of entangled chain segments. Indeed, rheological measurements by Pogodina *et al.* [93] showed a gel point in the early stages of quiescent crystallization of isotactic polypropylene, which they attributed to the formation of a network of amorphous 'tie chains' linking the spherulites [95]. The time to reach the gel point was observed to decrease exponentially with increasing undercooling [93] and, in shear-induced crystallization, with increasing strain [94]. Tanner [112], who proposed a rheological model for crystallizing polymers based on suspension mechanics, acknowledged that materials with gel-like crystalline structures should be given further consideration.

Boutahar *et al.* [12] carried out rheological experiments on two structurally different crystallizing polymers: a suspension-like polypropylene and a colloid-like polyethylene. For the colloid-like sample, their dynamic measurements revealed a yield effect in the low frequency range, which manifested itself at the very beginning of the crystallization process, whereas in the suspension-like sample it was delayed until a critical volume fraction of spherulites ($\phi = 0.4$) had been reached. The authors related this latter yield effect to a percolation threshold caused by the formation of a physical network in between the spherulites. For the suspension-like sample, they noted that the critical volume fraction was close to the result obtained by Pike and Seager [92], who performed numerical simulations of percolation in suspensions

of spherical particles. The particles were considered bonded when within a certain distance from each other; a percolation threshold of $\phi = 0.3$ was calculated. But Boutahar *et al.* gave no explanation for the fact that the yield effect appeared immediately in the colloid-like sample. Nevertheless, their results qualitatively confirm the observation of Pogodina *et al.* [93–95] that physical gelation, characteristic of network formation, occurred before a dense packing ($\phi = 0.63$) had been accomplished.

Small-angle X-ray scattering (SAXS) and wide-angle X-ray scattering (WAXS) patterns obtained by Somani *et al.* [105, 106] during shear-induced crystallization of isotactic polypropylene were also interpreted by the authors as evidence for the existence of a network at the early stages. But it should be mentioned that they looked at strong flows, where oriented crystallites developed, whereas the previously mentioned results applied to spherical morphologies, developed in quiescent and weak flow conditions.

Janeschitz-Kriegl *et al.* [57, 58, 108] argued against the hypothesis of network formation in polymer crystallization. In their experiments on shear-induced and elongational flow-induced crystallization of isotactic polypropylene, where for the most part no oriented structures developed, the number of spherulites per unit volume was so small that any interlinking would extend over distances far greater than might reasonably be expected. But nevertheless, the number of nuclei increased nonlinearly as a function of the applied work, indicating that nucleation is a self-enhancing process. These data are in contradiction with the idea of a sample-spanning network and suggest that the flow-induced acceleration of nucleation kinetics is governed by a localized process, acting on isolated nuclei, rather than a global process that involves all nuclei together. Janeschitz-Kriegl *et al.* therefore developed a theory based on the hypothesis that flow promotes the activation of nuclei that already exist in the melt above the melting temperature, yet are unstable and consequently do not grow yet.

Another possible explanation can be found in the works of Zuidema *et al.* [131,132]. They assumed that nuclei act as physical crosslinks. Consequently, as crystallization progresses, the molecular structure of the melt essentially becomes increasingly branched. When a flow is applied, a more branched chain segment will be able to maintain stretch and orientation for a longer time, thereby locally increasing the probability that a new nucleus is created. Thus, rather than postulating the formation of a global network, nucleation is supposed to be enhanced in the vicinity of existing nuclei. Zuidema *et al.* related the nucleation rate to the recoverable part of the strain corresponding to the longest relaxation time of the melt and, in accordance with the idea of physical crosslinking, made this relaxation time a function of the number of flow-induced nuclei. As a result, flow-induced nucleation becomes a self-

enhancing process. This part of the modeling proposed by Zuidema *et al.* turned out to be essential for predicting flow-induced structure formation during injection molding.

A more detailed discussion of the athermal flow-induced nucleation proposed by Janeschitz-Kriegl *et al.* and the thermal flow-induced nucleation model of Zuidema *et al.* will be presented in section 2.4.3. First, we will turn to the modeling of the kinetics of quiescent and flow-induced crystallization.

Secondary crystallization

A final remark is made with respect to the modeling of spherulites and shish-kebabs as spheres and cylinders, respectively, in (suspension) theories of polymer crystallization. These objects, which we call crystallites, are not homogeneous, but actually consist of alternating crystalline lamellae and regions of amorphous material. Crystallization within these internal amorphous regions causes a hardening of the crystallites. As a result, the linear viscoelastic moduli G_1' and G_1'' of the semicrystalline phase, and probably the nonlinear viscoelastic rheological parameters as well, are not constant, but increase in time. This process, called perfection or secondary crystallization, is complementary to the processes of nucleation and growth [30].

Regular suspension theories do not consider any evolution of the mechanical properties of the constituent phases. Since the characteristic time scale of perfection is expected to be much larger than that of nucleation and growth, perfection is usually neglected during the space filling process. Theoretically, the earlier a crystallite started to grow from a nucleus, the further the hardening process will have advanced. Thus, an unequal distribution of mechanical properties among the crystallites is obtained. But if perfection is indeed a slow process compared to nucleation and growth, it may be assumed to alter the effective moduli only after they have reached their 'plateau values', i.e. when the semicrystalline phase fills the entire volume of the material. In the colloid-like sample studied by Boutahar *et al.* [12], where complete space filling by tiny spherulites of low degree of crystallinity was reached virtually instantaneously, perfection was the main process through which hardening of the material occurred. In the remainder of this thesis, perfection is left out of consideration. We will only investigate the crystallization process up to the moment when space filling is completed.

2.3 Quiescent crystallization

The equations governing the spatial transition from one phase to another, in a substance at rest and without any flow history, were derived independently by Kolmogorov [65] and Avrami [5–7]. They identified two processes: nucleation, i.e. the appearance of primordial entities (nuclei) of the new phase, and subsequent growth of these nuclei by attachment of molecules from the original phase to their surfaces. The Kolmogorov–Avrami theory is widely used in crystallization studies, although it sometimes appears in a modified form, for example to allow for expansion or shrinkage of the crystallizing material [8] or for temperature gradients [17, 29–31]. In the original theory, the overall progress of crystallization is fully characterized by a nucleation rate $\alpha(t)$ $[m^{-3}]$ and a crystal growth rate $G(t)$ $[ms^{-1}]$. The latter is integrated from a past time s to the current time t to get the current size $R(t,s)$, as measured in the direction of growth, of a crystallite created at s, assuming that its growth is not impeded by the presence of other crystallites. In the case of a spherulite, growing at the same rate in all directions, the expression

$$V(t,s) = \frac{4\pi}{3}\left[\int_{s^-}^{t} G(u)\, du\right]^3 \tag{2.52}$$

equals the volume of the spherulite under the aforementioned assumption. Avrami called this the extended volume [5]. Other terms, like undisturbed volume and unbounded volume, have also been used in literature. The latter designation will be used throughout the remainder of this thesis.

Equation 2.52 is modified to account for the fact that different growth rates may exist in different directions. Following Hütter *et al.* [53] we consider the common situation where crystal growth can be expressed in three time-dependent growth rates along the axes of a suitably defined Cartesian coordinate system $\{\vec{x}_1, \vec{x}_2, \vec{x}_3\}$. The unbounded volume of a crystallite is then given by

$$V(t,s) = c\int_{s^-}^{t} G_1(u)\, du \int_{s^-}^{t} G_2(v)\, dv \int_{s^-}^{t} G_3(w)\, dw\,. \tag{2.53}$$

The parameter c is a shape factor. For example, $c = 2\pi$ in the case of a disk or fiber growing in the axial direction at a rate $G_1(t) = dL/dt$, where L denotes half the length of the fiber or half the height of the disk, and in the radial direction at a rate $G_2(t) = G_3(t) = dR/dt$, with R the cross-sectional radius. For a spherulite with a radial growth rate $G_1(t) = G_2(t) = G_3(t) = dR/dt$, $c = 4\pi/3$ and equation 2.53 reduces to equation 2.52. The growth rates are taken equal to zero for $t < s$. If any of the dimensions R_n $(n = 1, 2, 3)$ of

a crystallite is constant for $t \geq s$, then the corresponding growth rate G_n is represented by a Dirac function,

$$G_n(t,s) = R_{0n}\delta(t-s) \;, \tag{2.54}$$

and consequently

$$R_n(t,s) = \int_{s^-}^{t} G_n(u)\, du = R_{0n}\mathcal{H}(t-s) \;, \tag{2.55}$$

where $\mathcal{H}(t-s)$ denotes the Heaviside step function centered at $t = s$.

The fraction of the total volume of material occupied by the crystalline phase is called space filling and is denoted by $\xi_g(t)$. It is related to the nucleation rate and the growth rate by the Kolmogorov–Avrami equation

$$\xi_g(t) = 1 - \exp\left[-c\int_{-\infty}^{t} \alpha(s)\, V(t,s)\, ds\right] . \tag{2.56}$$

Kolmogorov [65] and Avrami [5–7] arrived at this result by different approaches. For the derivation of Kolmogorov's theory of phase transformation kinetics, which is based on the treatment of nucleation as a stochastic process, one can turn to the works of Eder [29–31]. The subscript in ξ_g refers to the geometric approach to which this derivation reduces in the limiting case of small temperature gradients. The integral in equation 2.56 represents the total volume occupied by the crystalline phase per unit volume of the material in the hypothetical case of unbounded growth. From the space filling the actual number of crystallites is calculated as

$$N_c(t) = \int_{-\infty}^{t} \alpha(s)\,[1 - \xi_g(s)]\, ds \,. \tag{2.57}$$

Stepwise differentiation of the integral in equation 2.56 with respect to time results in a set of coupled differential equations describing, in the case of spherulitic growth, the evolution of the unbounded number N, total radius R_{tot}, total surface area S_{tot}, and total volume V_{tot} of spherulites per unit volume. These rate equations, derived by Schneider *et al.* [98], read

$$\dot{\phi}_3(t) = 8\pi\alpha(t) \quad (\phi_3 = 8\pi N)\,; \tag{2.58}$$

$$\dot{\phi}_2(t) = G(t)\phi_3(t) \quad (\phi_2 = 4\pi R_{tot})\,; \tag{2.59}$$

$$\dot{\phi}_1(t) = G(t)\phi_2(t) \quad (\phi_1 = S_{tot})\,; \tag{2.60}$$

$$\dot{\phi}_0(t) = G(t)\phi_1(t) \quad (\phi_0 = V_{tot})\,. \tag{2.61}$$

The advantage of a differential formulation is that it is easily incorporated in the framework of thermodynamics, where the governing equations are also

in a differential form. For anisotropic crystal growth processes, Schneider's model should be modified by starting with equation 2.53 instead of equation 2.52. Hütter *et al.* [53] mainly focused on the special cases where all nonzero growth rates are equal. They studied the effects of changes in the preferred crystal shapes and in the directions of growth on the overall kinetics. In the model of shish-kebab formation developed by Liedauer *et al.* [73], which will be discussed in the next section, longitudinal and radial growth occur simultaneously and proceed at different rates.

The differential model of crystalline structure formation in quiescent conditions is completed by a description of impingement of the growing crystallites. Avrami's model, which was derived for the case of spatially random nucleation [6] is expressed as

$$\phi_0(t) = -\ln\left[1 - \xi_g(t)\right] \tag{2.62}$$

and corresponds to equation 2.56 when used in combination with Schneider's rate equations. The actual number of crystallites is again given by equation 2.57. Tobin [115, 116] derived a different impingement model. He found

$$\frac{\xi_g(t)}{1 - \xi_g(t)} = c \int_{-\infty}^{t} \alpha(s)\, V(t,s) \left[1 - \xi_g(s)\right] ds \tag{2.63}$$

for the space filling. The implementation of this model in a differential formulation is not straightforward since, due to the factor $(1 - \xi_g)$ appearing in the integrand, the right-hand side of equation 2.63 is not equivalent to ϕ_0. Therefore, using instead of equation 2.62 the expression

$$\phi_0(t) = \frac{\xi_g(t)}{1 - \xi_g(t)} \tag{2.64}$$

in combination with Schneider's rate equations is not equivalent to the integral formulation given in equation 2.63. Nevertheless, Tobin's model is usually implemented this way. Since it was obtained by a more phenomenological approach than the Kolmogorov–Avrami model, which can be derived from a formal stochastic treatment of the nucleation phenomenon, there is no fundamental objection to this apparent misuse of Tobin's model. Better results may even be obtained in certain cases [131] than with the Avrami model.

The modeling of crystallization processes, outlined above, is easily extended to multiphase systems, consisting of an amorphous melt and multiple growing crystalline and/or mesomorphic phases. See for example Brucato *et al.* [16] and Coccorullo *et al.* [21].

2.4 Flow-induced crystallization

2.4.1 Structure development during and after flow

The crystallization of polymers is significantly influenced by flow. Two effects are observed in experiments. Even in relatively weak flows the nucleation rate, and as a result the nucleation density, is significantly enhanced [4, 57, 119]. Secondly, under sufficiently strong flow conditions, the crystalline morphology changes. Row crystallites and shish-kebabs have been identified in various experiments [4,31,52,57,105,106]. A row crystallite consists of a number of adjoining spherulites, aligned in the flow direction. A shish-kebab is observed as a fibrillar nucleus (the shish) with chain-folded lamellae (kebabs) growing outward from its surface. These oriented morphologies are here assumed to originate from the same initial fibrillar structure. The only difference, presumably, lies in the lateral growth processes.

It is generally believed that orientation and stretch of macromolecules lower the free energy barrier associated with the formation of a stable nucleus. Attempts have been made to incorporate this deformation and temperature-dependent process in a continuum mechanics framework. Ziabicki's general theory of nucleation kinetics provides a means to account for the influence of the orientation distribution of macromolecular chains in the amorphous phase on the free energy barrier associated with incorporating these chains in the crystalline phase [129]. The theory was used to establish a coupling between the nucleation rate and macroscopic flow conditions [130]. Similar in approach is a recent paper in which Coppola *et al.* [22] took the nucleation rate from the theory of Lauritzen and Hoffman [51,68], which is driven by the free energy difference between the amorphous phase and the crystalline phase, and modified it by incorporating the free energy change caused by chain orientation according to the Doi– Edwards model [27]. They successfully predicted the decrease of the induction time of shear-induced crystallization with increasing shear rate.

The first successful attempt to capture the creation and development of the shish-kebab morphology in a theoretical framework was made by Liedauer *et al.* [73]. They adapted Schneider's rate equations to describe fibrillar nuclei growing in the longitudinal and radial directions. The resulting set of coupled differential equations reads, in a slightly different notation,

$$\dot{\psi}_3(t) + \frac{\psi_3(t)}{\tau_n} = 8\pi I_n(t) \quad (\psi_3 = 8\pi N_{ori}); \tag{2.65}$$

$$\dot{\psi}_2(t) + \frac{\psi_2(t)}{\tau_l} = I_l(t)\,\psi_3(t) \quad (\psi_2 = 4\pi L_{tot}); \tag{2.66}$$

$$\dot{\psi}_1(t) = G(t)\psi_2(t) \quad (\psi_1 = S_{tot}); \tag{2.67}$$
$$\dot{\psi}_0(t) = G(t)\psi_1(t) \quad (\psi_0 = V_{tot}). \tag{2.68}$$

The functions I_n and I_l are the driving forces for nucleation and longitudinal growth. The number and length of oriented nuclei are subject to relaxation processes characterized by τ_n and τ_l, respectively. In the original model, both driving forces were chosen proportional to the square of the shear rate,

$$I_n(t) = g_n \left[\frac{\dot{\gamma}(t)}{\dot{\gamma}_n}\right]^2 \tag{2.69}$$

and

$$I_l(t) = g_l \left[\frac{\dot{\gamma}(t)}{\dot{\gamma}_l}\right]^2, \tag{2.70}$$

where the shear rate is again defined as $\dot{\gamma} = \sqrt{2\boldsymbol{D} : \boldsymbol{D}}$, $\dot{\gamma}_n$ and $\dot{\gamma}_l$ are characteristic shear rates for the flow-induced nucleation and growth processes, and g_n and g_l are temperature-dependent scaling parameters.

Zuidema *et al.* [131,132] adapted this model, preserving its basic structure but assuming I_n and I_l proportional to the second invariant of the deviatoric part of the elastic Finger tensor,

$$I_n(t) = g_n J_2\left(\boldsymbol{B}_e^d(t)\right) \tag{2.71}$$

and

$$I_l(t) = g_l J_2\left(\boldsymbol{B}_e^d(t)\right). \tag{2.72}$$

Notice that $\boldsymbol{B}_e^d$ contains the stretch and the deviatoric part of the orientation tensor: $\boldsymbol{B}_e^d = 3\Lambda^2\boldsymbol{S}^d$. Zuidema *et al.* justified their assumptions by plotting the number of shishes ψ_3 calculated at the experimentally determined boundaries between morphological layers [61] against the shear time, using either of the three highest modes of the relaxation spectrum. Their results showed a linear trend except when the mode with the longest relaxation time was used, in which case ψ_3 was independent of the shear time. Therefore, only this mode was used thereafter in equations 2.71 and 2.72. The shear time independence was observed at the boundary between the core and the fine-grained layer as well as the boundary between the fine-grained layer and the oriented skin in the injection-molded samples. In contrast to the model of Liedauer *et al*, the kinetics of nucleation and growth are enhanced not only during flow, but also after cessation of flow, as long as the viscoelastic stress has not fully relaxed.

An important characteristic of the nucleation model expressed in equation 2.65 is that a nucleus is allowed to disappear, a process governed by

the relaxation time τ_n, before a shish can grow out of it. Liedauer *et al.* suggested taking $\tau_n \to \infty$ because nuclei only contribute to space filling once they become stable and start to grow, and as of that moment they cannot disappear anymore. However, it is widely accepted that the nucleation rate is determined by two opposing forces: the macroscopic flow, orienting and stretching the molecules in the melt, and the relaxation processes associated with molecular orientation and stretch. One would expect from this point of view that unstable nuclei can dissolve and that the relative time scales of macroscopic flow and molecular relaxation processes, which are strongly dependent on temperature, determine the rate at which stable nuclei appear [123]. So it seems reasonable to make a distinction between stable and unstable nuclei. This was done neither by Liedauer *et al.* in their original paper [73] and subsequent publications from the same group [14, 29, 31], nor by Zuidema *et al.* [131, 132]. In the latter authors' numerical simulations of injection molding, a process in which the material is cooled very fast, the assumption of an infinite relaxation time for the nuclei was appropriate. However, when isothermal crystallization after a short-term deformation is considered, as is the case in the majority of experiments reported in the literature, one might question the validity of this assumption. In chapter 3, where we simulate crystallization induced by short-term shear flow, it will become clear that it is indeed necessary to assume that nuclei can dissolve. But when the driving force I_n vanishes, the nuclei that have already started growing into crystallites should not be predicted to dissolve. Therefore, we distinguish between stable and unstable nuclei. In the remainder of this thesis, *the term nuclei will be used to designate stable nuclei exclusively. Unstable nuclei shall henceforth be called precursors.*

Thus, the first step in the development of crystalline structure is the creation of precursors. The second step is the transformation of precursors into nuclei. The equations governing these processes, to be derived in the next section, will replace the single equation 2.58 for point nuclei or 2.65 for fibrillar nuclei. The evolution of the unbounded size, surface, and volume of spherulites and oriented crystallites is still given by equations 2.59 to 2.61 and 2.66 to 2.68, respectively. Impingement is taken into account by summation of their unbounded volume fractions. Using Avrami's model,

$$\phi_0(t) + \psi_0(t) = -\ln\left[1 - \xi_g(t)\right] . \tag{2.73}$$

The actual numbers of spherulites and oriented crystallites follow from equation 2.57 when α is replaced by $\dot{\phi}_3/(8\pi)$ or $\dot{\psi}_3/(8\pi)$, respectively.

2.4.2 Flow-induced point nucleation

A brief return to the basic derivation of Avrami's theory of nucleation serves as the point of departure for a description of flow-induced nucleation. First a distinction is made between homogeneous precursors, consisting of the polymer's own molecules, and heterogeneous precursors, which include impurities such as nucleating agents, catalyst residues, and cavities. It is assumed that some precursors are present at the start of the crystallization process, their number per unit volume being predetermined by (1) the synthesis of the original material where, either on purpose or coincidentally, heterogeneous precursors may have been added and (2) the thermomechanical history of the material, as a result of which precursors, in general mainly of the homogeneous kind, may have been created that are still present. According to Avrami [5], who did not consider creation of new precursors, this initial number diminishes in two ways in quiescent conditions. First of all, some precursors are transformed into nuclei; in terms of Lauritzen and Hoffman's theory of polymer crystallization [51, 68] they reach the critical size required for the growth of folded-chain lamellae to be stable. Secondly, some are lost as a result of the growth of the crystalline phase at the expense of the amorphous phase. In Avrami's analysis, this 'swallowing' effect was intentionally ignored at first, considering the imaginary case of unbounded growth. Precursors are then also nucleated and, in the theory discussed next, created inside the already formed crystalline phase. Moreover, impingement of crystallites is ignored, so that they grow through each other without any obstruction. The error thus made was corrected for afterwards in the analysis leading to equation 2.62 for the space filling [6]. The following discussion concerns the unbounded numbers of precursors and nuclei. Application of equation 2.57 will result in the actual number of crystallites.

Avrami's theory is extended to include the creation of new homogeneous precursors. Furthermore, precursors will be allowed to dissolve into the melt. The form of equation 2.65, describing the nucleation process in the rate equations of Liedauer *et al.* [73], is adopted to capture these processes. A homogeneous precursor is envisaged as a cluster or bundle of chain segments, belonging to one or more macromolecules, in some ordered state. The question what exactly this state is, though interesting, is beyond the scope of this work. Homogeneous precursors are created by two fundamentally different processes. The first is a thermal process, which means that chain segments sporadically form precursors as a result of random order fluctuations, occurring in the melt at a frequency that depends on temperature and, if a flow is applied, on the molecular orientation and stretch. The second process is athermal creation of precursors. The concept of athermal nucleation,

as introduced by Fisher *et al.* [33], implies that precursors are transformed into nuclei when, upon reaching a characteristic temperature, the critical size required to overcome the energy barrier for nucleation becomes equal to their actual size. The nuclei thus obtained are called athermal nuclei. Here, *athermal precursors* are defined as precursors that appear upon lowering the temperature. They originate from entities with a certain degree of order, which are intrinsically present in the melt. This definition may appear strange; why not label all these entities precursors? The answer is that only part of them are large enough to be nucleated at a given temperature. If we keep the material at that temperature for a sufficiently long time, eventually they will become nuclei. But the ones that are too small will never become nuclei, no matter how long we wait. Upon cooling, more of these ordered entities become available for nucleation; they become precursors. Whether they are actually nucleated depends on the nucleation rate and the rate of dissolution of precursors.

Things will become more clear when we look at the mathematical formulation of the balance between these processes of creation and disappearance. The number of homogeneous precursors per unit volume N_p^{hom} is given by the differential equation

$$\dot{N}_p^{hom}(t) = I_{pq}(t) + I_{pf}(t) + \dot{T}(t)\frac{\partial N_{pa}^{hom}}{\partial T} - \frac{N_p^{hom}(t)}{\tau_p(t)}, \tag{2.74}$$

where I_{pq} is the driving force behind the thermal creation of homogeneous precursors in a quiescent melt and I_{pf} is an additional flow-induced driving force, related to one or more modes of the viscoelastic constitutive model. This relation will be dealt with separately in the next section and in chapter 3. The third term on the right-hand side of equation 2.74 is the rate of creation of athermal homogeneous precursors. The last term represents the rate of depletion of available homogeneous precursors; $1/\tau_p$ is a measure of the probability that one of them disappears. This parameter is composed of two terms, related to the mechanisms of disappearance, i.e. dissolution into the melt and nucleation:

$$\frac{1}{\tau_p} = \underbrace{\frac{1}{\tau_{pd}}}_{\text{dissolution}} + \underbrace{\frac{1}{\tau_{pn}}}_{\text{nucleation}}. \tag{2.75}$$

From this expression τ_p, which may be thought of as a mean residence time of homogeneous precursors, is obtained as

$$\tau_p = \frac{\tau_{pd}\tau_{pn}}{\tau_{pd} + \tau_{pn}}. \tag{2.76}$$

The characteristic time of nucleation was already present in Avrami's theory [5]. The characteristic time of dissolution is conceptually similar to the 'relaxation time' of nuclei encountered in publications by the group of Eder and Janeschitz-Kriegl [29,31,73] and by Zuidema *et al.* [131,132]. However, since the dissolution process is associated with precursors instead of nuclei in the present theory, a finite value can be assigned to τ_{pd} while still avoiding the unrealistic result that nuclei, which are by definition stable, gradually disappear when the driving forces I_{pq} and I_{pf} vanish. Both characteristic times may depend on flow conditions and temperature. It is expected that τ_{pd} and τ_{pn} are related to one or more relaxation processes associated with orientation or stretch of chain segments.

The number of homogeneous nuclei appearing in a given time interval is matched by the number of homogeneous precursors disappearing as a result of nucleation in that time interval. For the homogeneous nucleation rate one then finds

$$\dot{N}_n^{hom}(t) = \frac{N_p^{hom}(t)}{\tau_{pn}(t)} . \tag{2.77}$$

It is evident from equation 2.77 that the homogeneous nucleation rate goes to infinity when $\tau_{pn} \to 0$. In a numerical simulation, the number of nuclei created during a time step then becomes infinite. This violates the species balance, which dictates that the number of newly created nuclei cannot exceed the number of available precursors. Nevertheless, such fast nucleation processes are encountered in practice (see for example chapter 3). So the model has to be reformulated for small τ_{pn}. Because all homogeneous precursors become nuclei at the very moment they appear, the distinction between the two species vanishes. Thus, we may discard the evolution equation for the number of homogeneous precursors, 2.74, and replace equation 2.77 by

$$\dot{N}_n^{hom}(t) = I_{pq}(t) + I_{pf}(t) + \dot{T}\frac{\partial N_{pa}^{hom}}{\partial T} . \tag{2.78}$$

This result can be derived analytically from equations 2.74 and 2.76. The details of this derivation are included in appendix B. Athermal nucleation, according to the formal definition of Fisher *et al.* [33], is obtained when $I_{pq} = I_{pf} = 0$ in addition to $\tau_{pn} = 0$.

It is assumed that the number of foreign entities available to become heterogeneous precursors is constant. Although, for example, cavities may develop in the material as a result of thermomechanical loading and serve as heterogeneous precursors, the vast majority of these entities will in general consist of chemical impurities, which may have been added on purpose (such as nucleating agents). Their number in the uncrystallized melt was

established during the synthesis of the material. Impurities are often of a nonpolymeric nature. As a result, they cannot dissolve ($\tau_{pd} \rightarrow \infty$). In the present context, we consider something dissolved if it has been decomposed into elements that behave like the disordered polymer molecules in the amorphous phase. These elements cannot act as a precursor, even upon lowering the temperature, unless they are assembled in an ordered structure again. It is assumed that any nonpolymeric heterogeneity will be able to become a precursor at some activation temperature. Polymeric additives are left out of consideration here.

The only way for the impurities to become precursors is therefore through an athermal process, and the resulting heterogeneous precursors can only disappear by becoming nuclei. Hence

$$\dot{N}_p^{het}(t) = \dot{T}\frac{\partial N_{pa}^{het}(t)}{\partial T} - \frac{N_p^{het}(t)}{\tau_{pn}^{het}(t)} . \tag{2.79}$$

The heterogeneous nucleation rate is given by

$$\dot{N}_n^{het}(t) = \frac{N_p^{het}(t)}{\tau_{pn}^{het}(t)} . \tag{2.80}$$

Finally, one additional assumption with respect to heterogeneous precursors will be made here, namely that they are not subject to any thermal fluctuations in size, which cause thermal nucleation. Then equation 2.80 is transformed into

$$\dot{N}_n^{het}(t) = \dot{T}\frac{\partial N_{pa}^{het}(t)}{\partial T} . \tag{2.81}$$

This result can be derived in the same way as equation 2.78, as explained in appendix B, if we take $\tau_{pn}^{het} = 0$. In other words, heterogeneous precursors and heterogeneous nuclei are assumed equivalent. Every ordered entity that is large enough to be nucleated at a given temperature will be nucleated as soon as that temperature is reached.

Eder *et al.* [28] proposed a simple, and therefore attractive, model for the athermal nucleation of heterogeneous precursors. They used a discrete set of nucleation times $\tau_{pn,j}^{het}$ for different species of heterogeneous precursors $N_{p,j}^{het}$ and assumed that each species would instantaneously become stable when its characteristic temperature T_j was reached:

$$\tau_{pn,j}^{het}(T) = \begin{cases} \infty & \text{for} \quad T > T_j ; \\ 0 & \text{for} \quad T \leq T_j . \end{cases} \tag{2.82}$$

Equation 2.81 is then to be replaced by

$$\dot{N}_n^{het}(T(t)) = \sum_j N_{p,j}^{het}(0)\,\delta(T(t) - T_j) , \tag{2.83}$$

where $t = 0$ corresponds to the onset of undercooling. Care should be taken when implementing the above method in numerical simulations. Equation 2.83 predicts that, upon heating, the athermal nuclei are instantaneously lost, i.e. the folded-chain crystal structure melts, and the underlying precursors reappear as soon as T_j is reached. This is not observed in experiments. In fact, in the 'inverse quenching' experiments of Acierno and Grizzutti [2], where the crystallizing melt was heated fast to a suitably chosen temperature below the melting point, the nuclei obtained at lower temperature were shown to remain stable for a substantial period of time. Fortunately, since in most industrial manufacturing processes no heating occurs, melting of nuclei can usually be left out of consideration altogether.

2.4.3 Modeling flow-induced creation of precursors

The driving forces behind the creation of homogeneous precursors, I_{pq} as found in a quiescent melt and the flow-induced driving force I_{pf}, have not been specified yet. At practical degrees of undercooling, the contribution of I_{pq} to the final number of crystallites is negligible in comparison to the number of crystallites grown from athermal nuclei in quiescent conditions. On the other hand, the strong influences of strength and duration of flow on the nucleation density seem to indicate that the flow-induced sporadic creation process, characterized by I_{pf}, cannot be disregarded. In fact, nearly all flow-induced crystallization theories that have been proposed over the years are based on the assumption that flow induces sporadic creation of homogeneous precursors. Differences lie in the presumed nature of these precursors and the physics behind the creation process. For example, spinodal decomposition of the melt into two phases of different density has been suggested, with the denser phase being rich in closely packed helical sequences that serve as precursors [45, 46, 84, 97, 113]. On the other hand, transient liquid crystalline phases have been observed during flow-induced crystallization and were proposed as intermediate states in the transition from the amorphous to the semicrystalline phase [69–71].

The basic concept of the different physical pictures is that flow promotes the creation of precursors by orienting and/or stretching the macromolecular chains in the melt. In the following, the model developed by Zuidema *et al.* [131, 132] will be taken as a starting point, since it is quite general in the sense that no detailed assumptions of the internal structure of precursors are made. On the other hand, because the kinetics of creation and growth are related to molecular orientation and stretch, there is a clear link between macroscopic structure formation and processes occurring at the molecular scale. Finally, a unique new view on flow-induced nucleation, based on an

athermal instead of a thermal creation process, will be discussed.

Enhanced thermal creation process

According to the model proposed by Zuidema *et al*, flow increases the frequency of thermal order fluctuations having a sufficiently high amplitude to serve as nuclei. Therefore, the second invariant of the deviatoric part of the elastic Finger tensor was chosen as the driving force behind nucleation, as seen in equation 2.71. The flow-induced nuclei, as effective crosslinks, were assumed to increase the longest relaxation time of the melt according to the simple linear relationship

$$\lambda(t) = \lambda_0 \left[1 + aN_{nf}(t)\right] , \tag{2.84}$$

where λ_0 is the relaxation time of the amorphous phase, N_{nf} is the number of flow-induced nuclei and a is a scaling parameter, characteristic of the material and the processing conditions. Since the relaxation time determines the evolution of the elastic Finger tensor, which in turn determines the flow-induced nucleation rate, equation 2.84 makes flow-induced nucleation a self-enhancing process. As a result, structure formation in injection molding processes could be simulated quite successfully [131, 132].

The Zuidema model will be formulated in a different way here, due to the treatment of the crystallizing melt as a multiphase system. We assume that nuclei, and the crystallites that grow from them, only influence the effective properties (moduli and relaxation times) of the material as a whole. This should be accounted for by the chosen suspension model. The matrix formed by the amorphous phase, however, is where precursors are created. Therefore, I_{pf} is chosen proportional to the deviatoric part of the elastic Finger tensor,

$$I_{pf}(t) = g_p J_2\left(\boldsymbol{B}_e^d(t)\right) , \tag{2.85}$$

or some other function of the average viscoelastic stress in the material. Another possible choice is to use a function of the average viscoelastic stress resulting from the disturbed velocity field, which is characterized by $f_2\boldsymbol{D}$ as explained in section 2.2.4, but using the modulus of the amorphous phase G instead of the effective modulus $f_1 G$. Perhaps this will give a closer relation to the state of deformation in the amorphous phase, where precursor formation takes place.

Following the train of thoughts that lead to equation 2.84, the relaxation time of the amorphous phase may be related to the number of flow-induced precursors N_{pf} according to

$$\lambda(t) = \lambda_0 \left[1 + aN_{pf}(t)\right] . \tag{2.86}$$

Perceptive readers may object that this approach fails in the case of fast nucleation processes, described by equations 2.78 and 2.81, because then there are no precursors, only nuclei. In section 3.3.2, we will see that the method proposed here is useful after all. The reason is that, based on experimental observations, the assumption must be made that nucleation is inhibited by flow. It is only after cessation of flow that the majority of precursors become nuclei. Another point of criticism might be that nuclei, which are stable but whose size is still of the order of molecular dimensions or smaller, also act as physical crosslinks. Arguably, it would be more realistic to relate the relaxation time to the combined number of precursors and these small nuclei, while taking nuclei beyond a certain size into account as particles in the suspension model. But then the size distribution of nuclei would have to be known. Here, we simply assume that a precursor is removed from the amorphous phase once it becomes a nucleus and that, at the same instant, this nucleus starts to act as a particle instead of a physical crosslink.

Whereas Zuidema *et al.* successfully used the constitutive model of Leonov, which is based entirely on linear viscoelastic data, it is interesting to look at the more advanced Pom-Pom models. As explained in section 2.1.2, the parameter q appearing in these models is a measure of the amount of branching. Therefore, again using the concept of precursors as physical crosslinks, we propose that q is a function of the number of flow-induced precursors. In the original Pom-Pom model of McLeish and Larson [77], both relaxation times are proportional to q. Modifying this parameter according to an expression similar to equation 2.86,

$$q(t) = q_0 \left[1 + aN_{pf}(t)\right] , \tag{2.87}$$

then yields

$$\lambda_b(t) = \lambda_{0b} \left[1 + aN_{pf}(t)\right] \tag{2.88}$$

and

$$\lambda_s(t) = \lambda_{0s} \left[1 + aN_{pf}(t)\right] \tag{2.89}$$

for the orientation relaxation time and the stretch relaxation time of the backbone, respectively. In the extended Pom-Pom model of Verbeeten *et al.* [125,126] however, the latter is related to the molecular stretch parameter Λ by an exponential function, according to equation 2.15. Equation 2.89 should therefore be replaced by

$$\lambda_s(t) = \lambda_{0s} \left[1 + aN_{pf}(t)\right] \exp\left[-\frac{\nu\left(\Lambda(t) - 1\right)}{1 + aN_{pf}(t)}\right] \tag{2.90}$$

when the XPP model is used.

Enhanced athermal creation process

Over the course of the last decade, Janeschitz-Kriegl and coworkers [55–59, 108] have developed an interesting new, fundamentally different view on flow-induced nucleation. Their original goal, however, was to explain the observation made in quiescent experiments that, even in polymers containing few heterogeneous precursors, the nucleation density increases exponentially by many decades as a function of the crystallization temperature. Quiescent homogeneous nucleation has traditionally been described as a sporadic process, characterized by a finite nonzero free enthalpy barrier or, in the present context, a finite nonzero value of τ_{pn}^{hom}. But this picture is not correct at high degrees of undercooling. The mentioned barrier, following the classical nucleation theory, decreases upon cooling and becomes negligible at a temperature T_u. Thus, only in the temperature range $T_u < T < T_m$ a sporadic, fluctuation-controlled nucleation process can exist. According to what is known as Ostwald's rule of stages, the transition from the amorphous phase to the semicrystalline phase then proceeds through a number of intermediate, metastable states of increasing stability. Janeschitz-Kriegl [55] estimated the upper limit of this range of metastable undercooling as

$$T_m - T_u < \frac{1}{3}\frac{\Delta H_f}{C_{p,m}}, \tag{2.91}$$

where $C_{p,m}$ is the heat capacity of the melt at the equilibrium melting temperature T_m and ΔH_f is a heat of fusion, the exact meaning of which will be clarified shortly. Upon cooling to T_u all homogeneous precursors immediately become stable, so that none are left for nucleation at lower temperatures. But this does not agree with the aforementioned exponential increase of the number of crystallites with increasing degree of undercooling, which is observed below T_u as well as above, even in very pure polymer samples.

In subsequent papers by Janeschitz-Kriegl *et al.* [56,58] the idea of athermal nucleation of homogeneous precursors, intrinsically present in the melt, was developed in an attempt to solve this problem. These effectively pointlike precursors were envisaged as short bundles of parallel helical chain segments. According to the ideas of Strobl [109] the rate of lateral attachment of new segments, leading to the growth of a lamella, is determined by a 'surface tension' σ_e at the tips of the bundle, which is created by the difference in packing density between the chains' helical parts and their coiled ends protruding into the melt. This surface tension is not constant, but builds up as more helical stems are added and eventually levels off (see figure 2 of [58]). The lamellar growth process will proceed at a critical value of the number of repeating units n along the axes of the helices, i.e. in the longitudinal

direction of the bundle,

$$n^*(T) = -\frac{2\sigma_e T_m}{\Delta H_f (T_m - T)}, \tag{2.92}$$

where ΔH_f is defined as the heat of fusion per repeating unit. Because n will generally be large, the effect of σ_e on ΔH_f may be neglected. Hence, ΔH_f represents the heat of fusion of an ideal bundle of packed helical chains, where only a free enthalpy barrier associated with the process of lateral attachment itself has to be overcome. It is this barrier that vanishes at $T = T_u$. The lateral growth rate then initially increases, but is impeded by the buildup of σ_e. Only long enough precursors ($n \geq n^*$) can overcome this new barrier and grow into lamellae.

Janeschitz-Kriegl *et al.* [57, 58, 108] further proposed that flow allows the intrinsic homogeneous precursors to grow longer, as a result of which they will attain the critical size n^* at higher temperatures than in quiescent conditions. It was argued that precursors with lower activation temperatures, having a less ordered structure, will be more easily created and hence be more numerous in the melt than precursors with higher activation temperatures. Therefore, increasing the strength or the duration of flow will have a nonlinear effect on the number of nuclei tapped from the reservoir of precursors whose activation temperatures were initially below the actual crystallization temperature.

In a quiescent melt, the implementation of this athermal nucleation model is straightforward. The number of athermal precursors as a function of temperature, which is derived from the number of crystallites obtained in quiescent crystallization experiments, can be used as input. Because no threadlike precursors develop in the absence of any flow history, homogeneous and heterogeneous precursors do not have to be considered separately. Either the combined $\dot{T}\partial N_{pa}/\partial T$ terms in equations 2.74 and 2.79, or a discrete set of precursor species, to be used in equations 2.82 and 2.83, are determined by the experiments. In the latter case, one or more species should be taken to represent the sporadic nucleation process (the corresponding $\tau_{pn,j}$ having a finite value in the temperature range $T_u < T < T_m$).

If the melt possesses a flow history, it is necessary to know which part of the initially available precursors are homogeneous. Only these can grow and shift their activation temperatures by the mechanism described above. Subtracting the concentration of nucleating agents, which would have to be supplied by the manufacturer, from the total number of athermal precursors as a function of temperature in quiescent conditions, a fairly accurate estimate of the number of homogeneous athermal precursors might be made. The activation temperature of nucleating agents may be chosen close to the

melting temperature. A longitudinal growth model is needed in order to determine which fraction of the total amount of homogeneous precursors are long enough to be nucleated at any time during the crystallization process.

Thermal and athermal processes in flow-induced crystallization

In the Zuidema model, which was slightly modified here, it is assumed that flow enhances thermal creation of precursors. The driving force I_{pf} is related to the recoverable strain, which reflects the combined molecular orientation and stretch. Furthermore, a correlation between the orientation and stretch relaxation times is assumed. The model leaves some room for theorizing the details of the underlying physics, while still capturing the essentials. The Janeschitz-Kriegl model defies the traditional view of flow-induced nucleation as a sporadic process. Instead, it assumes that a range of homogeneous precursor species already exist in the material above the melting temperature and are activated (become nuclei) at specific temperatures. Flow merely perfects these precursors, shifting their activation temperatures upwards. Although these models are fundamentally different, both predict a nonlinear increase of the number of crystallites with increasing work supplied to the material, as observed by Janeschitz-Kriegl *et al.* [57, 58, 108].

Neither of the two models can be discarded yet. It is even conceivable that the different processes that are envisioned both take place in crystallizing polymer melts. The truth may prove difficult to find. But at least a framework for modeling flow-induced nucleation and growth of spherulites, in which sporadic as well as athermal nucleation processes can be incorporated, has been established in section 2.4.2. The kinetics of homogeneous nucleation are determined either by equations 2.74 and 2.77 or by equation 2.78. Analogously, the kinetics of heterogeneous nucleation are determined either by equations 2.79 and 2.80 or by equation 2.81. Substituting

$$\phi_3(t) = 8\pi \left[N_n^{hom}(t) + N_n^{het}(t) \right] \tag{2.93}$$

in Schneider's rate equations and using an impingement model, for example equation 2.62, the crystallization process is fully described. However, the situation becomes more complicated when threadlike precursors develop in the melt, which may lead to oriented crystal structures. A rate-type model of oriented crystallization, similar to equations 2.65–2.68, is needed that includes the creation and growth of precursors and their transformation into either spherulites or oriented crystallites.

2.4.4 Growth of threadlike precursors

Strong flow conditions are known to induce the formation of threadlike precursors (shishes) but the nature of this process and the internal structure of the threadlike precursors are still subjects of debate. It is generally believed, however, that the high molecular weight fraction of a crystallizing polymer melt is of primary importance in the development of oriented semicrystalline morphologies [1, 60, 107, 127, 132]. Here, two recently proposed physical explanations for the creation and growth of threadlike precursors [101, 106] will be discussed and their place within the framework of a unifying approach to flow-induced nucleation and growth kinetics [123] will be indicated.

The streamer model

Seki *et al.* [101] investigated binary iPP/iPP blends where one of the constituents had a relatively high molecular weight with a narrow distribution. The concentration of these long molecules was varied. The authors concluded from birefringence measurements, performed during isothermal crystallization under pressure-driven shear flow, that the long chain content greatly enhanced the formation of threadlike precursors, even while these consisted partly of shorter molecules. Surprisingly, they found that the number of point nuclei was not significantly influenced by the presence of long chains. Seki *et al.* explained the flow-induced development of oriented structures as follows. The formation of a shish starts with a pointlike precursor, to which a long chain is adsorbed. This chain is oriented by the flow, forming a 'streamer' in the wake of the pointlike precursor. The increased orientation of this streamer increases the probability that new pointlike precursors are created, to which new streamers can be adsorbed. Thus a string of connected pointlike precursors constitutes the shish. In a later stage, kebabs grow from this row of pointlike precursors.

The bundle model

Somani *et al.* [106] concluded, on the basis of results from in-situ SAXS measurements performed during shear-induced crystallization of iPP, that the streamer model of Seki *et al.* did not apply to their experiments. This conclusion was based on the observation that no meridional maxima, which would indicate the presence of lamellar stacks oriented perpendicular to the flow direction, showed up in the scattering patterns until after an equatorial streak, related to fibrillar structures aligned in the flow direction, had developed. Therefore, rather than as a string of pointlike precursors, they

visualised a shish as a bundle of parallel chain segments and proposed a longitudinal growth mechanism driven by the increased orientation and stretch of the free chain ends at the tips of the bundle[1]. The meridional maxima appearing in later stages of the crystallization process were attributed to kebabs growing from the shish.

Because of the low degree of crystallinity, estimated from WAXS measurements, it was assumed that the threadlike precursors consisted mainly of mesomorphic structures, and contained only a small fraction of crystalline material. A similar conclusion was drawn by Li and De Jeu [69–71] from SAXS and WAXS experiments after step shear flow. They identified smectic filaments as the building blocks of threadlike precursors.

One might object against Somani *et al.*'s dismissal of the streamer model that a pointlike precursor, consisting of a small number of parallel chain segments, may have been present for some time before a lamella starts to grow from its lateral surface. In that case, the growth process proposed by Seki *et al.* will result in strings of pointlike precursors that pass unnoticed in SAXS until they are nucleated and that, if they develop into fibrillar structures, do so either before or after the moment of nucleation. Thus, the absence of meridional scattering prior to the appearance of equatorial streaks may be caused by delayed nucleation; it does not necessarily mean that no pointlike precursors have been formed yet.

A closer look at the conditions and kinetics of precursor growth

Before comparing experimental results, it is of the utmost importance to verify if the external conditions are similar enough to allow such comparison. Van Meerveld *et al.* [123] therefore set up a classification scheme for flow-induced crystallization experiments. They identified four flow regimes. The transitions between these regimes are characterized by three parameters: the Deborah numbers associated respectively with orientation and stretch of chain segments, $De_b = \dot{\gamma}\lambda_b$ and $De_s = \dot{\gamma}\lambda_s$, and the critical backbone stretch Λ^* at which rotational energy barriers are sufficiently lowered to allow rotational isomerization (RI) of chain segments, implying a departure from Gaussian chain dynamics. Table 2.3 shows the definition of the flow regimes. Regime 1 corresponds to the quiescent state or weak flow conditions, where pointlike precursors are created as a result of fluctuations in the orientation and conformation of chain segments. According to Van Meerveld *et al,* the rate of creation is increased when chain segments are oriented by the flow (regime 2) because, in that case, only a fluctuation in the conformation

[1]Several models have been proposed to describe this kind of growth; see for example Lieberwirth [72].

Table 2.3: Classification of FIC experiments [123].

Flow regime	$De_b = \lambda_b \dot{\gamma}$	$De_s = \lambda_s \dot{\gamma}$	$\Lambda = \sqrt{\frac{1}{3}\mathrm{tr}\boldsymbol{B}_e}$
1	$De_b < 1$	$De_s < 1$	$\Lambda \approx 1$
2	$De_b > 1$	$De_s < 1$	$\Lambda \approx 1$
3	$De_b > 1$	$De_s > 1$	$1 < \Lambda < \Lambda^*$
4	$De_b > 1$	$De_s > 1$	$\Lambda > \Lambda^*$

may suffice to create a precursor. In regime 3, chain segments are stretched and consequently the probability of conformational fluctuations becomes even higher. Finally, regime 4 is characterized by strong RI. Rotational energy barriers vanish, allowing the chains to easily adopt a helical conformation, which is favorable for creating bundles of parallel segments. Threadlike precursors are supposed to develop when chain segments maintain a large stretch, i.e. $\Lambda > \Lambda^*$, for a sufficiently long time.

With this classification scheme in mind, it is conceivable that different growth models, such as those discussed above, are not necessarily mutually exclusive. First of all, they may simply apply to different flow regimes. To enable the identification of these regimes, Van Meerveld *et al.* [123] compiled rheological data for materials used in several flow-induced crystallization experiments. The data for the iPP melt used by Somani *et al.* can be found in their table 1. The orientation and stretch relaxation times, based on the longest chains in the molecular weight distribution, were calculated using the theoretical results [27, 63]

$$\lambda_b = 3\lambda_e Z^3 \left[1 - \frac{1.51}{\sqrt{Z}}\right]^2 \tag{2.94}$$

and

$$\lambda_s = \lambda_e Z^2 \,. \tag{2.95}$$

The equilibration time λ_e determines the stretch relaxation of a tube segment, which is defined as a portion of the backbone tube confined by two neighboring entanglements, and is independent of molecular weight. The parameter Z, on the other hand, represents the average number of entanglements per molecule, which is obviously a function of the molecular weight distribution of the melt. It is generally defined as

$$Z = \frac{M}{M_e} \tag{2.96}$$

with M_e the average molecular weight between entanglements, which is related to the plateau modulus G_N^0. Van Meerveld *et al.* used $M = M_{HMW}$ with M_{HMW} a characteristic weight of the longest molecules in the melt. The equilibration time was derived from the zero-shear viscosity, given by

$$\eta_0 = 0.064\lambda_e \frac{\rho RT}{M_e} \left[\frac{M_w}{M_e}\right]^{3.4} \tag{2.97}$$

and

$$M_e = \frac{4}{5}\frac{\rho RT}{G_N^0} \tag{2.98}$$

according to the constitutive model of Likhtman and McLeish [74]. A slightly different definition of M_e is used in a number of constitutive models, where the value of the prefactor is 1 instead of 4/5. Other material functions, like Z and η_0, are then to be modified accordingly. Thus, care must be taken not to mix up these definitions [67]. The above procedure to determine λ_e was discussed in detail by Van Meerveld [122]. The result of interest here is that De_s lay between 2.3 and 2.4 in the experiments of Somani *et al.* [103,104,106]. This means that the flow conditions corresponded to regime 3 or regime 4. But Λ^* is lacking, so we cannot check if the maximum stretch condition was indeed fulfilled, as expected on the basis of the shish-kebab morphology observed. In fact, as Van Meerveld *et al.* pointed out, the magnitude of Λ^* for temperatures close to and below T_m has not been resolved yet. Unfortunately, insufficient information on the materials and experimental conditions used by Seki *et al.* [101] is available to estimate De_b and De_s. No rheological data of the blends or their components were given by the authors. Moreover, they used an experimental setup in which a pressure-driven duct flow with a prescribed wall shear stress was applied, so the shear rates in the flow cell are unknown.

Another reason for discarding neither the streamer model nor the bundle model, besides the possibility that they apply to different flow regimes, is that both growth processes may be active in the melt at the same time. The flow regimes, defined in a global sense, are then to be replaced by a model describing localized flow-induced creation and longitudinal growth of precursors. In the following, such a model is distilled from the theoretical works [101,106,123] discussed above. Some degree of speculation is unfortunately inevitable because of the already indicated lack of comparable data. Figure 2.2(a) shows an ensemble of two parallel chain segments from different molecules, which is an extremely simplified representation of a pointlike precursor, but it will suffice to elucidate the basic ideas. This picture corresponds to flow regime 1 in table 2.3: the free ends of the molecules are coiled and

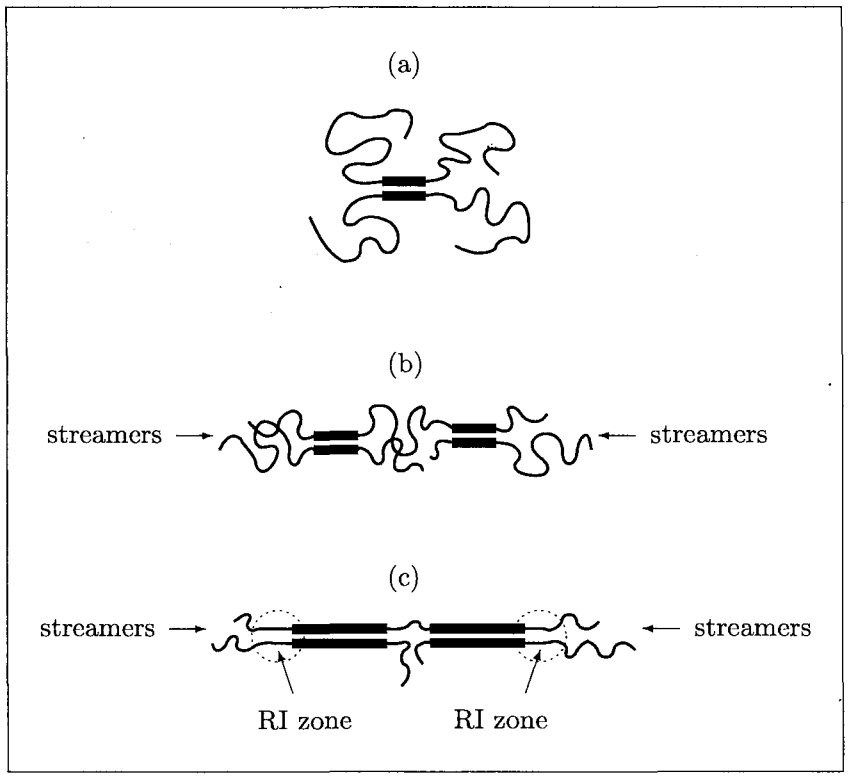

Figure 2.2: Identification of flow regimes at the molecular level. **(a)** No longitudinal growth (regime 1). **(b)** Strings of pointlike precursors induced by orientation (regime 2) and/or stretch (regime 3) of semi-attached chains (streamer model [101]). **(c)** Longitudinal growth of bundles of parallel chain segments [72,106] induced by RI close to the bundle tips (regime 4) and incorporation of new molecules further downstream induced by streamers (regimes 2 and 3).

randomly oriented. Figure 2.2(b) shows what happens when these chains are oriented (regime 2) and/or stretched (regime 3) in the flow direction. Since in general it is not trivial what 'flow direction' exactly means, it is defined here, based on Zuidema's idea that the recoverable strain in the amorphous phase drives the creation and growth of precursors, as the direction of the eigenvector corresponding to the highest eigenvalue of $\boldsymbol{B}_e$ or, equivalently, of $\boldsymbol{B}_e^d$. The increased order in the wake of the original precursor enhances the probability that new pointlike precursors are created. This corresponds to the streamer model, resulting in a row-nucleated or shish-kebab morphology where strings of pointlike precursors form the shishes [101]. Breakup of these strings as a result of the applied macroscopic flow may explain the greater number

of spherulites obtained in comparison to quiescent crystallization. Finally, in figure 2.2(c) the growth process in regime 4, characterized by rotational isomerization of chain segments, is shown. We expect that the condition $\Lambda > \Lambda^*$ is only fulfilled in a region close to the tips of the bundles of parallel chain segments forming the original pointlike precursors. Consequently, due to the locally vanishing rotational energy barriers, the length of these bundles increases. At the same time, however, the oriented and stretched free chain ends form new pointlike precursors, again according to the streamer model, which subsequently grow as a result of RI, etcetera. Thus we obtain a threadlike precursor with an internal structure of alternating bundles of parallel chain segments and regions that are more akin to the amorphous phase, similar to the structure proposed by Somani *et al.* [106].

An essential feature of the proposed explanation of oriented growth is that molecular orientation and stretch are increased locally, i.e. in the vicinity of the tips of precursors. This increase can be accounted for by relating the longest relaxation time of the melt to the number of flow-induced precursors, as explained in the previous section. But the question remains how to incorporate the ideas presented above in a mathematical model of precursor growth. In view of the many uncertainties regarding the nature of threadlike precursors, we take a more phenomenological approach. The basic structure of the growth model of Liedauer *et al.* [73] is probably general enough to capture the relevant processes without the need to specify the inner structure of threadlike precursors. In analogy to equation 2.66, the length of a precursor is given by

$$\dot{L}_p(t) = I_l(t) - \frac{L_p(t)}{\tau_l(t)}. \tag{2.99}$$

For compatibility with equation 2.65-2.68, L_p must be defined as the contour length from the center of a precursor to one of its tips, i.e. half its end-to-end contour length. The growth process is promoted by locally enhanced orientation and stretch of molecules, which is expressed in the driving force I_l, while τ_l is a relaxation time associated with disengagement of molecules from the tips of the precursor. Only homogeneous precursors are assumed to grow in this manner, because they consist of macromolecular chains, which can be oriented and stretched. Nogales *et al.* [81] presented evidence for a flow-induced oriented structure induced by a network-forming nucleating agent, but this will be left out of consideration here. In the following, we restrict our attention to homogeneous precursors and nuclei, and these are simply denoted by N_p and N_n for convenience (instead of N_p^{hom} and N_n^{hom}).

The total length of precursors L_p^{tot} changes according to the balance between the processes of growth and disappearance. The latter includes dis-

solution and nucleation. The characteristic time of nucleation τ_{pn} may be assumed independent of L_p. According to the ideas of Janeschitz-Kriegl [58], discussed in the previous section, the length of a precursor only determines whether or not it can induce the growth of a lamella at a certain temperature. A precursor above a certain length will be able to become a nucleus, but the average amount of time that passes before this actually happens, i.e. τ_{pn}, depends on the thickness of the precursor. On the other hand, the probability that a precursor dissolves is expected to decrease, hence τ_{pd} is expected to increase, as a function of the precursor's length L_p. So unless dissolution is negligible relative to nucleation, in which case $\tau_{pd} >> \tau_{pn}$ and consequently $\tau_p \approx \tau_{pn}$ as seen in equation 2.76, one is forced to introduce a discrete number of 'classes' of precursors, characterized by a number $N_{p,k}$, an average length $L_{p,k}$, a nucleation time $\tau_{pn,k}(L_{p,k})$, and a dissolution time $\tau_{pd,k}(L_{p,k})$. For each class, $\dot{N}_{p,k}$ is determined by nucleation and dissolution, as well as migration of precursors to and from other classes. The details of such an approach are discussed in appendix C.

Here, as an illustrative example, we assume that $\tau_{pd} \to \infty$. Therefore, it is not necessary to keep track of the length distribution. Because $\tau_p = \tau_{pn}$ is the same for all precursors, regardless of their lengths, the rate of change of L_p^{tot} can be written as

$$\begin{aligned} \dot{L}_p^{tot}(t) &= N_p(t)\,\dot{L}_p(t) - \frac{N_p(t)}{\tau_{pn}}\langle L_p(t)\rangle \\ &= N_p(t)\,\dot{L}_p(t) - \frac{L_p^{tot}(t)}{\tau_{pn}(t)}, \end{aligned} \tag{2.100}$$

where the average length

$$\langle L_p(t)\rangle = \frac{L_p^{tot}(t)}{N_p(t)} \tag{2.101}$$

was used. The first term on the right-hand side of equation 2.100 is what $\dot{L}_p^{tot}$ would be if none of the precursors became nuclei. The second term accounts for the total length lost as a result of nucleation. The total length of precursors is obtained by integrating equation 2.100 and reads

$$L_p^{tot}(t) = \int_{-\infty}^{t} \dot{N}_p(s) \int_s^t \dot{L}_p(u)\,du\,ds - \int_{-\infty}^{t} \frac{L_p^{tot}(s)}{\tau_{pn}(s)}\,ds\,. \tag{2.102}$$

The first term on the right-hand side is the result commonly encountered in literature [14, 29, 31, 73], which corresponds to the assumption that all precursors immediately become nuclei ($\tau_{pn} = 0$).

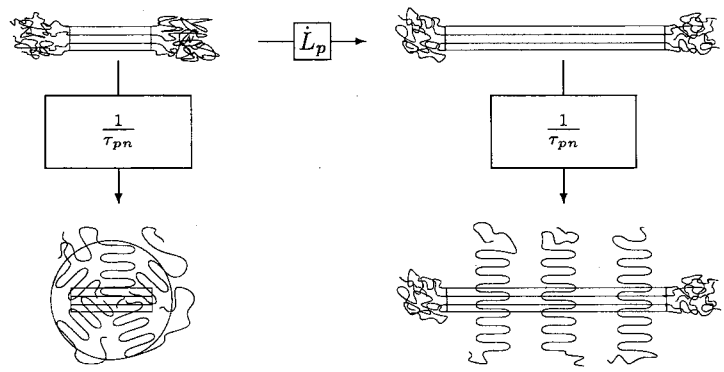

Figure 2.3: Transition from point nuclei to oriented nuclei.

The correlation between the growth of threadlike precursors and the development of an oriented semicrystalline structure is not trivial. While the transformation of pointlike precursors into threadlike precursors is kinetically determined, the transition from a spherulitical to an oriented morphology also depends on the time available for precursors to grow before they are nucleated. A short fibrillar nucleus will easily be overgrown by folded-chain lamellae and develop into a spherulite, and can therefore essentially be considered a point nucleus, while a long fibrillar nucleus will most likely template the growth of a row crystallite or a shish-kebab. Figure 2.3 illustrates this idea.

Janeschitz-Kriegl [58] reported that spherulites, which were accidentally cut exactly through their centers, when observed under the microscope indeed displayed lamellae growing from an oblong particle at the core. In this way, the temporary birefringence observed in the early stages of spherulitic crystallization could be explained. The initial lamellae, growing laterally from the threadlike precursors, cause this effect. Later, lamellae start to grow in all directions and the birefringence vanishes. Hütter *et al.* [53] provided a possibility to describe these kinds of processes with changing directions of growth.

To designate the transition from spherulitical to oriented crystallization, a critical length L_p^* is introduced. Precursors with a length below L_p^* are considered pointlike, while precursors whose length exceeds L_p^* are considered threadlike. When nucleated, these precursors are transformed into point nuclei and fibrillar nuclei, respectively. Unfortunately, it is impossible to write down an equation for the formation of new threadlike precursors at a given time t because it will depend on the subsequent development of

temperature and flow conditions whether a precursor with a certain length $L_p(t)$ will be long enough at a later time $t+\Delta t$, i.e. $L_p(t+\Delta t) \geq L_p^*$. This is an additional reason why, in general processing conditions, it will be necessary to model the length distribution of precursors. At the beginning of a new time step, one can look back to find the time interval(s) in the past during which precursors were formed that, in the mean time, have grown long enough to induce the growth of oriented semicrystalline structures. In the near future, the possibilities of predicting the transition from a spherical to an oriented morphology, based on the ideas presented here, will be investigated. At the moment, however, not enough experimental data are available to sufficiently reduce the number of free parameters.

2.5 Summary

The modeling framework presented in this chapter covers a broad range of length scales at which different processes take place. At the macroscopic level, the evolution of the degree of crystallinity and space filling, as well as the specific crystalline morphology, determine the evolution of the rheological properties of the material. We describe a crystallizing polymer as a suspension. Preliminary steps towards extending the suspension rheological modeling of crystallizing melts to the nonlinear viscoelastic regime have been indicated. In contrast to regular suspension theories, the mechanical properties of the constituent phases are not constant. The semicrystalline phase will harden as a result of secondary crystallization, which occurs in the amorphous regions within the crystallites. The amorphous phase presumably hardens because flow-induced precursors act as physical crosslinks. Thus, the evolution of rheological properties is linked to the molecular-scale processes of creation, growth, and disappearance of precursors.

Several aspects of the physics of flow-induced crystallization at the molecular level have not been resolved yet. Nevertheless, we have attempted, on the basis of previous theoretical developments and experimental data, to provide a means to capture the essentials of the relevant molecular processes. The kinetics of creation and disappearance of precursors, the growth of pointlike precursors into threadlike precursors, and the transition from a spherulitical to an oriented crystalline morphology have been formulated. In chapter 3, we will validate the modeling presented here by comparing it to experimental results on short-term shear-induced point nucleation, for which the limited number of free parameters allows such comparison. Validation with respect to anisotropic crystallization after strong short-term deformation, as well as continuous flow-induced crystallization, will be the objective of future work.

Chapter 3

Simulation of FIC experiments

Different parts of the theoretical framework presented in the previous chapter will be confronted with experimental data in the following. The ultimate objective is to be able to describe, in a quantitative manner, the characteristic phenomena observed under experimental as well as processing conditions. Specifically, we would like to predict

- the final number of spherulites and oriented crystallites per unit volume;
- the moment of transition from spherical to oriented morphologies;
- space filling and degree of crystallinity as a function of time;
- the evolution of rheological properties and probably other properties, which have not yet been considered, as a function of space filling and degree of crystallinity.

Two main subjects are covered here. First, the possibility to monitor quiescent and flow-induced crystallization processes by rheometry is discussed. Specifically, the storage modulus is related to space filling according to different scaling laws as well as on the basis of suspension rheology. The second subject is the validation of the theory of crystallization kinetics for the case that point nucleation dominates. Anisotropic flow-induced crystallization processes involve too many additional modeling parameters, related to the longitudinal growth and relaxation processes of precursors and nuclei, for a reliable validation. Therefore, attention is restricted to point nucleation here.

3.1 Materials and experimental methods

Different aspects of the evolving semicrystalline structure were studied by Hristova *et al.* [52] using in situ methods – optical microscopy (OM) and

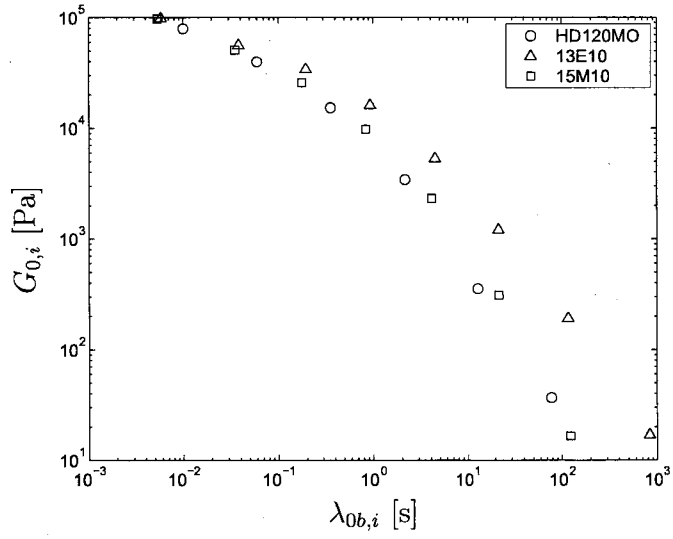

Figure 3.1: Linear viscoelastic relaxation spectra of the iPP melts HD120MO from Borealis [52, 124] and 13E10 and 15M10 from DSM [110, 124] at 135°C.

small- and wide-angle X-ray scattering (SAXS and WAXS) – as well as ex situ methods – differential scanning calorimetry (DSC) and environmental scanning electron microscopy (ESEM). Vega *et al.* [124] studied the evolution of linear viscoelastic rheological properties (storage modulus G' and loss angle δ) during crystallization.

Experimental results of both studies will be compared to predictions based on the theory developed in chapter 2. The experiments discussed in this chapter were performed during isothermal crystallization, following the fast cooling of a polymer melt from above the melting temperature T_m, where it was kept long enough to erase any deformation history, to the desired crystallization temperature T_c. Quiescent and flow-induced crystallization were studied, the latter by applying short-term shear flows of varying strengths and durations at the beginning of the isothermal crystallization process.

A linear isotactic polypropylene (iPP) HD120MO, manufactured by Borealis, was studied. The XPP model is applied here to simulate the experiments. This model requires nonlinear rheological data, which are not available for this material. The rheological data of the linear iPP 15M10 from DSM will be used instead. This material was characterized by Swartjes [110]. The linear viscoelastic relaxation spectrum is comparable to that of the Borealis iPP (figure 3.1). The crystallization parameters, the growth rate $G(T)$ and the number of available athermal precursors $N_{pa}(T)$, are those determined by Hristova *et al.* for HD120MO.

Table 3.1: Properties of the iPP melts HD120MO [52, 124] and 15M10 [110, 124].

Material	M_w [kg/mol]	M_w/M_n [–]	T_m [°C]
HD120MO	365	5.4	165
15M10	350	5.6	161

A general feature of crystallization induced by a short-term flow, applied at the beginning of the crystallization process, is that the final nucleation density is reached before any space filling can be noticed. The kinetics of precursor formation and nucleation therefore take place in essentially unbounded conditions; no significant volume fraction of the amorphous phase is crystallized yet during this period, which we will refer to as the early stage of crystallization. Consequently, the state of stress in the material is not disturbed by the presence of crystallites and it is not necessary to apply a suspension model when looking at the crystallization kinetics. Experiments conducted by Devaux *et al.* [23] showed that the extent of the early stage was of the order of 10^2s at $T_c = 136$°C. They used an iPP melt with a weight-averaged molecular weight $M_w = 338$kg/mol and polydispersity index $M_w/M_n = 6.45$, which is similar to the HD120MO melt considered here (table 3.1). The full modeling, including suspension rheology, will be applied to continuous flow experiments conducted by Vega *et al.* [124] in the near future. In the present work, however, only crystallization after short-term shear flow is considered. Nevertheless, it will be shown in the next section that the suspension rheology approach to flow-induced crystallization offers a possibility to accurately monitor the development of space filling. In this respect, it constitutes a significant improvement over methods that have been used up till now.

3.2 Monitoring crystallization by rheometry

Because in most cases it is not possible to determine the degree of crystallinity $\chi(t)$ or the space filling $\xi_g(t)$ in situ by means of optical microscopy, experimentalists have devised indirect methods to obtain these properties. For example, the degree of crystallinity is often related to the intensity measured with light scattering or X-ray diffraction techniques. A commonly used measure of space filling is the storage modulus G'. In this section, the relation between G' and ξ_g is investigated.

Vega *et al.* [124] determined the linear viscoelastic relaxation spectrum

of the iPP melt HD120MO by means of oscillatory shear rheometry. Next, they determined the storage modulus $G'(t)$ and the loss angle $\delta(t)$ during isothermal crystallization, at $T_c = 135°C$ and at $T_c = 145°C$, of samples that were sheared at different rates $\dot{\gamma}$ and for different durations t_s immediately after reaching T_c. Here, we consider the results obtained at 135°C with an angular frequency of 5rad/s, for the preshear conditions $\dot{\gamma} = 60s^{-1}$ and t_s = 0s, 3s, and 6s, and compare them to predictions based on different supposed relations between G' and ξ_g. The evolution of G' and δ during these experiments is shown in figure 3.2. Two phenomena, well-known from literature, are observed upon increasing the shear time (or shear strain). First, the effect of crystallization on G' shows up earlier. This is in accordance with the idea of a flow-enhanced nucleation rate. Secondly, for higher shear times, there is a distinct change in the slopes of the storage modulus and loss angle curves in the intermediate stage, where space filling becomes important and the increase, respectively decrease, of G' and δ is most conspicuous. The change in the slopes of the curves is an indication of the development of anisotropic semicrystalline structures.

In order to relate these rheological data to the evolution of space filling, we need to know how the dynamic moduli $G_0^*(t)$ and $G_1^*(t)$ of the individual phases develop during the crystallization process. Comparison of the data for the three experiments in the early stage of crystallization reveals that, during the shear period, the melt becomes more elastic: the storage modulus increases and the loss angle decreases. Since this effect is observed while $\xi_g \approx 0$, it must be the result of structure development in the amorphous phase. In chapter 2, changes in the rheology of the amorphous phase were related to the flow-induced creation of precursors. It will be shown later on in this chapter that no significant number of precursors is created after the flow has been stopped. Therefore, G'_0 and δ_0 are assumed constant and equal to the earliest measured values.

The rheological properties of the semicrystalline phase can only be determined in the plateau region, reached after a certain time, where both $\log(G')$ and δ become weak linear functions of $\log(t)$. Presumably, space filling is then completed and the crystallization process involves only perfection of the semicrystalline phase. The characteristic time t_1, indicating the transition from the space filling stage to the perfection stage, is defined by the intersection of the extrapolated linear fits of the $\log(G')$–$\log(t)$ data in these stages, as shown in figure 3.3. The value read from the G' axis at the intersection point is taken as $G'_1(t_1)$, i.e. the storage modulus of the semicrystalline phase at $t = t_1$. The corresponding loss angle $\delta_1(t_1)$ is defined as the value at $t = t_1$ of the extrapolated fit of δ versus $\log(t)$ in the plateau region. An alternative method is to derive the characteristic time t_1 from the loss angle data, and

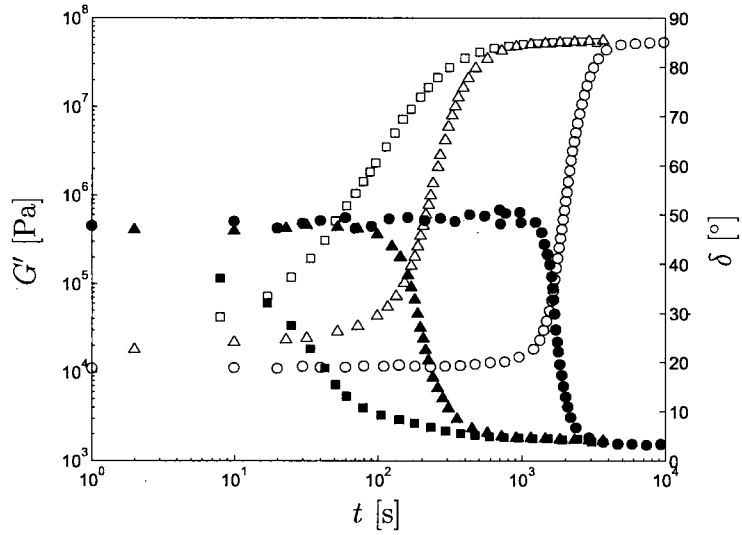

Figure 3.2: Evolution of the storage modulus (open symbols) and loss angle (filled symbols) during crystallization, measured in quiescent conditions (○,●) and after shearing at $\dot{\gamma} = 60\text{s}^{-1}$ for $t_s = 3\text{s}$ (△,▲) and $t_s = 6\text{s}$ (□,■) [124]. Part of the data points were omitted for the sake of clarity.

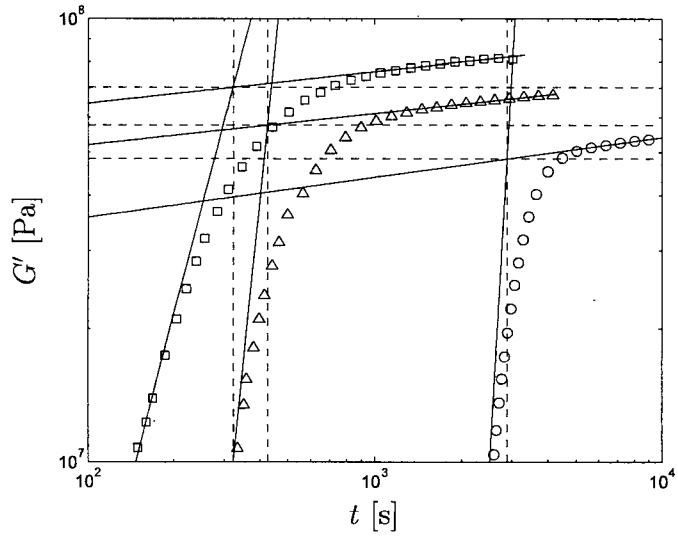

Figure 3.3: Close-up of the storage moduli from figure 3.2. Part of the data points were omitted and the curves corresponding to $t_s = 3\text{s}$ and $t_s = 6\text{s}$ were shifted vertically by factors 1.2 and 1.5, respectively, for the sake of clarity. The solid lines are fits of the data in the plateau region and in the region where the increase of G' is most conspicuous. The dashed lines indicate t_1 and $G'_1(t_1)$.

Table 3.2: Parameters for calculating the rheological properties and degree of crystallinity of the semicrystalline phase by means of equations 3.1, 3.2, and 3.4.

t_s [s]	t_1 [s]	$G'_1(t_1)$ [Pa]	$\delta_1(t_1)$ [°]	$\chi_1(t_1)$ [–]
0	$2.89 \cdot 10^3$	$4.83 \cdot 10^7$	3.48	–
3	$4.25 \cdot 10^2$	$4.80 \cdot 10^7$	4.83	$4.98 \cdot 10^{-1}$
6	$3.22 \cdot 10^2$	$4.68 \cdot 10^7$	4.97	$5.40 \cdot 10^{-1}$

t_s [s]	m	c_δ	c_χ
0	$9.00 \cdot 10^{-2}$	$-1.29 \cdot 10^{-1}$	–
3	$7.02 \cdot 10^{-2}$	$-3.40 \cdot 10^{-1}$	$5.75 \cdot 10^{-2}$
6	$7.11 \cdot 10^{-2}$	$-3.40 \cdot 10^{-1}$	0

determine $\delta_1(t_1)$ and $G'_1(t_1)$ from this. However, comparison revealed that the values of t_1 based on the storage modulus data were in better agreement with the onset of the plateau regions observed in the space filling and the degree of crystallinity measured during quiescent and flow-induced crystallization, respectively, which will be discussed next. Since it is unknown how the rheological properties of the semicrystalline phase develop in the earlier stages of crystallization, we simply assume that no secondary crystallization takes place up to $t = t_1$, and that G'_1 and δ_1 are given by the fits of the plateau regions for $t > t_1$. Thus

$$G'_1(t) = \begin{cases} G'_1(t_1) & \text{for } t \leq t_1 \\ G'_1(t_1)\left[\frac{t}{t_1}\right]^m & \text{for } t > t_1 \end{cases} \tag{3.1}$$

and

$$\delta_1(t) = \begin{cases} \delta_1(t_1) & \text{for } t \leq t_1 \\ \delta_1(t_1) + c_\delta \ln\left(\frac{t}{t_1}\right) & \text{for } t > t_1 \end{cases} . \tag{3.2}$$

The values of the parameters used in these equations, obtained from the rheological experiments, are given in table 3.2.

For the quiescent crystallization experiment, ξ_g was derived from in situ optical microscopy by Hristova *et al.* [52]. The result was verified using Schneider's rate equations, with the growth rate obtained from sequences of microscopic images of spherulites and assuming that all nuclei were present from the start of the crystallization process, which is justified by the observed narrow size distribution of the spherulites. Figure 3.4 shows the evolution of ξ_g during this experiment. It is seen that the space filling process is completed at $t \approx 3 \cdot 10^3$s, which agrees with t_1 obtained from the measured storage

modulus. The contribution of oriented crystallites, appearing in the flow-induced crystallization experiments, to ξ_g could not be determined accurately by optical means. Therefore, the degree of crystallinity χ, derived from in situ WAXS experiments by Hristova *et al.* [52], is used here to estimate ξ_g. By definition, ξ_g and χ are related according to

$$\xi_g(t) = \frac{\chi(t)}{\chi_1(t)} \tag{3.3}$$

with χ_1 the internal degree of crystallinity of the semicrystalline phase. Whereas ξ_g directly influences the effective rheological properties of the melt (from the point of view of suspension rheology it plays the role of the volume fraction ϕ) χ_1 determines the rheology of the semicrystalline phase, and thus influences the effective properties of the melt indirectly (in the linear viscoelastic regime through the dynamic modulus G_1^*).

The integrated WAXS intensities X_{WAXS} for the quiescent and flow-induced crystallization experiments are included in figure 3.4. Comparing the results of WAXS and OM for the quiescent melt, it is seen that X_{WAXS} is close to or even slightly higher than ξ_g up to $\xi_g = 0.3$. Since the degree of crystallinity is always smaller than the space filling, we conclude that $X_{WAXS} > \chi$. This is a consequence of the sensitivity of WAXS measurements: intensity peaks are caused not only by crystallites, but also by noncrystalline ordered structures. On the other hand, the values of t_1 derived from the storage modulus measured during flow-induced crystallization (table 3.2) correlate with the onset times of the plateaus in the WAXS data. So at least the time scale is correct, provided that t_1 corresponds to $\xi_g = 1$ as observed in the quiescent crystallization experiment. For $t > t_1$, the contribution of noncrystalline ordered phases to the scattered intensity is expected to be negligible, so that $X_{WAXS} \approx \chi$. The data in the plateau region can be fitted by a linear function $X_{WAXS}(t > t_1) \sim t$. This is probably an adequate measure of the internal degree of crystallinity χ_1. It is unknown, however, how χ and χ_1 develop during the space filling process. Like in the rheological experiments, it is assumed that no secondary crystallization takes place up to $t = t_1$:

$$\chi_1(t) = \begin{cases} \chi_1(t_1) & \text{for } t \leq t_1 \\ \chi_1(t_1) + c_\chi [t - t_1] & \text{for } t > t_1 \end{cases} . \tag{3.4}$$

Furthermore, for lack of better data, X_{WAXS} is taken as χ and the experimental data are scaled by equation 3.4, in accordance with equation 3.3, to obtain ξ_g. The result is shown in figure 3.5. The parameters used in equation 3.4 are included in table 3.2.

Although it was necessary to make some simplifying assumptions concerning the properties of the semicrystalline phase, the experimental results

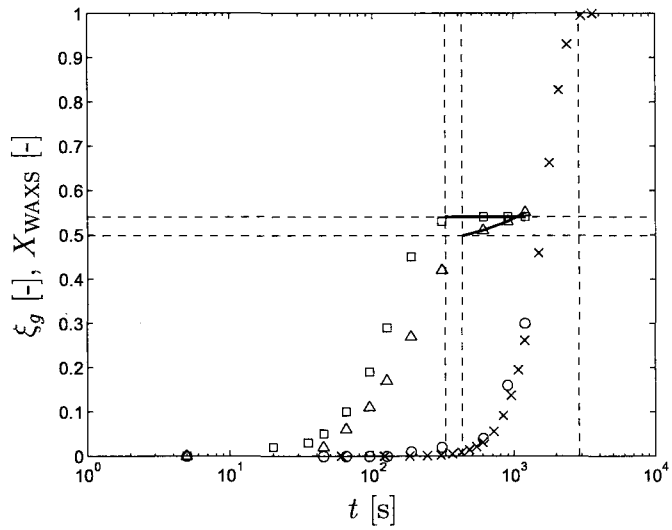

Figure 3.4: Space filling during quiescent crystallization, obtained from OM (×), along with the integrated WAXS intensity during quiescent crystallization (○) and after shearing at $\dot{\gamma} = 60\mathrm{s}^{-1}$ for $t_s = 3\mathrm{s}$ (△) and $t_s = 6\mathrm{s}$ (□). The solid lines are fits of the WAXS data in the plateau region. The dashed lines indicate t_1 and $\chi_1(t_1)$.

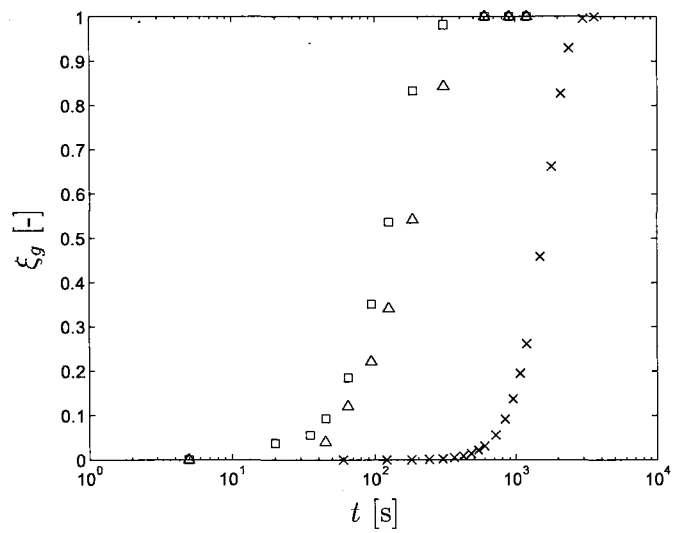

Figure 3.5: Space filling during quiescent crystallization, obtained from OM (×), and after shearing at $\dot{\gamma} = 60\mathrm{s}^{-1}$ for $t_s = 3\mathrm{s}$ (△) and $t_s = 6\mathrm{s}$ (□), estimated from WAXS as explained in the text.

discussed in this section will provide insight into the relation between the rheological properties of a crystallizing melt and its crystalline structure. Methods to monitor crystallization processes by means of dynamic rheological experiments can now be evaluated. Here, we consider two different kinds of methods: scaling laws and methods based on suspension models.

3.2.1 Scaling laws for the storage modulus

Because both $\log(G')$ versus $\log(t)$ and ξ_g versus $\log(t)$ have a characteristic sigmoidal shape, it seems reasonable to approximate ξ_g by a scaled storage modulus, which is easily measured by oscillatory shear rheometry. Khanna [64] proposed a simple linear scaling,

$$\xi_g(t) = \frac{G'(t) - G'_0(t)}{G'_1(t) - G'_0(t)}, \tag{3.5}$$

or, equivalently,

$$G'(t) = G'_0(t) + [G'_1(t) - G'_0(t)]\,\xi_g(t) . \tag{3.6}$$

Contrary to common practice, where the storage modulus is scaled between the values at the beginning and at the end of the experiment, the phase moduli G'_0 and G'_1, which are in general time-dependent, are used here.

It is not difficult to pinpoint the error in Khanna's approach: not G', but $\log(G')$ is similar in shape to ξ_g. So the logical choice would be to relate the space filling to the scaled logarithm of the storage modulus like

$$\xi_g(t) = \frac{\log(G'(t)) - \log(G'_0(t))}{\log(G'_1(t)) - \log(G'_0(t))}, \tag{3.7}$$

which can be rewritten in the form

$$G'(t) = G'_0(t)\left[\frac{G'_1(t)}{G'_0(t)}\right]^{\xi_g(t)} . \tag{3.8}$$

The right-hand side of equation 3.7 corresponds to the normalized storage modulus used by Pogodina *et al.* [94]. Figure 3.6 shows the storage modulus calculated by equations 3.6 and 3.8, using the experimentally obtained G'_0, G'_1, and ξ_g. Not surprisingly, Khanna's linear scaling law completely fails to predict the measured storage modulus. The logarithmic scaling law performs a lot better, but is still not quite accurate, especially at the longest shear time.

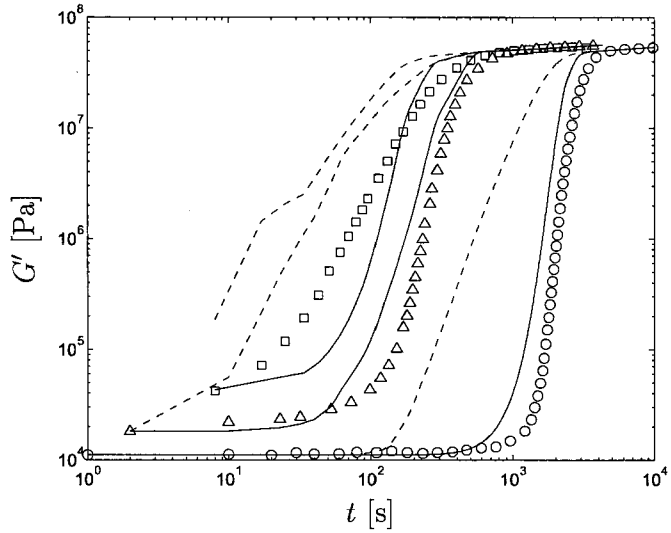

Figure 3.6: Evolution of the storage modulus in quiescent conditions (○) and after shearing at $\dot{\gamma} = 60\text{s}^{-1}$ for $t_s = 3\text{s}$ (△) and $t_s = 6\text{s}$ (□). The dashed lines correspond to Khanna's linear scaling law (equation 3.6). The solid lines correspond to the logarithmic scaling law (equation 3.8).

3.2.2 The storage modulus from suspension models

Based on the theory of suspension mechanics, discussed in the previous chapter, we predict that

$$\begin{aligned} G'(t) &= \text{Re}\{f_G^* G_0^*\} \\ &= f_G'(t)\, G_0' - f_G''(t)\, G_0'', \end{aligned} \tag{3.9}$$

which is a nonlinear function of G_0', G_0'', G_1', and G_1'' in the case of a non-dilute suspension of deformable particles, like the crystallizing polymer melts considered here. Two approaches to obtain G' from the experimentally determined space filling will be outlined next. In the first, the linear viscoelastic form of the classical elastic suspension model [62, 120], discussed in section 2.2.1, is applied. Solutions for the low-concentration and high-concentration regimes are thus obtained. An interpolation between the two limiting solutions is applied. The second approach is based on the linear viscoelastic form of the generalized self-consistent method [19, 20], discussed in section 2.2.2. The relative modulus f_G^* is in both cases obtained from the originally elastic models by applying the correspondence principle (section 2.2.3).

Tanner [112] proposed an interpolation between the theoretical relative moduli corresponding to low and high space filling, obtained from the clas-

sical first-order suspension theory, i.e. equations 2.17 and 2.22 or the corresponding dilute limits, equations 2.20 and 2.23, respectively. We introduce a weight function $w(\xi_g) \in [0,1]$ to interpolate between these asymptotic solutions. The effective dynamic modulus of the material is then written as

$$G^*(\xi_g) = [1 - w(\xi_g)] f_G^*(\xi_g) G_0^* + w(\xi_g) h_G^*(\xi_g) G_1^*. \tag{3.10}$$

The weight function should obviously satisfy the boundary conditions

$$\begin{aligned} w(0) &= 0; \\ w(1) &= 1. \end{aligned} \tag{3.11}$$

Furthermore, it should be of the order of ξ_g^2 or higher. This becomes clear when the assumption $|G_1^*| >> |G_0^*|$ is made. Note that equation 3.10 can then be replaced by two uncoupled equations for the storage modulus and the loss modulus. The dynamic equivalents of equations 2.20 and 2.23 under the mentioned assumption reduce to

$$\lim_{\xi_g \to 0} f_G^*(\xi_g) = 1 + \frac{15(1-\nu_0)\xi_g}{8 - 10\nu_0} \tag{3.12}$$

and

$$\lim_{\xi_g \to 1} h_G^*(\xi_g) = 1 - \frac{15(1-\nu_1)(1-\xi_g)}{7 - 5\nu_1}. \tag{3.13}$$

If both phases are incompressible ($\nu_0 = \nu_1 = 0.5$) it follows from equations 3.10, 3.12, and 3.13 that

$$G^*(\xi_g) = [1 - w(\xi_g)] \left[1 + \frac{5}{2}\xi_g\right] G_0^* + w(\xi_g) \left[\frac{5}{3}\xi_g - \frac{2}{3}\right] G_1^*. \tag{3.14}$$

In the limit $\xi_g \to 0$, equation 3.14 should attain the Einstein form $G^* = (1 + 5/2\xi_g)G_0^*$. This is the case if w goes to zero faster than ξ_g. Hence, for w a function at least of the order of ξ_g^2 should be chosen.

The weight function w can easily be defined such that the evolution of the storage modulus in the range of intermediate space filling is fitted accurately. A definition that satisfies the boundary conditions 3.11 is

$$\begin{aligned} w(\phi_0) &= \frac{1}{2}\left[\tanh\left(\ln\left(\left[\frac{\phi_0}{\phi_{0,1/2}}\right]^n\right)\right) + 1\right] \\ &= \frac{\left[\frac{\phi_0}{\phi_{0,1/2}}\right]^{2n}}{1 + \left[\frac{\phi_0}{\phi_{0,1/2}}\right]^{2n}}, \end{aligned} \tag{3.15}$$

where $\phi_0 = -\ln(1-\xi_g)$ is the unbounded volume fraction of crystallites, and $\phi_{0,1/2}$ and n determine the point where $w = 0.5$ and the slope of $w(\phi_0)$ in that point. The quiescent crystallization experiment is fitted quite accurately with $\phi_{0,1/2} = 3$ and $n = 1$, as shown in figure 3.7. For the flow-induced crystallization experiments, using the same values of the fitting parameters, the prediction of G' becomes worse as the shear time increases. The results are still satisfying for $t_s = 3$s, but clearly not for $t_s = 6$s. The same conclusions can be drawn when comparing the calculated loss angle to the experimental data (figure 3.8).

In order to avoid the use of fitting parameters that don't have a clear physical meaning, like in the interpolation method outlined above, it is preferable to apply a suspension model that is valid over the entire range of space filling. The generalized self-consistent method (GSCM), discussed in section 2.2.2, is used here because it was shown to give accurate results for elastic suspensions [19,20,100]. The differential effective medium approximation (DEMA), also discussed in section 2.2.2, was tested as well. This model failed at higher ξ_g, as expected [19,20], and the results are therefore not shown here.

One of the main advantages of the GSCM, given the spherical and fibrillar morphologies typically encountered in flow-induced crystallization processes of polymers, is that it provides solutions for suspensions of spheres as well as suspensions of fibers. Because, in the flow-induced crystallization experiments, spherulites and oriented crystallites were present simultaneously, the 3D GSCM (equation 2.26) is first applied to calculate the effective rheological properties of the amorphous phase containing the spherulites. The result is used as the matrix in the 2D GSCM, with the oriented crystallites as the particles, to calculate the effective rheological properties of the melt. We assume that all oriented crystallites are immediately aligned in the flow direction, so that only the longitudinal shear modulus, given by equation A.8 in the appendix, needs to be determined. Incompressibility was assumed for both phases: $\nu_0 = \nu_1 = 0.5$. The volume fraction of spherulites in the amorphous phase, used in the 3D GSCM, is given by

$$x^{sph} = \frac{\xi_g^{sph}}{1 - \xi_g + \xi_g^{sph}}, \tag{3.16}$$

where ξ_g is the total space filling derived from the WAXS measurements and ξ_g^{sph} is the space filling contributed by the spherulites only, as obtained from the OM experiments. In the 2D GSCM, the space filling due to the oriented crystallites,

$$\xi_g^{fib} = \xi_g - \xi_g^{sph}, \tag{3.17}$$

was used.

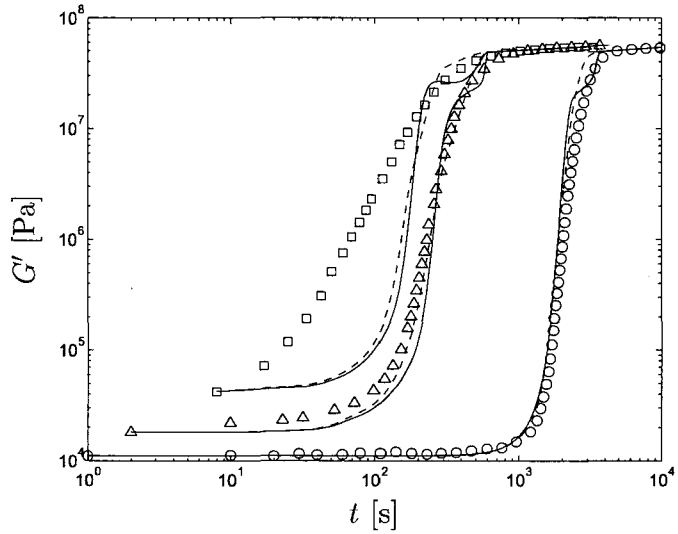

Figure 3.7: Evolution of the storage modulus in quiescent conditions (○) and after shearing at $\dot{\gamma} = 60\text{s}^{-1}$ for $t_s = 3\text{s}$ (△) and $t_s = 6\text{s}$ (□). The dashed lines were obtained by the interpolation method (equations 3.10 and 3.15) with $\phi_{0,1/2} = 3$ and $n = 1$. The solid lines correspond to the GSCM (equations 2.26 and A.8) with $\nu_0 = \nu_1 = 0.5$.

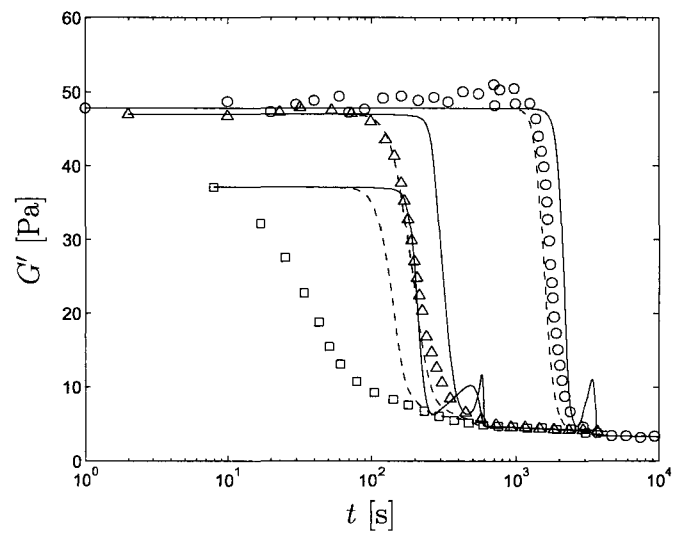

Figure 3.8: Evolution of the loss angle in quiescent conditions (○) and after shearing at $\dot{\gamma} = 60\text{s}^{-1}$ for $t_s = 3\text{s}$ (△) and $t_s = 6\text{s}$ (□). The dashed lines were obtained by the interpolation method (equations 3.10 and 3.15) with $\phi_{0,1/2} = 3$ and $n = 1$. The solid lines correspond to the GSCM (equations 2.26 and A.8) with $\nu_0 = \nu_1 = 0.5$.

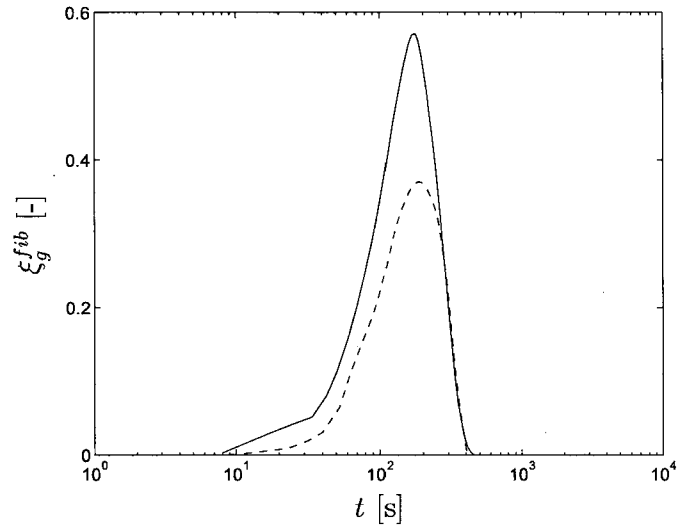

Figure 3.9: Space filling due to oriented crystallites after shearing at $\dot{\gamma} = 60\text{s}^{-1}$ for $t_s = 3\text{s}$ (dashed lines) and $t_s = 6\text{s}$ (solid lines), derived from the total space filling (WAXS) and the space filling due to spherulites (OM) using equation 3.17.

Figure 3.7 shows the evolution of the storage modulus for the three experiments. For high ξ_g, an oscillation occurs in the prediction of the GSCM, which is even more prominent in the loss angle (figure 3.8). In appendix A, it is shown that this behavior is an inherent feature of the solution of the quadratic equation 2.26, which gives the relative shear modulus, when the Poisson ratio of the matrix is close to 0.5. For the quiescent crystallization experiment, a better fit was obtained with $\nu_0 = 0.49$ and $\nu_1 = 0.5$, but the simulations of the flow-induced crystallization experiments could not be improved. In fact, the oscillation in these simulations is partly due to ξ_g^{fib}, as calculated from equation 3.17, which reaches its maximum around $t = 2 \cdot 10^2\text{s}$ and then falls back to zero (figure 3.9). This behavior of ξ_g^{fib} can probably be explained by the overgrowth of the oriented crystallites by the more numerous spherulites. However, given the uncertainties in the assumptions that we made to obtain ξ_g from the WAXS data, the real space filling due to oriented crystallites may differ significantly from the calculations shown in figure 3.9.

Apart from this, for the quiescent melt and the melt sheared for 3s, $G'(t)$ as predicted by the GSCM agrees very well with the experimental results. For the melt sheared for 6s, a large difference between the simulation and the data is observed. This is probably due to the inaccuracy of the assumptions concerning the rheological properties of the semicrystalline phase, and possibly also of the amorphous phase, during the space filling process. Figure 3.8

shows that the difference between the predicted and measured loss angles already becomes large for the 3s shear experiment. Nevertheless, the successful simulation of the oscillatory shear experiments during quiescent crystallization is a promising result. In the case of flow-induced crystallization, there is room for improvement in the modeling of the crystallization kinetics and the resulting morphology.

3.3 Early-stage crystallization kinetics

The evolution of the unbounded number of homogeneous precursors, as described by equation 2.74, is the result of a balance of two processes. First, the creation of precursors, the rate of which is determined by the driving forces I_{pq} and I_{pf} and the number of athermal precursors obtained per unit time $\dot{T}\partial N_{pa}/\partial T$ and, secondly, the depletion of available precursors, characterized by τ_p. This parameter is essentially a residence time related to the probability that a precursor survives and, as expressed in equation 2.76, is the resultant of two characteristic time scales: τ_{pn} for nucleation and τ_{pd} for dissolution into the melt. The experiments considered here are isothermal, except for the initial cooling to the crystallization temperature T_c. Therefore, it follows from equation 2.81 or equation 2.83 that the number of heterogeneous nuclei is constant from the moment T_c is reached and depends on the number of heterogeneous precursors with activation temperatures above T_c that are contained in the material prior to cooling. The cooling rate ($\dot{T} = 15°\text{Cmin}^{-1}$) is high in comparison to the kinetics of nucleation and growth, which are initially very slow, so the size distribution of these athermal nuclei is narrow.

As already mentioned, the kinetics in the early stage of crystallization take place in unbounded conditions. This is a fortunate circumstance since, when space filling increases, the velocity field will become nonuniform due to disturbances caused by the crystallites. Then the deformation of molecules in the amorphous phase can no longer be represented by a single elastic Finger tensor derived from the macroscopic flow conditions. As long as creation of precursors is confined to the early stage of crystallization, it is not affected by these disturbances.

Different models for the creation of pointlike precursors and the transformation of these precursors into nuclei, which grow into spherulites, will be tested in the next sections. The calculated space filling and nucleation density will be compared to the experimental data of Hristova *et al.* [52] for quiescent crystallization and short-term shear-induced crystallization at a constant shear rate $\dot{\gamma} = 60\text{s}^{-1}$ and varying shear times $t_s = 1, 2, 3, 4$, and 6s. The crystallization temperature $T_c = 135°\text{C}$ was used.

Because only point nucleation was simulated, despite the fact that oriented crystallites appeared in the experiments where a flow was applied, the space filling due to spherulites ξ_g^{sph}, obtained from optical microscopy, is probably more useful for validating the results than the total space filling derived from WAXS. Therefore, the calculated space filling will be compared to ξ_g^{sph}. In all experiments, the number of oriented crystallites is two or more orders of magnitude smaller than the number of spherulites. So the errors in the calculated numbers of pointlike precursors, due to the fact that some of these grow into threadlike precursors, are negligible. In the future, when we include a growth model to predict the number of oriented crystallites, our objective will be to fit the total space filling while at the same time predicting the correct numbers of oriented crystallites as well as spherulites.

3.3.1 Characterization of the nucleation process

The images obtained by optical microscopy during and after application of short-term shear flow, as well as in quiescent conditions, showed that all spherulites were approximately the same size, indicating that they had started to grow at the same moment, or at least within a short time interval. Therefore, it is assumed that $I_{pq} = 0$ so that, in quiescent conditions, there is no sporadic creation of precursors. Furthermore, τ_{pn} is set to zero. Then dissolution is negligible relative to nucleation because all precursors are nucleated immediately ($\tau_p \approx \tau_{pn} = 0$) The kinetics of such fast nucleation processes are explained in appendix B. Thus, the nucleation rate is simply given by

$$\dot{N}_n(t) = I_{pf}(t) \; . \tag{3.18}$$

This is not surprising at a crystallization temperature of 135°C, which is about 30 degrees below the limit of sporadic nucleation [58].

3.3.2 Effects of macroscopic flow and molecular deformation

As a starting point, the flow-induced nucleation models of Liedauer *et al.* [73] and Zuidema *et al.* [131, 132] are compared. These were given in equations 2.69 and 2.71, respectively, and are here applied to the creation of precursors. According to the Liedauer model, the driving force is proportional to the shear rate,

$$I_{pf}(t) = g_p \left[\frac{\dot{\gamma}(t)}{\dot{\gamma}_n} \right]^2 \; . \tag{3.19}$$

Because $\dot{\gamma}$ is constant here, the only adjustable parameter is the ratio $g_p/\dot{\gamma}_n$. In agreement with experimental results, this model predicts that the unbounded volume fraction $\phi_0 = -\ln(1-\xi_g)$ becomes proportional to t^3 after cessation of flow. This is shown in figure 3.10, commonly known as an Avrami plot, where $\log(\phi_0)$ is plotted against $\log(t)$.

In figure 3.11, the calculated time evolution of the number of point nuclei N_{np} in each flow-induced crystallization experiment is plotted. The corresponding experimentally determined numbers of spherulites are also included. As mentioned before, these were all created at the same time, since they were all the same size, and were counted some time after they had become visible. The data points are plotted at an arbitrary position along the time axis in the figure. Because $\tau_{pn} = 0$, there are no precursors.

The tremendous increase of the final number of crystallites with increasing shear time, observed experimentally, is not captured by the model. Moreover, in Hristova *et al.*'s experiment with the highest shear time (90s at a shear rate of $4s^{-1}$, not shown in the figure) the predicted difference between the largest and smallest crystallite diameters, based on the measured growth rate of 51nm/s, is 9.2μm. This value lies well above the resolution limit of the microscope, which is about 2μm. Hence a distribution of diameters would have to be observed, but this is not the case.

According to the model of Zuidema *et al,* the driving force is proportional to the recoverable strain in the melt, quantified by the second invariant of the deviatoric part of the elastic Finger tensor,

$$I_{pf}(t) = g_p J_2\left(\boldsymbol{B}_e^d(t)\right) . \tag{3.20}$$

Because several studies indicate that flow-induced nucleation primarily involves the high molecular weight fraction of the melt [1,60,103,107,127,132] only a single mode of the relaxation spectrum, the one corresponding to the longest relaxation time, is considered. First, we look at the results without relating the relaxation time to structure development within the amorphous phase. Due to the fact that $J_2(\boldsymbol{B}_e^d(t))$ does not vanish instantaneously at $t = t_s$ but gradually relaxes to zero, nucleation continues for $t > t_s$. Consequently, an even broader distribution of crystallite diameters will be predicted than by the Liedauer model. After the recoverable strain has relaxed, the Avrami plot again attains the slope of 3 (figure 3.12) and the number of nuclei becomes constant (figure 3.13). The figures clearly demonstrate that the strong influence of shear time on the final number of crystallites is still missing.

These results are not surprising, given the experimental evidence supporting the idea that flow-induced creation of precursors is a self-enhancing process [57]. The shear rate is a macroscopic parameter. Hence, in the Liedauer

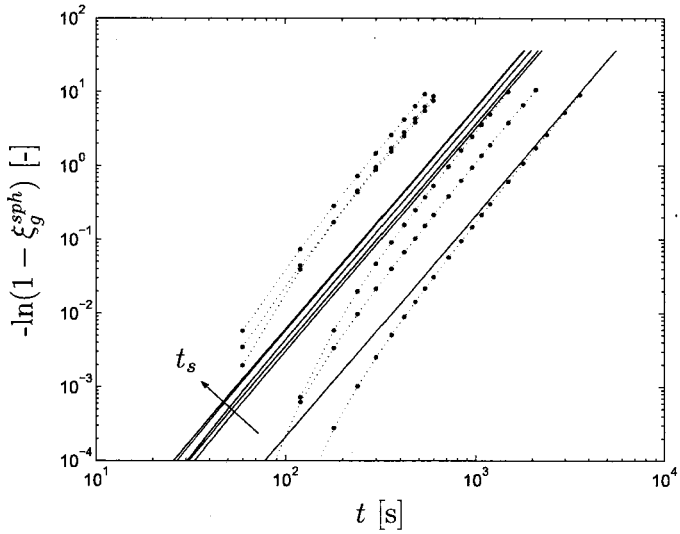

Figure 3.10: Avrami plot for $\dot{\gamma} = 60\text{s}^{-1}$ and $t_s = 0, 1, 2, 3, 4$, and 6s. The solid lines are simulations based on equation 3.19; $\tau_{pn} = 0$ so that the nucleation rate is given by equation 3.18. Dots connected by a thin dotted line represent the data points of one experiment.

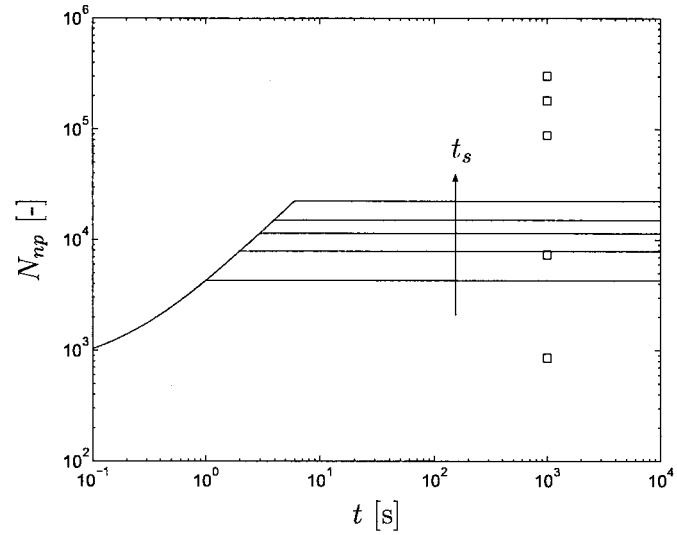

Figure 3.11: Evolution of the number of point nuclei for $\dot{\gamma} = 60\text{s}^{-1}$ and $t_s = 1, 2, 3, 4$, and 6s according to equation 3.19; $\tau_{pn} = 0$ so that the nucleation rate is given by equation 3.18. The squares indicate the numbers of spherulites determined by optical microscopy.

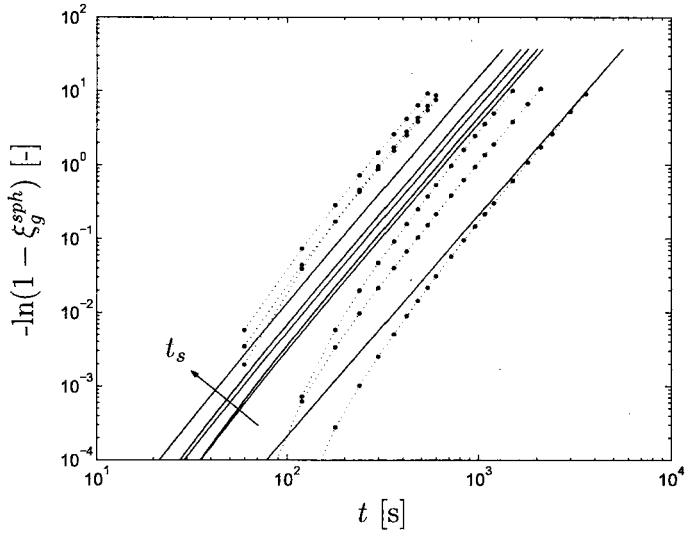

Figure 3.12: Avrami plot for $\dot{\gamma} = 60\text{s}^{-1}$ and $t_s = 0, 1, 2, 3, 4$, and 6s. The solid lines are simulations based on equation 3.20; q is taken equal to q_0 (from the rheological characterization of the melt [110]) and $\tau_{pn} = 0$ so that the nucleation rate is given by equation 3.18. Dots connected by a thin dotted line represent the data points of one experiment.

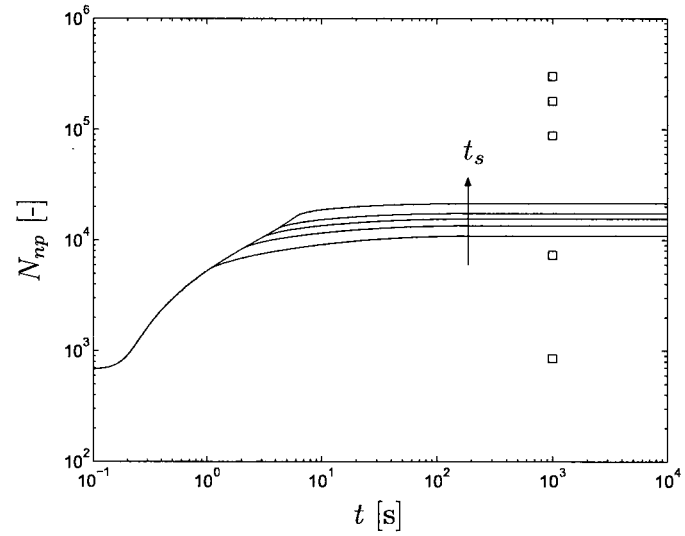

Figure 3.13: Evolution of the number of point nuclei for $\dot{\gamma} = 60\text{s}^{-1}$ and $t_s = 1, 2, 3, 4$, and 6s according to equation 3.20; q is taken equal to q_0 (from the rheological characterization of the melt [110]) and $\tau_{pn} = 0$ so that the nucleation rate is given by equation 3.18. The squares indicate the numbers of spherulites determined by optical microscopy.

model, no connection with molecular dynamics is made. In contrast, the Zuidema model offers the possibility to capture the self-enhancing nature of precursor creation by correlating rheological parameters with the changing microstructure of the melt. In a first attempt to get a better agreement with experimental results, following the approach of Zuidema [131] outlined in section 2.4.2, the relaxation time was made a function of the number of flow-induced nuclei according to equation 2.84. This indeed improved the predictions of the final numbers of crystallites. But with an increasing relaxation time, a large number of nuclei is created even after cessation of flow. As a result, contrary to the OM observations, a very broad distribution of spherulite sizes is predicted. Moreover, a fundamental difference between theory and experiment is observed in the Avrami plot: its slope does not reach the final value of 3 observed experimentally, which indicates a constant number of crystallites. Assuming a relation between the relaxation time and the number of precursors (instead of nuclei) does not make any difference in this case, simply because all precursors become nuclei at the moment they are created.

These problems can be solved in two steps. First, the assumption is made that nucleation is inhibited during flow. From a physical point of view, this implies that velocity gradients tend to tear apart folded-chain lamellae or prevent their formation in the first place. The optical microscopy data seem to support this idea: only in the experiments with the highest shear times, e.g. $t_s = 90\text{s}$ at a rate of $\dot{\gamma} = 4\text{s}^{-1}$, a few nuclei were already observed before t_s. But the vast majority appeared at a later time, with no visible distribution of sizes. The characteristic time of nucleation is therefore written as

$$\tau_{pn} = \begin{cases} \infty & \text{for } \dot{\gamma} \neq 0\,; \\ 0 & \text{for } \dot{\gamma} = 0\,, \end{cases} \tag{3.21}$$

where the shear rate is again defined as $\dot{\gamma} = \sqrt{2\boldsymbol{D} : \boldsymbol{D}}$. The second step taken to improve the results is to make the relaxation time a function of the developing structure. However, as explained in section 2.4.3, we make the branching parameter q of the XPP model, and consequently the orientation and stretch relaxation times, a function of the number of flow-induced precursors instead of the number of flow-induced nuclei, as Zuidema *et al.* did for the relaxation time of the Leonov model.

Equation 3.21 resembles the athermal nucleation model of Eder *et al.* [28], expressed in equation 2.82, where heterogeneous precursors become stable at their characteristic temperature. Here we have defined an additional 'athermal' mechanism, which interferes with all other nucleation processes as follows. As long as a flow is applied, precursors are created and 'put on hold'.

As soon as the flow is switched off, all precursors that exceed the critical size at the current temperature are transformed into nuclei. This is a rather crude model: it will not work for continuous flow, because then it will predict that no precursors are nucleated at all. So the infinite $\tau_{pn}(\dot{\gamma} \neq 0)$ should be replaced by a finite value. Furthermore, $\tau_{pn}(\dot{\gamma} = 0)$ will be greater than zero in the range of shallow undercooling ($T_u < T < T_m$). It seems reasonable to assume a smooth transition between these two values, which takes place at a characteristic shear rate $\dot{\gamma}_c > 0$. Equation 3.21 can then be extended to a multi-mode model, where to every precursor species a different $\dot{\gamma}_c$ is assigned at which this species becomes stable. However, for the constant shear rate experiments discussed here, the single-mode formulation according to equation 3.21 suffices.

Although the assumption $\tau_{pd} \to \infty$ may not hold when τ_{pn} is large, dissolution of precursors will also be neglected during flow. Given the fact that most shear times are more than one order of magnitude smaller than the relaxation times λ_b and λ_s belonging to the highest mode, which are expected (or at least one of which is expected) to correlate with τ_{pd}, the number of dissolved precursors is probably small in these experiments. Equation 3.18 is now replaced by two separate expressions. One describes the creation of precursors during flow,

$$\dot{N}_{pf}(t) = I_{pf}(t) \text{ for } t < t_s\,, \tag{3.22}$$

while the other gives the evolution the number of flow-induced nuclei after the flow has been stopped,

$$\dot{N}_{nf}(t) = I_{pf}(t) \text{ for } t \geq t_s\,. \tag{3.23}$$

Figures 3.14 and 3.15 show the results obtained using equation 3.20 with the above assumptions. There are now two adjustable parameters: g_p in equation 3.20 and a in equation 2.87. The increase of the final number of crystallites with increasing shear time is at least qualitatively predicted. And secondly, also in accordance with the experimental data, the number of nuclei does not change significantly after cessation of flow. These results are easily understood. Precursors are created during flow at a rate determined by the deformation of molecules, which is characterized by $J_2(\boldsymbol{B}_e^d(t))$. Because of the coupling of the relaxation time with the number of precursors, this is a strongly self-enhancing process. At $t = t_s$, all precursors are immediately nucleated and the relaxation time abruptly drops to its original value. The self-enhancing effect vanishes, and the precursors created afterwards are far less numerous than those created during flow.

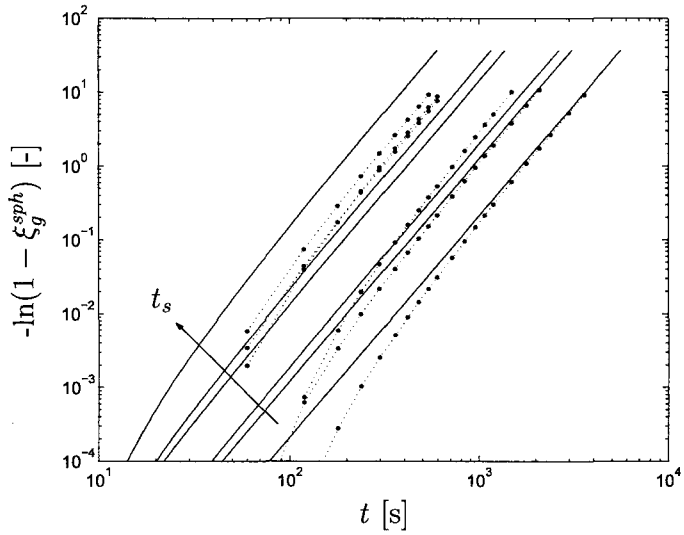

Figure 3.14: Avrami plot for $\dot{\gamma} = 60\text{s}^{-1}$ and $t_s = 0, 1, 2, 3, 4$, and 6s. The solid lines are simulations based on equation 3.20; q is given by equation 2.87 and τ_{pn} by equation 3.21. Dots connected by a thin dotted line represent the data points of one experiment.

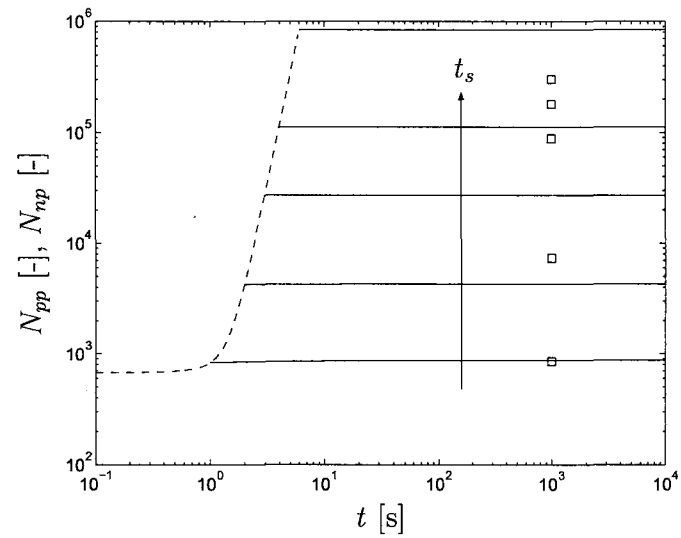

Figure 3.15: Evolution of the number of pointlike precursors (dashed lines) and point nuclei (solid lines) for $\dot{\gamma} = 60\text{s}^{-1}$ and $t_s = 1, 2, 3, 4$, and 6s according to equation 3.20; q is given by equation 2.87 and τ_{pn} by equation 3.21. The squares indicate the numbers of spherulites determined by optical microscopy.

The question remains whether equivalent or even better results would have been obtained with Janeschitz-Kriegl's athermal flow-induced nucleation model, discussed in section 2.4.2. Unfortunately, insufficient data are at our disposal for such an investigation. Even if we determine the number of spherulites obtained in quiescent conditions as a function of the crystallization temperature, which is a straightforward procedure, it is still unknown which of these spherulites were initiated by precursors of the homogeneous kind, which can grow longitudinally. With the number of homogeneous precursors as a function of temperature it would be possible to fit the Janeschitz-Kriegl model, in combination with a model for the flow-induced growth of precursors, to experimental data. This will be a subject of future research.

3.3.3 The role of molecular orientation and stretch

At this point, it is interesting to see if any conclusions regarding the nature of the driving force behind precursor formation can be drawn. For example, one could hypothesize that molecular orientation alone suffices to increase $\dot{N}_{pf}$ and therefore assume $I_{pf}(t)$ in equations 3.22 and 3.23 linearly proportional to the second invariant of the deviatoric part of the orientation tensor,

$$I_{pf}(t) = g_p J_2\left(\boldsymbol{S}^d(t)\right) , \tag{3.24}$$

where

$$J_2\left(\boldsymbol{S}^d\right) = \frac{J_2\left(\boldsymbol{B}_e^d\right)}{J_1\left(\boldsymbol{B}_e\right)^2} = \frac{J_2\left(\boldsymbol{B}_e^d\right)}{9\Lambda^4} . \tag{3.25}$$

The time-dependent numbers of precursors and nuclei calculated on the basis of this hypothesis are plotted in figure 3.16. The model now completely fails to predict the increase in the final number of nuclei as a function of shear time. It was attempted to make the self-enhancing effect stronger by replacing the linear relation between the branching parameter q and the number of flow-induced precursors, equation 2.87, by a power law. However, this yielded no better results.

From these observations, we conclude that creation of precursors as a result of orientation of chain segments is not sufficient to explain the tremendous increase in the final nucleation density with increasing shear time. Stretch of the chains' contour paths, characterized by the scalar stretch parameter $\Lambda = \sqrt{J_1(\boldsymbol{B}_e)/3}$, is apparently essential. This parameter appears in $J_2(\boldsymbol{B}_e^d)$ to the fourth power. In order to investigate the influence of chain stretch, the following expression is proposed:

$$I_{pf}(t) = g_p\left[\Lambda(t)^m - 1\right] . \tag{3.26}$$

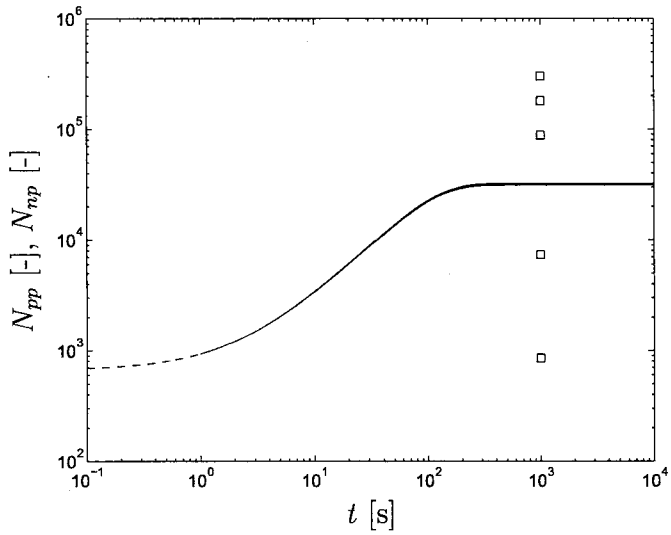

Figure 3.16: Evolution of the number of pointlike precursors (dashed lines) and point nuclei (solid lines) for $\dot{\gamma} = 60\text{s}^{-1}$ and $t_s = 1, 2, 3, 4$, and 6s according to equation 3.24; q is given by equation 2.87 and τ_{pn} by equation 3.21. The squares indicate the numbers of spherulites determined by optical microscopy.

The exponent m is assumed constant. For different values of m, we can try fitting the experimental data by varying the parameters g_p and a again. The results are shown in figures 3.17 to 3.20 for different shear rates and shear times. It is obvious that a linear relationship between I_{pf} and Λ is not enough. When m is equal to three or higher, however, the results are about as satisfactory as those obtained using $J_2(\boldsymbol{B}_e^d)$. With $m = 4$ we essentially get the original Zuidema model again, because the effect of orientation is negligible and the second invariant of the deviatoric elastic Finger tensor depends on the stretch parameter to the power four.

3.3.4 Depletion of ordered species in the melt

The fact that the high molecular weight fraction of the melt most strongly influences the kinetics of flow-induced nucleation is supposedly due to the fact that only chains that are sufficiently long and/or sufficiently branched can stay in an ordered state long enough to form precursors. One might expect that at some point, the amorphous phase simply runs out of these high molecular weight chains. Somani *et al.* [103] observed and investigated this phenomenon. Their results show that an increasing portion of the molecular weight distribution (characterized by $M > M^*$) can be used for the creation

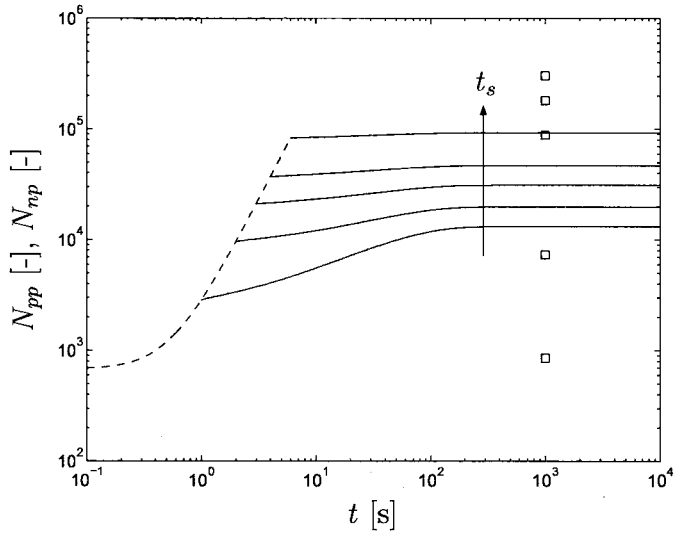

Figure 3.17: Evolution of the number of pointlike precursors (dashed lines) and point nuclei (solid lines) for $\dot{\gamma} = 60\text{s}^{-1}$ and $t_s = 1, 2, 3, 4$, and 6s according to equation 3.26 with $m = 1$; q is given by equation 2.87 and τ_{pn} by equation 3.21. The squares indicate the numbers of spherulites determined by optical microscopy.

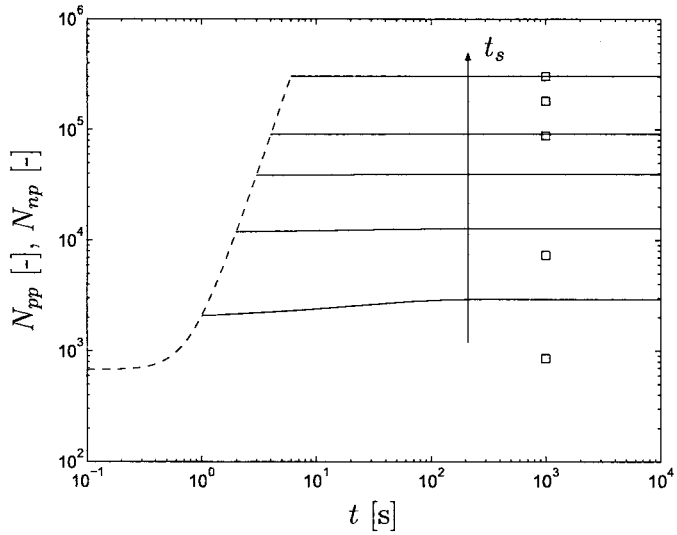

Figure 3.18: Evolution of the number of pointlike precursors (dashed lines) and point nuclei (solid lines) for $\dot{\gamma} = 60\text{s}^{-1}$ and $t_s = 1, 2, 3, 4$, and 6s according to equation 3.26 with $m = 2$; q is given by equation 2.87 and τ_{pn} by equation 3.21. The squares indicate the numbers of spherulites determined by optical microscopy.

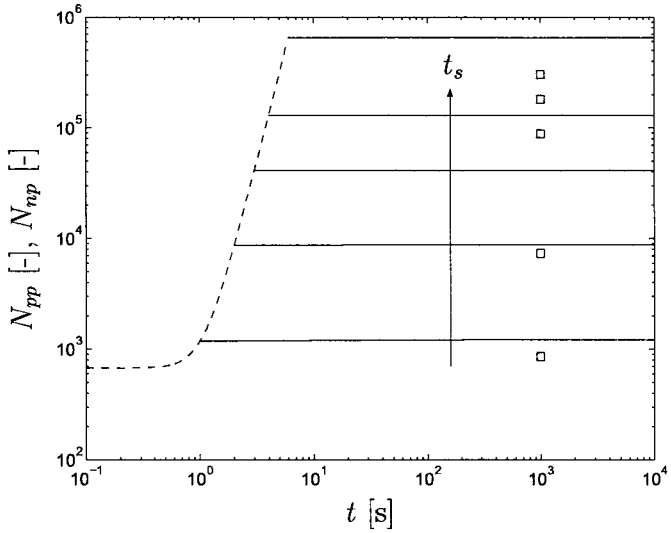

Figure 3.19: Evolution of the number of pointlike precursors (dashed lines) and point nuclei (solid lines) for $\dot{\gamma} = 60\text{s}^{-1}$ and $t_s = 1, 2, 3, 4$, and 6s according to equation 3.26 with $m = 3$; q is given by equation 2.87 and τ_{pn} by equation 3.21. The squares indicate the numbers of spherulites determined by optical microscopy.

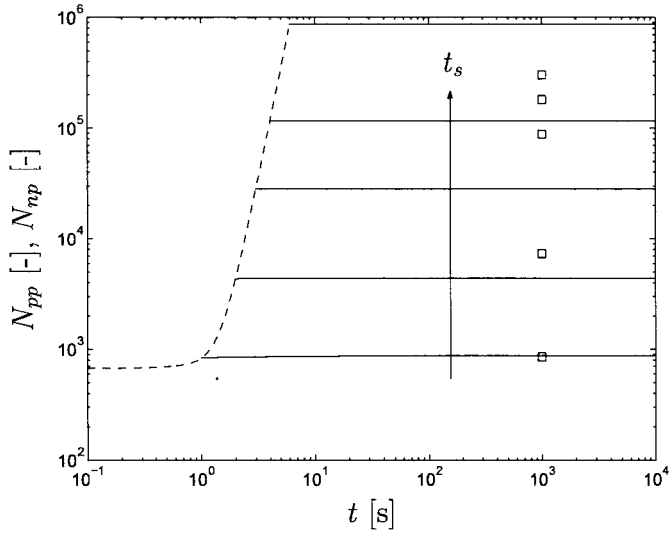

Figure 3.20: Evolution of the number of pointlike precursors (dashed lines) and point nuclei (solid lines) for $\dot{\gamma} = 60\text{s}^{-1}$ and $t_s = 1, 2, 3, 4$, and 6s according to equation 3.26 with $m = 4$; q is given by equation 2.87 and τ_{pn} by equation 3.21. The squares indicate the numbers of spherulites determined by optical microscopy.

of precursors when the shear rate is increased ($M^* = M^*(\dot{\gamma})$). Eventually, some plateau is reached. Increasing the shear rate further, no larger portion of the molecular weight distribution becomes available for the creation of precursors. We model this kind of depletion simply by rewriting the driving force as

$$I_{pf}(t) = \tilde{g}_p(t)\left[\Lambda(t)^4 - 1\right], \tag{3.27}$$

where $\tilde{g}_p(t)$ is the product of g_p and a function that 'dampens' I_{pf} as more and more molecules are taken out of the high molecular weight tail of the distribution. The simplest choice is a linear function of the number of flow-induced precursors and nuclei,

$$\tilde{g}_p(t) = g_p\left[1 - \frac{N_{pf}(t) + N_{nf}(t)}{(N_{pf} + N_{nf})_{max}}\right]. \tag{3.28}$$

The denominator on the right-hand side represents the maximum number of crystallizable species, which is temperature- and flow rate-dependent. Figures 3.21 and 3.22 show that this linear saturation law significantly improves the agreement with experimental data. The same results were obtained using $J_2(\boldsymbol{B}_e^d)$ instead of $\Lambda^4 - 1$ in equation 3.27. The flow-induced crystallization model now contains three adjustable parameters: g_p, a, and $(N_{pf} + N_{nf})_{max}$. In the experiments considered here, the space filling due to spherulites and the spherulitic nucleation density are predicted quantitatively using constant values for these parameters. Their dependence on temperature and flow conditions has not been explored yet.

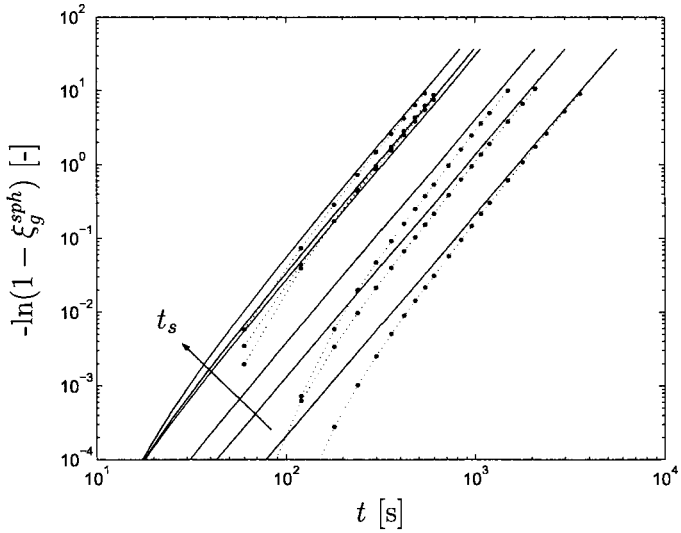

Figure 3.21: Avrami plot for $\dot{\gamma} = 60\text{s}^{-1}$ and $t_s = 0, 1, 2, 3, 4$, and 6s. The solid lines are simulations based on equation 3.27; q is given by equation 2.87, τ_{pn} by equation 3.21, and $\tilde{g}_p$ by equation 3.28. Dots connected by a thin dotted line represent the data points of one experiment.

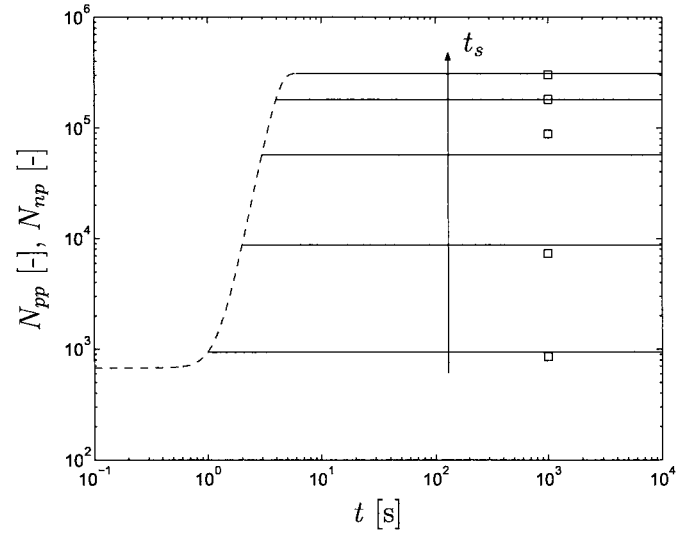

Figure 3.22: Evolution of the number of pointlike precursors (dashed lines) and point nuclei (solid lines) for $\dot{\gamma} = 60\text{s}^{-1}$ and $t_s = 1, 2, 3, 4$, and 6s according to equation 3.27; q is given by equation 2.87, τ_{pn} by equation 3.21, and $\tilde{g}_p$ by equation 3.28. The squares indicate the numbers of spherulites determined by optical microscopy.

Chapter 4

Conclusions

The evolution of the linear viscoelastic properties of a linear isotactic polypropylene during crystallization could be described accurately using a suspension model. This was demonstrated by comparison of model predictions, using information on the semicrystalline structure provided by Hristova *et al.* [52] as input, to oscillatory shear experiments conducted by Vega *et al.* [124] during crystallization. The suspension rheology approach presents a major improvement in comparison to a simple scaling method (Khanna *et al.* [64]) that, unfortunately, is widely accepted in polymer crystallization studies.

A theory of crystallization kinetics was formulated, based on the concept of precursors (unstable nuclei). Precursors were introduced to explain the fact that all spherulites obtained in isothermal flow-induced crystallization experiments have the same size. For this purpose, the assumption was made that nucleation, i.e. the formation and growth of folded-chain lamellae on the lateral surfaces of the precursors, is impeded by flow. The kinetics of precursor creation were coupled to rheology, following the ideas of Zuidema *et al.* [131,132]. The results were compared to short-term shear-induced crystallization experiments of Hristova *et al.* [52], where the shear rate was kept constant. The number of spherulites and the time evolution of space filling due to these spherulites could simultaneously be described, in a qualitative sense, as a function of shear time.

Creation of precursors was shown to be determined by molecular stretch, whereas molecular orientation alone could not explain the experimental results. Using only the stretch as the driving force behind the creation process, the simulations were as good as using the Zuidema model, where both stretch and orientation were taken into account.

The modeling was extended with a description of the depletion of available chains with a sufficiently high molecular weight to form precursors. The existence of such a process was demonstrated experimentally by Somani *et*

al. [103]. Taking this into account, the increase of the number of spherulites with increasing shear time could be predicted quantitatively.

A model for the growth of pointlike precursors into threadlike precursors was presented. The validation of this model will be possible if the number of free parameters is reduced. In the near future, experiments will be designed specifically for this purpose.

Another subject of future work is the simulation of continuous flow-induced crystallization experiments, where the effects of precursors, nuclei, and crystallites on the rheology of the crystallizing polymer, and the effects of flow on the formation of precursors, nucleation of these precursors, and the development of isotropic as well as anisotropic structures all take place at the same time. It is important that the appropiate experiments are carried out simultanously to support this modeling.

Finally, it will be interesting to depart from the concept of a flow-enhanced rate of sporadic creation of precursors and see if the idea of flow as a promotor of the development of athermal precursors, recently put forward by Janeschitz-Kriegl and coworkers [55–59, 108], enables us to describe flow-induced crystallization processes as well.

Bibliography

[1] S. Acierno, B. Palomba, H. H. Winter, and N. Grizzuti. Effect of molecular weight on the flow-induced crystallization of isotactic poly(1-butene). *Rheologica Acta*, 42:243–250, 2003.

[2] S. Acierno and N. Grizzuti. Measurements of the rheological behavior of a crystallizing polymer by an "inverse quenching" technique. *Journal of Rheology*, 47:563–576, 2003.

[3] A. Agbossou, A. Bergeret, K. Benzarti, and N. Alberola. Modelling of the viscoelastic behaviour of amorphous thermoplastic/glass beads composites based on the evaluation of the complex Poisson's ratio of the polymer matrix. *Journal of Materials Science*, 28:1963–1972, 1993.

[4] G. C. Alfonso and F. Azzurri. Formation and disappearance of shear induced nucleation precursors. In *Polymer Crystallization and Structure Formation in Processing*, Linz, September 2003. Proceedings of the PC2003 International Mini-Conference.

[5] M. Avrami. Kinetics of phase change I. General theory. *Journal of Chemical Physics*, 7:1103–1112, 1939.

[6] M. Avrami. Kinetics of phase change II. Transformation-time relations for random distribution of nuclei. *Journal of Chemical Physics*, 8:212–224, 1940.

[7] M. Avrami. Kinetics of phase change III. Granulation, phase change, and microstructure. *Journal of Chemical Physics*, 9:177–184, 1941.

[8] K. Avramova. Kinetics of overall phase transition in changing size system. *Crystal Research and Technology*, 37:491–500, 2002.

[9] J. G. Berryman. Long-wavelength propagation in composite elastic media I. Spherical inclusions. *Journal of the Acoustical Society of America*, 68:1809–1819, 1980.

[10] J. G. Berryman. Long-wavelength propagation in composite elastic media II. Ellipsoidal inclusions. *Journal of the Acoustical Society of America*, 68:1820–1831, 1980.

[11] K. Boutahar, C. Carrot, and J. Guillet. polypropylene during crystallization from the melt as a model for the rheology of molten-filled polymers. *Journal of Applied Polymer Science*, 60:103–114, 1996.

[12] K. Boutahar, C. Carrot, and J. Guillet. Crystallization of polyolefins from rheological measurements - relation between the transformed fraction and the dynamic moduli. *Macromolecules*, 31:1921–1929, 1998.

[13] J. F. Brady. The Einstein viscosity correction in n dimensions. *International Journal of Multiphase Flow*, 10:113–114, 1983.

[14] J. Braun, H. Wippel, G. Eder, and H. Janeschitz-Kriegl. Industrial solidification processes in polybutene-1. Part II–Influence of shear flow. *Polymer Engineering and Science*, 43:188–203, 2003.

[15] H. Brenner. Rheology of a dilute suspension of axisymmetric Brownian particles. *International Journal of Multiphase Flow*, 1:195–341, 1974.

[16] V. Brucato, S. Piccarolo, and G. Titomanlio. Crystallization kinetics in relation to polymer processing. *Makromolekulare Chemie, Macromolecular Symposia*, 68:245–255, 1993.

[17] M. Burger, V. Capasso, and G. Eder. Modelling of polymer crystallization in temperature fields. *Zeitschrift für Angewandte Mathematik und Mechanik*, 82:51–63, 2002.

[18] R. M. Christensen. Viscoelastic properties of heterogeneous media. *Journal of the Mechanics and Physics of Solids*, 17:23–41, 1969.

[19] R. M. Christensen and K. H. Lo. Solutions for effective shear properties in three phase sphere and cylinder models. *Journal of the Mechanics and Physics of Solids*, 27:315–330, 1979.

[20] R. M. Christensen. A critical evaluation for a class of micro-mechanics models. *Journal of the Mechanics and Physics of Solids*, 38:379–404, 1990.

[21] I. Coccorullo, R. Pantani, and G. Titomanlio. Crystallization kinetics and solidified structure in iPP under high cooling rates. *Polymer*, 44:307–318, 2003.

[22] S. Coppola, N. Grizzuti, and P. L. Maffettone. Microrheological modeling of flow-induced crystallization. *Macromolecules*, 34:5030–5036, 2001.

[23] N. Devaux, B. Monasse, J.-M. Haudin, P. Moldenaers, and J. Vermant. Rheooptical study of the early stages of flow enhanced crystallization in isotactic polypropylene. *Rheologica Acta*, 43:210–222, 2004.

[24] R. A. Dickie. Heterogeneous polymer-polymer composites. I. Theory of viscoelastic properties and equivalent mechanical models. *Journal of Applied Polymer Science*, 17:45–63, 1973.

[25] R. A. Dickie, M.-F. Cheung, and S. Newman. Heterogeneous polymer-polymer composites. II. Preparation and properties of model systems. *Journal of Applied Polymer Science*, 17:65–78, 1973.

[26] R. A. Dickie and M.-F. Cheung. Heterogeneous polymer-polymer composites. III. Viscoelastic properties of acrylic polyblends. *Journal of Applied Polymer Science*, 17:79–94, 1973.

[27] M. Doi and S. F. Edwards. *The Theory of Polymer Dynamics.* Oxford University Press, Oxford, 1986.

[28] G. Eder, H. Janeschitz-Kriegl, and S. Liedauer. Crystallization processes in quiescent and moving polymer melts under heat transfer conditions. *Progress in Polymer Science*, 15:629–714, 1990.

[29] G. Eder. Fundamentals of structure formation in crystallizing polymers. In K. Hatada, T. Kitayama, and O. Vogl, editors, *Macromolecular Design of Polymeric Materials*, pages 763–784. Marcel Dekker, New York, 1996.

[30] G. Eder. Mathematical modelling of crystallization processes as occurring in polymer processing. *Nonlinear Analysis, Theory, Methods & Applications*, 30:3807–3815, 1997.

[31] G. Eder and H. Janeschitz-Kriegl. Structure development during processing: crystallization. In H. E. H. Meijer, editor, *Processing of Polymers*, pages 269–342. VCH Verlagsgesellschaft mbH, Weinheim, 1997.

[32] J. D. Eshelby. The determination of the elastic field of an ellipsoidal inclusion and related problems. *Proceedings of the Royal Society of London A*, 241:376–396, 1957.

[33] J. C. Fisher, J. H. Hollomon, and D. Turnbull. Nucleation. *Journal of Applied Physics*, 19:775–784, 1948.

[34] L. V. Gibiansky and G. W. Milton. On the effective viscoelastic moduli of two-phase media. I. Rigorous bounds on the complex bulk modulus. *Proceedings of the Royal Society of London A*, 440:163–188, 1993.

[35] L. V. Gibiansky, G. W. Milton, and J. G. Berryman. On the effective viscoelastic moduli of two-phase media. III. Rigorous bounds on the complex shear modulus in two dimensions. *Proceedings of the Royal Society of London A*, 455:2117–2149, 1999.

[36] D. Graebling, R. Muller, and J.-F. Palierne. Linear viscoelastic behavior of some incompatible polymer blends in the melt. Interpretation of data with a model of emulsion of viscoelastic liquids. *Macromolecules*, 26:320–329, 1993.

[37] Z. Hashin. The elastic moduli of heterogeneous materials. *Transactions of the ASME, Series E,* 84, *Journal of Applied Mechanics*, 29:143–150, 1962.

[38] Z. Hashin and S. Shtrikman. A variational approach to the theory of the elastic behaviour of multiphase materials. *Journal of the Mechanics and Physics of Solids*, 11:127–140, 1963.

[39] Z. Hashin and B. W. Rosen. The elastic moduli of fiber-reinforced materials. *Transactions of the ASME, Series E,* 86, *Journal of Applied Mechanics*, 31:223–232, 1964.

[40] Z. Hashin. On elastic behaviour of fibre reinforced materials of arbitrary transverse phase geometry. *Journal of the Mechanics and Physics of Solids*, 13:119–134, 1965.

[41] Z. Hashin. Viscoelastic behavior of heterogeneous media. *Transactions of the ASME, Series E,* 87, *Journal of Applied Mechanics*, 32:630–636, 1965.

[42] Z. Hashin. Complex moduli of viscoelastic composites - I. General theory and application to particulate composites. *International Journal of Solids and Structures*, 6:539–552, 1970.

[43] Z. Hashin. Complex moduli of viscoelastic composites - II. Fiber reinforced materials. *International Journal of Solids and Structures*, 6:797–807, 1970.

[44] Z. Hashin. Theory of fiber reinforced materials. Technical Report NASA-CR-1974, NASA Center for Aerospace Information, 1972.

[45] E. L. Heeley, C. K. Poh, W. Li, A. Maidens, W. Bras, I. P. Dolbnya, A. J. Gleeson, N. J. Terrill, J. P. A. Fairclough, P. D. Olmsted, R. I. Ristic, M. J. Hounslow, and A. J. Ryan. Are metastable, pre-crystallisation, density-fluctuations a universal phenomena? *Faraday Discussions*, 122:343–361, 2002.

[46] E. L. Heeley, A. V. Maidens, P. D. Olmsted, W. Bras, I. P. Dolbnya, J. P. A. Fairclough, N. J. Terrill, and A. J. Ryan. Early stages of crystallization in isotactic polypropylene. *Macromolecules*, 36:3656–3665, 2003.

[47] R. Hill. Theory of mechanical properties of fibre-strengthened materials: I. Elastic behaviour. *Journal of the Mechanics and Physics of Solids*, 12:199–212, 1964.

[48] R. Hill. Theory of mechanical properties of fibre-strengthened materials: II. Inelastic behaviour. *Journal of the Mechanics and Physics of Solids*, 12:213–218, 1964.

[49] R. Hill. A self-consistent mechanics of composite materials. *Journal of the Mechanics and Physics of Solids*, 13:213–222, 1965.

[50] R. Hill. Theory of mechanical properties of fibre-strengthened materials: III. Self-consistent model. *Journal of the Mechanics and Physics of Solids*, 13:189–198, 1965.

[51] J. D. Hoffman and J. I. Lauritzen. Crystallization of bulk polymers with chain folding: theory of growth of lamellar spherulites. *Journal of Research of the National Bureau of Standards. Section A, Physics and Chemistry*, 65:297–336, 1961.

[52] D. G. Hristova, G. W. M. Peters, and H. E. H. Meijer. Flow induced crystallization: effect of flow strength and temperature. In *Proceedings of the 228th ACS National Meeting*, Philadelphia, August 2004. CD-ROM.

[53] M. Hütter, G. C. Rutledge, and R. C. Armstrong. Crystal shapes and crystallization in continuum modeling. *Physics of Fluids*, 17:014107-1–014107-13, 2005.

[54] W. R. Hwang, M. A. Hulsen, and H. E. H. Meijer. Direct simulations of particle suspensions in a viscoelastic fluid in sliding biperodic frames. *Journal of Non-Newtonian Fluid Mechanics*, 121:15–33, 2004.

[55] H. Janeschitz-Kriegl. Conditions of nucleation in crystallizable polymers: reconnaissance of positions – a critical evaluation. *Colloid and Polymer Science*, 275:1121–1135, 1997.

[56] H. Janeschitz-Kriegl, E. Ratajski, and H. Wippel. The physics of athermal nuclei in polymer crystallization. *Colloid and Polymer Science*, 277:217–226, 1999.

[57] H. Janeschitz-Kriegl, E. Ratajski, and M. Stadlbauer. Flow as an effective promotor of nucleation in polymer melts: a quantitative evaluation. *Rheologica Acta*, 42:355–364, 2003.

[58] H. Janeschitz-Kriegl. How to understand nucleation in crystallizing polymer melts under real processing conditions. *Colloid and Polymer Science*, 281:1157–1171, 2003.

[59] H. Janeschitz-Kriegl and E. Ratajski. Kinetics of polymer crystallization under processing conditions: transformation of dormant nuclei by the action of flow. *Polymer*, 46:3856–3870, 2005.

[60] F. Jay, J.-M. Haudin, and B. Monasse. Shear-induced crystallization of polypropylenes: effect of molecular weight. *Journal of Materials Science*, 34:2089–2102, 1999.

[61] P. Jerschow. *Crystallization of Polypropylene. New Experiments, Evaluation Methods and Coice of Material Compositions.* PhD thesis, Johannes Kepler Universität Linz, 1994.

[62] E. H. Kerner. The elastic and thermo-elastic properties of composite media. *Proceedings of the Physical Society of London B*, 69:808–813, 1956.

[63] R. Ketzmerick and H. C. Öttinger. Simulation of a non-Markovian process modelling contour length fluctuation in the Doi–Edwards model. *Continuum Mechanics and Thermodynamics*, 1:113–124, 1989.

[64] Y. P. Khanna. Rheological mechanism and overview of nucleated crystallization kinetics. *Macromolecules*, 26:3639–3643, 1993.

[65] A. N. Kolmogorov. On the statistical theory of the crystallization of metals. *Bulletin of the Academy of Sciences of the USSR, Mathematics Series*, 1:355–359, 1937.

[66] R. G. Larson. *Constitutive Equations for Polymer Melts and Solutions.* Butterworth Publishers, Stoneham, 1988.

[67] R. G. Larson, T. Sridhar, L. G. Leal, G. H. McKinley, A. E. Likhtman, and T. C. B. McLeish. Definitions of entanglement spacing and time constants in the tube model. *Journal of Rheology*, 47:809–818, 2003.

[68] J. I. Lauritzen and J. D. Hoffman. Theory of formation of polymer crystals with folded chains in dilute solution. *Journal of Research of the National Bureau of Standards. Section A, Physics and Chemistry*, 64:73–102, 1960.

[69] L. Li and W. H. de Jeu. Shear-induced smectic ordering as a precursor of crystallization in isotactic polypropylene. *Macromolecules*, 36:4862–4867, 2003.

[70] L. Li and W. H. de Jeu. Shear-induced smectic ordering in the melt of isotactic polypropylene. *Physical Review Letters*, 92:075506-1–075506-3, 2004.

[71] L. Li and W. H. de Jeu. Shear-induced smectic ordering and crystallisation of isotactic polypropylene. *Faraday Discussions*, 128:299–319, 2005.

[72] I. Lieberwirth. *Orientation-Induced Evolution of Crystal Morphologies in Semi-Crystalline Polymers.* PhD thesis, Technische Universiteit Eindhoven, 2001.

[73] S. Liedauer, G. Eder, H. Janeschitz-Kriegl, P. Jerschow, W. Geymayer, and E. Ingolic. On the kinetics of shear induced crystallization of polypropylene. *International Polymer Processing VIII*, 3:236–244, 1993.

[74] A. E. Likhtman and T. C. B. McLeish. Quantitative theory for linear dynamics of linear entangled polymers. *Macromolecules*, 35:6332–6343, 2002.

[75] C. W. Macosko. *Rheology: Principles, Measurements, and Applications.* VCH Verlagsgesellschaft mbH, Weinheim, 1994.

[76] S. E. Mall-Gleissle, W. Gleissle, G. H. McKinley, and H. Buggisch. The normal stress behavior of suspensions with viscoelastic matrix fluids. *Rheologica Acta*, 41:61–76, 2002.

[77] T. C. B. McLeish and R. G. Larson. Molecular constitutive equations for a class of branched polymers: the pom-pom polymer. *Journal of Rheology*, 42:81–110, 1998.

[78] G. W. Milton and J. G. Berryman. On the effective viscoelastic moduli of two-phase media. II. Rigorous bounds on the complex shear modulus in three dimensions. *Proceedings of the Royal Society of London A*, 453:1849–1880, 1997.

[79] M. Muthukumar. Molecular modelling of nucleation in polymers. *Philosophical Transactions of the Royal Society of London A*, 361:539–556, 2003.

[80] M. Muthukumar. Nucleation in polymer crystallization. *Advances in Chemical Science*, 128:1–26, 2004.

[81] A. Nogales, G. R. Mitchell, and A. S. Vaughan. Anisotropic crystallization in polypropylene induced by deformation of a nucleating agent network. *Macromolecules*, 36:4898–4906, 2003.

[82] A. N. Norris. A differential scheme for the effective moduli of composites. *Mechanics of Materials*, 4:1–16, 1985.

[83] A. N. Norris, A. J. Callegari, and P. Sheng. A generalized differential effective medium theory. *Journal of the Mechanics and Physics of Solids*, 33:525–543, 1985.

[84] P. D. Olmsted, W. C. K. Poon, T. C. B. McLeish, N. J. Terrill, and A. J. Ryan. Spinodal-assisted crystallization in polymer melts. *Physical Review Letters*, 81:373–376, 1998.

[85] J.-F. Palierne. Linear rheology of viscoelastic emulsions with interfacial tension. *Rheologica Acta*, 29:204–214, 1990. Errata available at http://www.mxpl.net.

[86] G. W. M. Peters. Private communication.

[87] G. W. M. Peters and F. P. T. Baaijens. Modelling of non-isothermal viscoelastic flows. *Journal of Non-Newtonian Fluid Mechanics*, 68:205–224, 1997.

[88] C. J. S. Petrie. The rheology of fibre suspensions. *Journal of Non-Newtonian Fluid Mechanics*, 87:369–402, 1999.

[89] N. Phan-Thien. Constitutive equation for concentrated suspensions in Newtonian liquids. *Journal of Rheology*, 39:679–695, 1995.

[90] N. Phan-Thien and D. C. Pham. Differential multiphase models for polydispersed suspensions and particulate solids. *Journal of Non-Newtonian Fluid Mechanics*, 72:305–318, 1997.

[91] N. Phan-Thien, X.-J. Fan, and B. C. Khoo. A new constitutive model for monodispersed suspensions of spheres at high concentrations. *Rheologica Acta*, 38:297–304, 1999.

[92] G. E. Pike and C. H. Seager. Percolation and conductivity: a computer study. I. *Physical Review B*, 10:1421–1434, 1974.

[93] N. V. Pogodina and H. H. Winter. polypropylene crystallization as a physical gelation process. *Macromolecules*, 31:8164–8172, 1998.

[94] N. V. Pogodina, H. H. Winter, and S. Srinivas. Strain effects on physical gelation of crystallizing isotactic polypropylene. *Journal of Polymer Science, Part B: Polymer Physics*, 37:3512–3519, 1999.

[95] N. V. Pogodina, V. P. Lavrenko, S. Srinivas, and H. H. Winter. Rheology and structure of isotactic polypropylene near the gel point: quiescent and shear-induced crystallization. *Macromolecules*, 42:9031–9043, 2001.

[96] P. Rubio and M. H. Wagner. Letter to the editor: a note added to "Molecular constitutive equations for a class of branched polymers: the pom-pom polymer" [J. Rheol. 42, 81 (1998)]. *Journal of Rheology*, 43:1709–1710, 1999.

[97] A. J. Ryan, J. P. A. Fairclough, N. J. Terrill, P. D. Olmsted, and W. C. K. Poon. A scattering study of nucleation phenomena in polymer crystallisation. *Faraday Discussions*, 112:13–29, 1999.

[98] W. Schneider, A. Köppl, and J. Berger. Non-isothermal crystallization of polymers. *International Polymer Processing*, 2:151–180, 1988.

[99] H. See, P. Jiang, and N. Phan-Thien. Concentration dependence of the linear viscoelastic properties of particle suspensions. *Rheologica Acta*, 39:131–137, 2000.

[100] J. Segurado and J. Llorca. A numerical approximation to the elastic properties of sphere-reinforced composites. *Journal of the Mechanics and Physics of Solids*, 50:2107–2121, 2002.

[101] M. Seki, D. W. Thurman, J. P. Oberhauser, and J. A. Kornfield. Shear-mediated crystallization of isotactic polypropylene: the role of long chain-long chain overlap. *Macromolecules*, 35:2583–2594, 2002.

[102] E. S. G. Shaqfeh and G. H. Fredrickson. The hydrodynamic stress in a suspension of rods. *Physics of Fluids A*, 2:7–24, 1990.

[103] R. H. Somani, B. S. Hsiao, A. Nogales, S. Srinivas, A. H. Tsou, I. Sics, F. J. Balta-Calleja, and T. A. Ezquerra. Structure development during shear flow-induced crystallization of i-PP: in-situ small-angle X-ray scattering study. *Macromolecules*, 33:9385–9394, 2000.

[104] R. H. Somani, B. S. Hsiao, A. Nogales, H. Fruitwala, S. Srinivas, and A. H. Tsou. Structure development during shear flow induced crystallization of i-PP: in situ wide-angle X-ray diffraction study. *Macromolecules*, 34:5902–5909, 2001.

[105] R. H. Somani, L. Yang, B. S. Hsiao, I. Sics, N. V. Pogodina, H. H. Winter, P. K. Agarwal, H. A. Fruitwala, and A. H. Tsou. Orientation-induced crystallization in isotactic polypropylene melt by shear deformation. *Macromolecular Symposia*, 185:105–117, 2002.

[106] R. H. Somani, L. Yang, B. S. Hsiao, P. K. Agarwal, H. A. Fruitwala, and A. H. Tsou. Shear-induced precursor structures in isotactic polypropylene melt by in-situ rheo-SAXS and rheo-WAXD studies. *Macromolecules*, 35:9096–9104, 2002.

[107] R. H. Somani, L. Yang, B. S. Hsiao, T. Sun, N. V. Pogodina, and A. Lustiger. Shear-induced molecular orientation and crystallization in isotactic polypropylene: effects of the deformation rate and strain. *Macromolecules*, 38:1244–1255, 2005.

[108] M. Stadlbauer, H. Janeschitz-Kriegl, G. Eder, and E. Ratajski. New extensional rheometer for creep flow at high tensile stress. Part II. Flow induced nucleation for the crystallization of iPP. *Journal of Rheology*, 48:631–639, 2004.

[109] G. Strobl. *The Physics of Polymers: Concepts for Understanding their Structures and Behavior.* Springer, Berlin, 1997.

[110] F. H. M. Swartjes. *Stress Induced Crystallization in Elongational Flow.* PhD thesis, Technische Universiteit Eindhoven, 2001.

[111] R. I. Tanner. A suspension model for low shear rate polymer solidification. *Journal of Non-Newtonian Fluid Mechanics*, 102:397–408, 2002.

[112] R. I. Tanner. On the flow of crystallizing polymers I. Linear regime. *Journal of Non-Newtonian Fluid Mechanics*, 112:251–268, 2003.

[113] N. J. Terrill, P. A. Fairclough, E. Towns-Andrews, B. U. Komanschek, R. J. Young, and A. J. Ryan. Density fluctuations: the nucleation event in isotactic polypropylene crystallization. *Polymer*, 39:2381–2385, 1998.

[114] D. G. Thomas. Transport characteristics of suspensions VIII. A note on the viscosity of Newtonian suspensions of uniform spherical particles. *Journal of Colloid Science*, 20:267–277, 1965.

[115] M. C. Tobin. Theory of phase transition kinetics with growth site impingement. I. Homogeneous Nucleation. *Journal of Polymer Science: Polymer Physics Edition*, 12:399–406, 1974.

[116] M. C. Tobin. The theory of phase transition kinetics with growth site impingement. II. Heterogeneous Nucleation. *Journal of Polymer Science: Polymer Physics Edition*, 14:2253–2257, 1976.

[117] S. Torquato. Effective stiffness tensor of composite media–I. Exact series expansions. *Journal of the Mechanics and Physics of Solids*, 45:1421–1448, 1997.

[118] S. Torquato. Effective stiffness tensor of composite media: II. Applications to isotropic dispersions. *Journal of the Mechanics and Physics of Solids*, 46:1411–1440, 1998.

[119] C. Tribout, B. Monasse, and J. M. Haudin. Experimental study of shear-induced crystallization of an impact polypropylene copolymer. *Colloid and Polymer Science*, 274:197–208, 1996.

[120] S. Uemura and M. Takayanagi. Application of the theory of elasticity and viscosity of two-phase systems to polymer blends. *Journal of Applied Polymer Science*, 10:113–125, 1966.

[121] J. C. van der Werff and C. G. de Kruif. Hard-sphere colloidal dispersions: the scaling of rheological properties with particle size, volume fraction, and shear rate. *Journal of Rheology*, 33:421–454, 1989.

[122] J. van Meerveld. A method to extract the monomer friction coefficient from the linear viscoelastic behavior of linear, entangled polymer melts. *Rheologica Acta*, 43:615–623, 2004.

[123] J. van Meerveld, G. W. M. Peters, and M. Hütter. Towards a rheological classification of flow induced crystallization experiments of polymer melts. *Rheologica Acta*, 44:119–134, 2004.

[124] J. F. Vega, D. G. Hristova, and G. W. M. Peters. Flow-induced crystallization and rheology of isotactic polypropylene: effects of molecular architecture. Unpublished work.

[125] W. M. H. Verbeeten. *Computational Melt Rheology.* PhD thesis, Technische Universiteit Eindhoven, 2001.

[126] W. M. H. Verbeeten, G. W. M. Peters, and F. P. T. Baaijens. Differential constitutive equations for polymer melts: the extended Pom-Pom model. *Journal of Rheology*, 45:823–843, 2001.

[127] S. Vleeshouwers and H. E. H. Meijer. A rheological study of shear induced crystallization. *Rheologica Acta*, 35:391–399, 1996.

[128] L. J. Walpole. On bounds for the overall elastic moduli of inhomogeneous systems - I. *Journal of the Mechanics and Physics of Solids*, 14:151–162, 1966.

[129] A. Ziabicki. Generalized theory of nucleation kinetics. IV. Nucleation as diffusion in the space of cluster dimensions, positions, orientations, and internal structure. *Journal of Chemical Physics*, 85:3042–3056, 1986.

[130] A. Ziabicki. Crystallization of polymers in variable external conditions IV. Isothermal crystallization in the presence of variable tensile stress or hydrostatic pressure. *Colloid and Polymer Science*, 277:752–761, 1999.

[131] H. Zuidema. *Flow-Induced Crystallization of Polymers; Application to Injection Moulding.* PhD thesis, Technische Universiteit Eindhoven, 2000.

[132] H. Zuidema, G. W. M. Peters, and H. E. H. Meijer. Development and validation of a recoverable strain-based model for flow-induced crystallization of polymers. *Macromolecular Theory and Simulations*, 10:447–460, 2001.

Appendix A

Evaluation of the generalized self-consistent method

The results of the GSCM [19,20] for suspensions of elastic particles in an elastic matrix are presented here. These can be rewritten for linear viscoelastic materials by replacing the static elastic moduli by complex dynamic moduli according to the correspondence principle (section 2.2.3). The dependence of f_G on the phase Poisson ratios ν_0 and ν_1 is investigated.

A.1 Spherical particles

For a suspension of spheres, the relative shear modulus f_G is obtained from equation 2.26 with the parameters A, B, and C from table A.1. Christensen and Lo [19] showed that the GSCM reduces to the Eshelby equation (2.20) in dilute conditions. The relative bulk modulus f_K is given by equation 2.18. Results for f_G are plotted in figures A.1 and A.2. The ratio of the phase moduli is kept constant ($G_1/G_0 = 10^3$) while the Poisson ratios ν_0 and ν_1 and the volume fraction ϕ are varied. When both phases are incompressible, i.e. $\nu_0 = \nu_1 = 0.5$, the $\log(f_G)$–ϕ curve exhibits an inflection point at $\phi \approx 0.70$ and another one at $\phi \approx 0.95$, after which f_G increases very fast to its final value G_1/G_0. It is self-evident that the resulting shoulder in the relative modulus curve between these points is obscured when the particles are rigid, like in the suspensions considered by Christensen [20]. On the other hand, Christensen and Lo [19] looked at suspensions with finite ratios of moduli and their calculated $f_G(\phi)$ curves all had a monotonously increasing slope. The results presented here reveal that this is due to the low Poisson ratios of the materials they used in their simulations ($\nu_0 = 0.35$, $\nu_1 = 0.20$ and $\nu_1 = 0.22$). Figure A.1 shows that, upon lowering the Poisson ratio of the

Table A.1: Parameters used in the GSCM [19, 20] for suspensions of spheres.

Shear modulus G (equation 2.26)			
$\left.\begin{matrix} A \\ B \\ C \end{matrix}\right\}$	$= c_1\left(\frac{G_1}{G_0}-1\right)\eta_1\phi^{10/3} + c_2\left[63\left(\frac{G_1}{G_0}-1\right)\eta_2 + 2\eta_1\eta_3\right]\phi^{7/3}$		
	$+ c_3\left(\frac{G_1}{G_0}-1\right)\eta_2\phi^{5/3} + c_4\left(\frac{G_1}{G_0}-1\right)\eta_2\phi + c_5\eta_2\eta_3$		
with...	... for A:	... for B:	... for C:
c_1	$8(4-5\nu_0)$	$-4(1-5\nu_0)$	$-4(7-5\nu_0)$
c_2	-2	4	-2
c_3	252	-504	252
c_4	$-50(7-12\nu_0+8\nu_0^2)$	$150(3-\nu_0)\nu_0$	$-25(7-\nu_0^2)$
c_5	$4(7-10\nu_0)$	$-3(7-15\nu_0)$	$-(7+5\nu_0)$
η_1	$\left(\frac{G_1}{G_0}-1\right)(7-10\nu_0)(7+5\nu_1) + 105(\nu_1-\nu_0)$		
η_2	$\left(\frac{G_1}{G_0}-1\right)(7+5\nu_1) + 35(1-\nu_1)$		
η_3	$\left(\frac{G_1}{G_0}-1\right)(8-10\nu_0) + 15(1-\nu_0)$		

matrix, $f_G(\phi)$ decreases and the shoulder vanishes fast: at $\nu_0 = 0.49$ it is hardly recognizable anymore. In contrast, decreasing ν_1 while $\nu_0 = 0.5$ has a much weaker influence on f_G, as seen in figure A.2, and the shoulder remains.

A.2 Aligned fibers

Under the assumption of transverse isotropy, the elastic constitutive equation for a suspension of aligned fibers can be written in matrix form according to

$$\begin{bmatrix} \tau_{11} \\ \tau_{22} \\ \tau_{33} \\ \tau_{12} \\ \tau_{13} \\ \tau_{23} \end{bmatrix} = \begin{bmatrix} C_{11} & C_{12} & C_{13} & 0 & 0 & 0 \\ C_{12} & C_{22} & C_{23} & 0 & 0 & 0 \\ C_{13} & C_{23} & C_{22} & 0 & 0 & 0 \\ 0 & 0 & 0 & C_{44} & 0 & 0 \\ 0 & 0 & 0 & 0 & C_{44} & 0 \\ 0 & 0 & 0 & 0 & 0 & C_{22}-C_{23} \end{bmatrix} \begin{bmatrix} \epsilon_{11} \\ \epsilon_{22} \\ \epsilon_{33} \\ 2\epsilon_{12} \\ 2\epsilon_{13} \\ 2\epsilon_{23} \end{bmatrix} \tag{A.1}$$

with the index 1 corresponding to the direction of the fiber axes and the indices 2 and 3 corresponding to perpendicular directions in the transverse

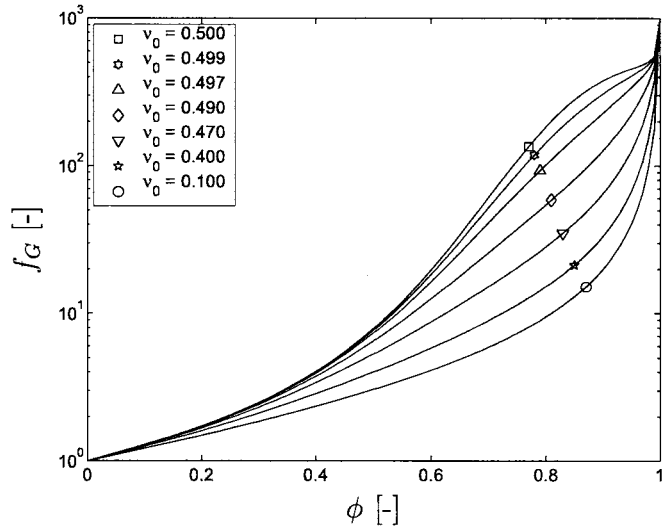

Figure A.1: Influence of the Poisson ratio of the matrix phase on the relative modulus of an elastic suspension of spheres ($G_1/G_0 = 10^3$, $\nu_1 = 0.5$).

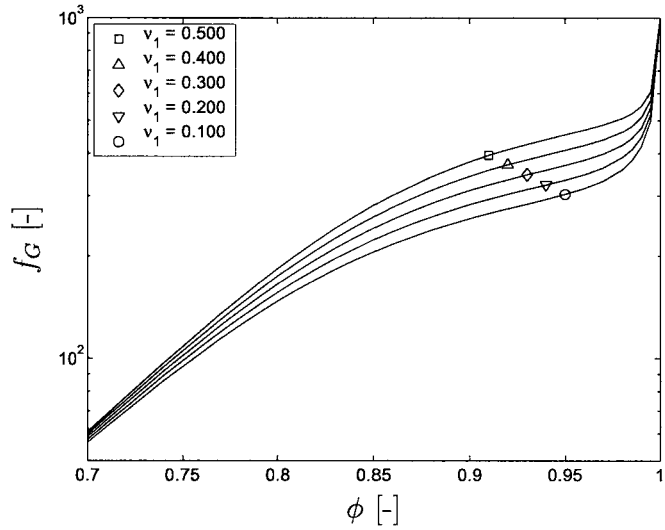

Figure A.2: Influence of the Poisson ratio of the particle phase on the relative modulus of an elastic suspension of spheres ($G_1/G_0 = 10^3$, $\nu_0 = 0.5$).

plane. In a more concise notation,

$$\underset{\sim}{\tau} = \underline{C} \cdot \underset{\sim}{\varepsilon} . \tag{A.2}$$

Hashin and Rosen [39] conveniently selected the following moduli to describe the mechanical behavior of the suspension:

$$K_{23} = \frac{C_{22}+C_{23}}{2} \quad \text{(plane – strain bulk modulus)}, \tag{A.3}$$

$$G_{23} = \frac{C_{22}-C_{23}}{2} \quad \text{(transverse shear modulus)}, \tag{A.4}$$

$$G_{12} = G_{13} = C_{44} \quad \text{(longitudinal shear modulus)}, \tag{A.5}$$

$$E_{11} = C_{11} - \frac{2C_{12}^2}{C_{22}+C_{23}} \quad \text{(longitudinal Young's modulus)}, \tag{A.6}$$

and C_{11}. In the case of a random arrangement of the fibers across the 23-plane they found

$$\frac{K_{23}}{K_0} = \frac{(1+2\nu_0\phi)\frac{K_1}{K_0} + 2\nu_0(1-\phi)}{(1-\phi)\frac{K_1}{K_0} + 2\nu_0 + \phi}, \tag{A.7}$$

$$\frac{G_{12}}{G_0} = \frac{(1+\phi)\frac{G_1}{G_0} + 1 - \phi}{(1-\phi)\frac{G_1}{G_0} + 1 + \phi}, \tag{A.8}$$

$$\frac{E_{11}}{E_0} = \left[\left(\frac{E_1}{E_0} - 1\right)\phi + 1\right]\left[\frac{D_1 - D_3F_1 + (D_2 - D_4F_2)\frac{E_1}{E_0}}{D_1 - D_3 + (D_2 - D_4)\frac{E_1}{E_0}}\right], \tag{A.9}$$

and

$$C_{11} = E_{11} + 4\nu_{12}^2 K_{23}, \tag{A.10}$$

where

$$\nu_{12} = \nu_{13} = \frac{L_1\phi\frac{E_1}{E_0} + L_2\nu_0(1-\phi)}{L_3\phi\frac{E_1}{E_0} + L_2(1-\phi)} \tag{A.11}$$

is the Poisson ratio for uniaxial stress in the direction of the fiber axes. The parameters D_1, D_2, D_3, D_4, F_1, F_2, L_1, L_2, and L_3 depend on the properties of the individual phases and on ϕ and are given in table A.2.

The relative transverse shear modulus G_{23}/G_0 is obtained from equation 2.26 with the parameters A, B, and C from table A.2. The dependence of G_{23}/G_0 on ν_0 and ν_1 is the same as in the case of a suspension of spheres. For a dilute suspension of aligned rigid fibers in an incompressible matrix, i.e. with

$$\frac{G_1}{G_0} \to \infty, \tag{A.12}$$

$$\nu_0 = \nu_1 = 0.5, \tag{A.13}$$

Table A.2: Parameters used in the composite cylinders model [39] and the GSCM [19,20] for suspensions of aligned fibers.

Longitudinal Young's modulus E_{11} (equation A.9)			
D_1	$1-\nu_1$	D_4	$2\nu_0^2\frac{\phi}{1-\phi}$
D_2	$\frac{1+\phi}{1-\phi}+\nu_0$	F_1	$\frac{\nu_0\phi\frac{E_1}{E_0}+\nu_1(1-\phi)}{\nu_1\phi\frac{E_1}{E_0}+1-\phi}$
D_3	$2\nu_1^2$	F_2	$\frac{\nu_1}{\nu_0}F_1$

Poisson ratio ν_{12} (equation A.11)	
L_1	$2\nu_1\left(1-\nu_0^2\right)\phi+\nu_0\left(1+\nu_0\right)\left(1-\phi\right)$
L_2	$\left(1-\nu_1-2\nu_1^2\right)\phi$
L_3	$2\left(1-\nu_0^2\right)\phi+\left(1+\nu_0\right)\left(1-\phi\right)$

Transverse shear modulus G_{23} (equation 2.26)	
A	$3c_1c_2\phi\left(1-\phi\right)^2+\left(c_2\eta_0-c_3\phi^3\right)\left(c_1\eta_0\phi-c_4\right)$
B	$-6c_1c_2\phi\left(1-\phi\right)^2+\left[c_2\left(\eta_0-1\right)-2c_3\phi^3\right]\left(c_1\phi+c_4\right)$
C	$3c_1c_2\phi\left(1-\phi\right)^2+\left(c_2+c_3\phi^3\right)\left(c_1\phi+c_4\right)$

c_1	c_2	c_3	c_4	η_0	η_1
$\frac{G_1}{G_0}-1$	$\frac{G_1}{G_0}+\eta_1$	$\frac{G_1}{G_0}\eta_0-\eta_1$	$\frac{G_1}{G_0}\eta_0+1$	$3-4\nu_0$	$3-4\nu_1$

and

$$\phi \to 0\,, \tag{A.14}$$

the relative transverse shear modulus according to the GSCM is found to be

$$\frac{G_{23}}{G_0} = 1+2\phi\,. \tag{A.15}$$

This is the two-dimensional equivalent of Einstein's model for dilute suspensions of rigid spheres, as given by Brady [13].

Appendix B

Modifying the rate equations for fast stabilized precursors

An alternative formulation of the (unbounded) homogeneous nucleation rate appearing in the differential model of crystalline structure formation,

$$\dot{N}_n(t) = \frac{N_p(t)}{\tau_{pn}(t)}, \tag{B.1}$$

is derived here for $\tau_{pn} \to 0$, which corresponds to the situation that all precursors, once created, are immediately transformed into nuclei. The superscript *hom* is omitted because only homogeneous precursors are considered. The evolution of the number of homogeneous precursors is given by

$$\dot{N}_p(t) = \tilde{I}_p(t) - \frac{N_p(t)}{\tau_p(t)}, \tag{B.2}$$

where $\tilde{I}_p$ is a shorthand notation for $I_{pq} + I_{pf} + \dot{T}\frac{\partial N_{pa}}{\partial T}$. Now suppose that, at some time $t = t'$, $\tau_{pn} \to 0$. It is easily derived from equation 2.76 that, in a fast nucleation process, the disappearance of precursors is dominated by nucleation,

$$\lim_{\tau_{pn}\to 0} \tau_p = \tau_{pn}, \tag{B.3}$$

so that dissolution can be neglected. Since τ_p becomes constant, equation B.2 reduces to an ordinary differential equation with the general solution

$$N_p(t \geq t') = \mathrm{e}^{-\frac{t-t'}{\tau_p}} \left[N_p(t') + \int_{t'}^{t} \tilde{I}_p(u) \mathrm{e}^{\frac{u-t'}{\tau_p}}\, du \right]. \tag{B.4}$$

The number of homogeneous nuclei is obtained by integrating equation B.1, after substitution of equation B.4,

$$N_n(t \geq t') = N_n(t') + \int_{t'}^{t} \left[\frac{N_p(t')}{\tau_p} \mathrm{e}^{-\frac{s-t'}{\tau_p}} + \int_{t'}^{s} \frac{\tilde{I}_p(u)}{\tau_p} \mathrm{e}^{-\frac{s-u}{\tau_p}}\, du \right] ds. \tag{B.5}$$

Taking $\tau_p \rightarrow 0$ in equation B.5 and making use of

$$\lim_{\theta \rightarrow 0} \frac{\mathrm{e}^{-\frac{t}{\theta}}}{\theta} = \delta(t) \,, \tag{B.6}$$

where $\delta(t)$ is the Dirac function, it follows that

$$\begin{aligned} N_n(t \geq t') &= N_n(t\prime) + \int_{t'}^{t} \left[N_p(t')\delta(s-t') + \int_{t'}^{s} \tilde{I}_p(u)\delta(s-u)du \right] ds \\ &= N_n(t') + N_p(t') + \int_{t'}^{t} \tilde{I}_p(s)\, ds \,. \end{aligned} \tag{B.7}$$

Thus, if $\tau_{pn} \rightarrow 0$, the nucleation rate is equal to the rate of creation of precursors,

$$\dot{N}_n(t \geq t') = I_{pq}(t) + I_{pf}(t) + \dot{T}(t) \frac{\partial N_{pa}(t)}{\partial T} \,. \tag{B.8}$$

If, in addition, $I_{pq} = I_{pf} = 0$, the nucleation process is purely athermal: no new nuclei appear unless the temperature is lowered.

The result obtained here allows for a description of crystallization processes involving fast nucleation, without using equation B.1. In the example used above, where the transition from slow to fast nucleation kinetics takes place at t', we get:

$$t < t' \quad \begin{cases} \dot{N}_p(t) &= \tilde{I}_p(t) - \frac{N_p(t)}{\tau_p(t)} \\ \dot{N}_n &= \frac{N_p(t)}{\tau_{pn}(t)} \end{cases}$$

$$t \geq t' \quad \begin{cases} N_n(t') &\rightarrow N_n(t') + N_p(t') \\ N_p(t') &\rightarrow 0 \\ \dot{N}_n(t) &= \tilde{I}_p(t) \end{cases}$$

The implementation of the inverse transition, from fast to slow nucleation kinetics, is trivial.

Appendix C

Tracing the length distribution of precursors

The evolution equation for the number of homogeneous precursors is given by

$$\dot{N}_p(t) = \tilde{I}_p(t) - \frac{N_p(t)}{\tau_p(t)} \tag{C.1}$$

with the abbreviation $\tilde{I}_p = I_{pq} + I_{pf} + \dot{T}\frac{\partial N_p^{hom}}{\partial T}$ as introduced in appendix B. The length of a single precursor follows from

$$\dot{L}_p(t) = I_l(t) - \frac{L_p(t)}{\tau_l(t)}, \tag{C.2}$$

where I_l is the driving force behind longitudinal growth and τ_l is a relaxation time associated with the length of a precursor. As before, only homogeneous precursors are considered here. Therefore, the superscript *hom* is omitted again.

The length of an oriented crystallite may be described by a model similar to equation C.2, taking $\tau_l \to \infty$ because the kebabs growing from a shish, or the spherulites forming a row crystallite, prevent shortening of the threadlike precursor that forms the core of the crystallite. One could use the same I_l as for the precursors before nucleation, assuming that the ends of a precursor keep growing by the same process after it has been nucleated, or assume that longitudinal growth stops at the moment of nucleation because the chains protruding from the tips of the shish are incorporated in the lamellae. Alternatively, a finite rate at which nucleated precursors stop growing could be introduced. Here, however, we only look at the growth process of precursors before they are nucleated.

Keeping track of the length distribution of precursors is complicated by the fact that growth and disappearance of precursors take place at the same

time. Here, the simplifying assumption is made that the growth process is uniform, i.e. independent of L_p, which means that the relaxation time τ_l is infinite. Hence

$$\dot{L}_p(t) = I_l(t) \; . \tag{C.3}$$

Increasing the length of a precursor will most likely decrease the probability that it dissolves, so a single parameter τ_{pd} will not adequately describe the overall process of dissolution. Therefore, the length distribution is represented by a discrete number of classes. Each class contains $N_{p,k}$ precursors, to all of which are assigned a length $L_{p,k}$ and a dissolution time $\tau_{pd,k}$. A constant range of lengths W is taken for all classes here, but generalization of the method to unequally sized classes is straightforward.

A consequence of the assumption that the length relaxation time is infinite is that, during an infinitesimal time interval Δt, the entire length distribution is shifted by the amount $\Delta L_p = \dot{L}_p \Delta t$. Obviously $\dot{L}_p \geq 0$ because, otherwise, the length of the shortest precursors would become negative. If the time step Δt is chosen such that

$$\Delta t < \frac{W}{\dot{L}_p(t)} \, , \tag{C.4}$$

precursors from a class $N_{p,k}$ can only move to the adjacent class $N_{p,k+1}$. The change of the length distribution is given by a set of balance equations

$$\dot{N}_{p,k}(t) = \frac{\dot{L}_p(t)}{W} \left[N_{p,k-1}(t) - N_{p,k}(t) \right] - \frac{N_{p,k}(t)}{\tau_{p,k}(t)} \tag{C.5}$$

for $k = 1, 2, 3, \ldots$ with

$$N_{p,0}(t) = \frac{\dot{N}_p(t) \, W}{\dot{L}_p(t)} \, . \tag{C.6}$$

When the relaxation time τ_l of the precursors is finite, the precursors will not grow uniformly. However, with certain modifications, the length distribution can still be modeled by a method like the one described here.